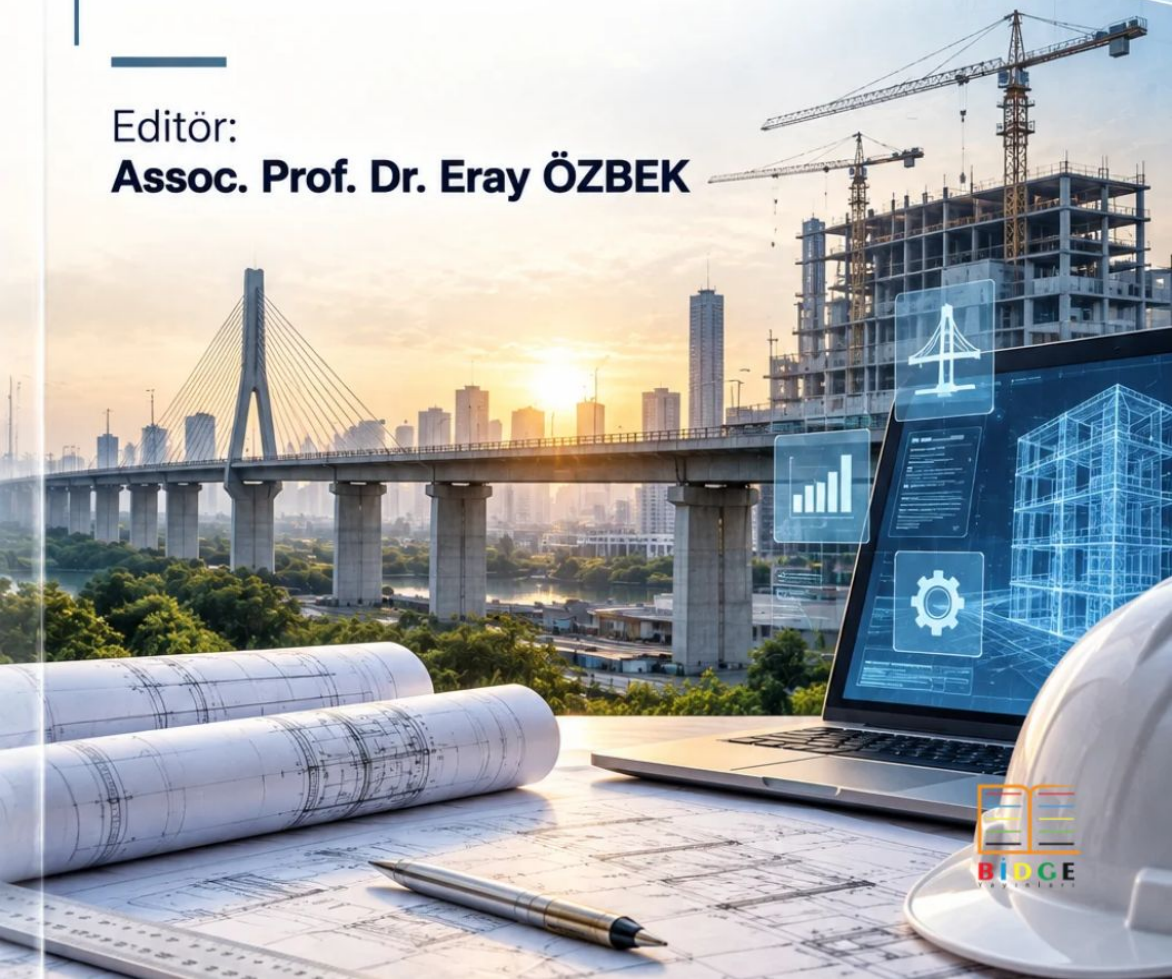
ACADEMIC RESEARCH AND TECHNOLOGY ON CIVIL ENGINEERING

Editör:
Assoc. Prof. Dr. Eray ÖZBEK



BİDGE

BİDGE Yayınları

Academic Research and Technology on Civil Engineering

Editör: Assoc. Prof. Dr. Eray ÖZBEK

ISBN: 978-625-5057-49-5

1. Baskı
Sayfa Düzeni: Gözde YÜCEL
Yayınlama Tarihi: 2026-10-25
BİDGE Yayınları

Bu eserin bütün hakları saklıdır. Kaynak gösterilerek tanıtım için yapılacak kısa alıntılar dışında yayıncının ve editörün yazılı izni olmaksızın hiçbir yolla çoğaltılamaz.

Sertifika No: 71374
Yayın hakları © BİDGE Yayınları
www.bidgeyayinlari.com.tr - bidgeyayinlari@gmail.com
Krc Bilişim Ticaret ve Organizasyon Ltd. Şti.
Güzeltepe Mahallesi Abidin Daver Sokak Sefer Apartmanı No: 7/9 Çankaya / Ankara

PREFACE

Civil engineering is one of the most deep-rooted disciplines in human history. It is constantly evolving in line with advancements in science and the principles of sustainability. In today's world, the goal of civil engineering extends beyond merely constructing safe structures; it also aims to minimize the negative environmental impacts of these structures, optimize the use of resources, and lay the infrastructures for the smart cities of the future. At the heart of this transformation and innovation lies, undoubtedly, academic research. This book encompasses current studies and scientific findings across a broad spectrum ranging from structural, geotechnical, hydraulic, and transportation engineering to construction management and materials technology. I would like to express my gratitude to all the authors who contributed to this work by sharing their scientific expertise and research, as well as to my esteemed colleagues who provided valuable input during the peer-review process.

Assoc. Prof. Dr. Eray ÖZBEK

GAZI UNIVERSITY

İÇİNDEKİLER

EARLY-AGE HYDRATION EVOLUTION OF CEMENT PASTES WITH HIGH FLY ASH REPLACEMENT: NUMERICAL INSIGHTS 1
HAYDAR DEHGAN

EFFECT OF PILE SPACING ON THE BEHAVIOR OF QUAY PILES UNDER LINEAR WAVE LOADING 30
MUHAMMET ENSAR YİĞİT, ÜMİT GÖKKUŞ

FLEXURAL BEHAVIOR OF RAPIDLY COOLED CJP GROOVE WELDS ON ULTRA HIGH STRENGTH STEEL .. 52
EMİR ALTIPARMAK, ERAY ÖZBEK

GOOGLE EARTH ENGINE FOR WATER RESOURCES MONITORING: DATASETS, APPLICATIONS AND LIMITATIONS 68
YILDIRIM BAYAZIT

DEEP LEARNING FOR STREAMFLOW PREDICTION: LONG SHORT-TERM MEMORY NETWORKS AND THE CHANGING PRACTICE OF HYDROLOGICAL MODELLING 85
YILDIRIM BAYAZIT

OCCUPATIONAL SAFETY IN 3D CONCRETE PRINTING: HAZARD TRANSFORMATION AND A TASK-BASED RISK MANAGEMENT FRAMEWORK 100
ÖZGE ALBOĞA

Seismic Performance of Retaining Walls: Numerical, Experimental, and Field Evidence 123
TEOMAN EFEOĞLU

SEISMIC EARTH PRESSURES ON RETAINING WALLS: ANALYTICAL AND THEORETICAL APPROACHES 146

İÇİNDEKİLER

TEOMAN EFEOĞLU

SUSTAINABLE SOIL IMPROVEMENT TECHNICS FOR CIRCULAR ECONOMY AND RESILIENCE IN ROAD INFRASTRUCTURES 177

HALİL OĞUZHAN KARA

BÖLÜM 1

EARLY-AGE HYDRATION EVOLUTION OF CEMENT PASTES WITH HIGH FLY ASH REPLACEMENT: NUMERICAL INSIGHTS

HAYDAR DEHGAN[1]

Introduction

The cementitious systems that underpin modern infrastructure are undergoing a paradigmatic shift toward sustainable design, driven by an imperative to reduce embodied carbon while maintaining or enhancing performance. A central strategy is the partial or substantial replacement of Portland cement with supplementary cementitious materials (SCMs), among which fly ash (FA) has long been the most widely employed. In particular, high-volume fly ash (HVFA) systems—where FA replacement fractions exceed conventional limits—have attracted intense research attention due to their potential to lower greenhouse gas emissions, refine microstructure, and improve certain durability aspects. However, the early-age behavior of HVFA pastes remains a persistent challenge, as the pozzolanic activity of FA is typically lower than that of cement, often resulting in retarded hydration kinetics, delayed gel formation, and weaker early-age strength. These early-age limitations can constrain the applicability of HVFA in precast components, rapid-build projects, and other applications where early stiffness and strength are critical (Bu et al., 2025). Consequently, a precise understanding of the hydration evolution at the micro- to meso-scale in HVFA pastes is essential for

[1] Assist. Prof Dr., Sakarya University, Faculty of Engineering, Department of Civil Engineering, Orcid: 0000-0001-7801-2288

reliable predictions of early-age performance and for guiding mix-design strategies that reconcile sustainability with structural adequacy.

A mechanistic lens on early hydration emphasizes the interplay among chemical reactions, microstructure development, and transport properties. Classic hydration theory partitions cement hydration into distinct kinetic processes, most notably nucleation and growth (NG), phase-boundary reactions (I), and diffusion (D). The Krstulovic-Dabic hydration kinetic framework has proven a valuable tool for interpreting calorimetric data and linking hydration kinetics to mechanical development across ages (Quan et al., 2023). In FA-containing systems, the presence of unreacted aluminosilicate glass, dilution of reactive clinker phases, and the slower dissolution of FA particles collectively modulate the NG, I, and D processes, thereby shaping early strength and stiffness trajectories.

Beyond chemical kinetics, HVFA pastes exhibit distinctive microstructural evolutions that bear directly on early-age properties. The pozzolanic reaction of FA consumes calcium hydroxide (CH) and contributes to secondary C–S–H gel formation, refining pore structure and reducing capillary porosity over time. Yet at early ages, insufficient CH consumption and limited nucleation sites can lead to looser microstructures and reduced early strength. Recent work indicates that nanostructured additives, GO or nano-SiO2, and combined nano-modifications can modulate hydration product development and pore refinement, thereby enhancing early-age performance while preserving long-term gains (Huang et al., 2026). In HVFA systems, sandwiched between clinker dilution and accelerated later-age reactions, the balance of early microstructure refinement and delayed pozzolanic activity becomes a critical design target.

Numerical insights into HVFA hydration have advanced through coupling calorimetry, microstructural modelling, and constitutive frameworks. Studies leveraging the Krstulovic-Dabic model and related hydration kinetics analyses provide a mechanistic basis for interpreting heat release data and translating it into predictions of early-age strength gain and modulus development. In parallel, multiscale modelling approaches—spanning nucleation and growth of C–S–H at the nanoscale to macro-scale elastic response—offer a

coherent pathway to connect microscopic hydration events with bulk mechanical performance. Recent investigations highlight the benefits of incorporating supplementary activators, ultrafine FA variants, and advanced nano-reinforcement strategies to drive earlier gel evolution and densification in HVFA systems; these interventions yield measurable improvements in early stiffness and strength without sacrificing long-term benefits (Quan et al., 2023).

In this context, the present study comprehensively investigates the early-age hydration evolution of cement pastes incorporating high fly ash (FA) replacement levels through numerical simulations utilizing the Virtual Cement and Concrete Testing Laboratory (VCCTL) software developed by the National Institute of Standards and Technology (NIST). The central objective is to establish predictive capabilities for early-age hydration heat release, gel formation, microstructural densification, and the concomitant development of elastic properties as FA content increases beyond conventional thresholds. To this end, the work builds on established hydration kinetics frameworks and multiscale representations of the C–S–H/gels system, while explicitly accounting for FA's dilution effect, delayed pozzolanic activity, and potential microstructural refinements induced by elevated FA contents.

Numerical Method and Simulation Procedure

In this study, a numerical modeling approach was adopted to investigate the effects of high-volume fly ash (FASH) replacement on the early-age hydration and microstructural evolution of cement-based systems. Accordingly, the Virtual Cement and Concrete Testing Laboratory (VCCTL) software, developed by the National Institute of Standards and Technology (NIST) (Bullard, 2014), was employed.

VCCTL is an advanced software platform that models the three-dimensional (3D) microstructure of cement paste using a pixel-based, micron-scale cellular automaton approach and simulates phase transformations. Within the model, the CEM I-type cement matrix was volumetrically replaced with FASH in 10% increments, ranging from 0% to 90%, resulting in a total of 10 distinct mixture designs being defined in the system.

The simulations were conducted over a 72-hour hydration timeline to evaluate the reaction kinetics of the cement pastes. Using the software, time-dependent phase depletion (C_3S, C_2S, C_3A, C_4AF, and hemihydrate), precipitation rates of hydration products (CH, C-S-H, and ettringite), adiabatic temperature rise, chemical shrinkage (ChemShrink) values, and changes in microstructural porosity were numerically calculated.

All volumetric phase data and elastomechanical matrix parameters (Young's modulus, Poisson's ratio, and compressive strength) obtained from the simulations were directly extracted from the software's output algorithms and used to establish analytical correlations.

Results and Discussion

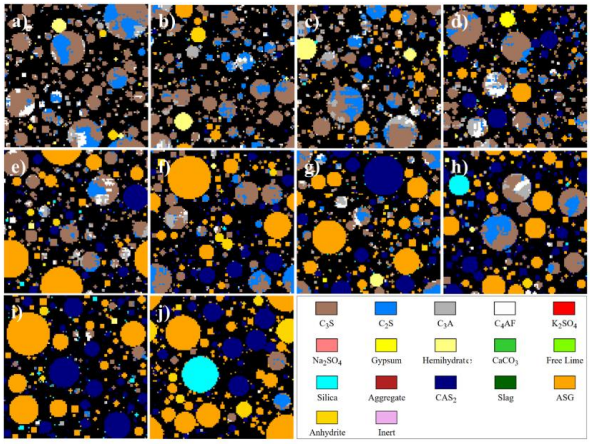
Microstructural Appearance

The simulated microstructural evolution of the cement pastes, spanning from the reference mixture (0% FA) to the highest replacement level (90% FA) at 72 hours, is illustrated in Figur 1. The graphical representations clearly capture the systematic transformation of the matrix configuration and solid phase continuity induced by the volumetric substitution of cement with fly ash.In the reference paste (Figure a), the microstructure is characterized by a dense, interconnected matrix predominantly populated by unhydrated tricalcium silicate (C_3S, brown) and dicalcium silicate (C_2S, light blue) particles, interspersed with fine distributions of aluminate (C_3A, grey) and ferrite (C_4AF, white) phases. The capillary porosity (represented by the black background) is relatively minimized due to the early formation of hydration products filling the interstitial spaces.As the fly ash replacement level increases progressively from 10% to 90% (Figure 1-b to Figure 1-j), a significant microstructural dilution effect is observed. The volume fraction of the primary clinker minerals (C_3S, C_2S, C_3A, and C_4AF) systematically depletes, marked by the rapid disappearance of the brown and light blue particulate domains. Concurrently, the microstructure becomes dominated by unreacted spherical fly ash particles predominantly represented by quartz/silica inclusions (cyan) and inert/aluminosilicate glassy spheres (orange/dark blue configurations).At extreme replacement thresholds, particularly

from 50% to 90% FA (Figures f to j), the spatial continuity of the cementitious matrix undergoes severe disruption. The larger orange and dark blue spherical inclusions act as non-reactive fillers at this early age (72 hours), failing to establish a cohesive, cross-linked microstructural network. This phenomenon is visually correlated with the expanding black background areas, indicating a substantial increase in interconnected capillary porosity and a lack of sufficient space-filling hydration jels (C-S-H and CH). The microstructural evidence visually confirms the linear mechanical degradation noted in the bulk properties: beyond a 20% replacement threshold, the framework transitions from a continuous binder matrix into a loosely bound particulate suspension of fly ash spheres, which fundamentally accounts for the 70% drop in early-age Young's modulus and compressive strength.

The scenario described—a progressive dilution of the clinker matrix with fly ash up to 90% replacement and corresponding microstructural disruption by 72 hours—resonates with established findings in high-quality literature. In HVFA systems, early-age hydration is routinely retarded due to limited pozzolanic activity and clinker dilution, which reduces early gel formation (C-S-H and CH) and elevates capillary

Figure 1. Microstructural appearance of simulated FA-doped cement mortars.



Mechanical Properties

The correlation between the fly ash (FA) substitution ratio and the elastomechanical parameters (Young's modulus and Poisson's ratio)

of 72-hour-old mortar specimens is presented in Figure 2. The Young's modulus (E), plotted on the right vertical axis, exhibits a continuous, non-linear degradation behavior as fly ash content increases from 0% to 90%. In the control configuration (0% FA), the matrix records its maximum stiffness with a Young's modulus of approximately 18.27 GPa. As fly ash is incrementally introduced, the elastic stiffness experiences a clear reduction. Between 0% and 50% FA replacement, the stiffness decreases steadily, dropping to around 12.0 GPa. Beyond this intermediate threshold, the rate of mechanical degradation accelerates sharply, culminating in a critical low of 5.66 GPa at 90% FA substitution. This global trend follows a non-linear second-order polynomial regression layout, which is mathematically defined as follows:

$$y = 0.0015x^2 - 0.01x + 0.2893 \quad \text{(Eq. 1)}$$

The regression model provided in Eq. 1 features a high correlation coefficient, where R-squared equals 0.9624, mathematically validating the severe loss of solid-phase structural rigidity. Conversely, the Poisson's ratio, mapped on the left vertical axis, demonstrates an inverse relationship, rising steadily across the entire replacement spectrum. For low-volume blends (0% to 30% FA), the lateral deformation coefficient remains highly stable, fluctuating minimally within a tight range of 0.274 to 0.278. This stable plateau indicates that the internal structural network maintains its cohesion under load. However, as the fly ash content exceeds 30%, the Poisson's ratio transitions into a steep, highly predictable linear ascent. It climbs past 0.0285 at 50% FA, breaks through 0.302 at 70% FA, and ultimately stabilizes at a maximum value of 0.340 at 90% FA replacement. This linear progression is modeled by a robust linear regression equation:

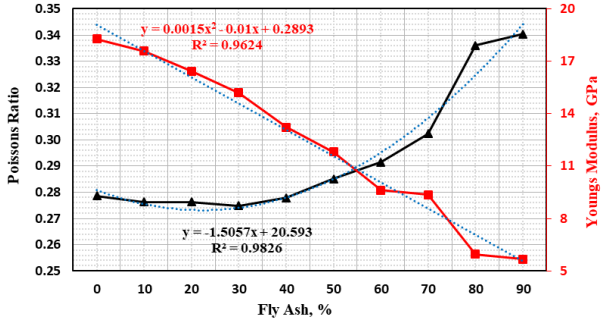
$$y = -1.5057x + 20.593 \quad \text{(Eq. 2)}$$

The linear model expressed in Eq. 2 features an excellent statistical fit, where R-squared equals 0.9826.The simultaneous reduction in axial stiffness governed by Eq. 1 and the increase in lateral expansion capacity described by Eq. 2 directly reflect a major modification in the microstructural load-bearing performance of the mortar skeleton. The non-linear softening of the Young's modulus proves that replacing highly reactive clinker phases with slow-reacting

fly ash reduces the overall density of the main hydration products, resulting in a more flexible solid framework. At the same time, the transition of the Poisson's ratio from a stable early plateau to a steep linear rise indicates that the mechanical matrix becomes less rigid and more susceptible to lateral shear sliding and volumetric strain under uniaxial loading conditions. This mechanical imbalance confirms that exceeding a 20% to 30% fly ash replacement threshold alters the bulk deformation kinetics of the material.

The decline in elastic stiffness agrees closely with studies showing that higher FA contents generally reduce modulus in mortar and concrete (Maysyurah et al., 2025). In mortar specifically, fly ash incorporation has been shown to significantly decrease the average elastic modulus of hydration products at the microscale, which supports the present interpretation that the solid load-bearing skeleton becomes more compliant as clinker is replaced. The Poisson's ratio trend is only partly aligned with the literature. One recent mortar study found that Poisson's ratio remained within the normal solid range despite FA addition, rather than showing mechanical instability (Maysyurah et al., 2025). Comparable links between denser matrix development and lateral-deformation performance have also been reported in fly ash geopolymer systems (Yang et al., 2023).

Figure 2. Young's moduli and Poisson's ratios of 72-day-old mortars, depending on FA content.



The numerical correlation between the fly ash (FA) replacement level and the multi-physical parameters specifically porosity ratio and compressive strength of 72-hour-old simulated mortar specimens is analytically evaluated in Figure 3. The porosity ratio, mapped on the left vertical axis, demonstrates a continuous and highly predictable

upward trend across the entire replacement spectrum. In the control configuration (0% FA), the simulated matrix records its minimum void fraction with a porosity ratio of approximately 0.285. As fly ash is incrementally introduced, the volumetric pore space experiences a steady, uniform increase. This progression follows a strong linear trajectory up to 80% FA replacement, where the porosity reaches approximately 0.50, before slightly flattening toward 90% FA content. This global behavior is modeled by a highly correlated linear regression equation:

$$y = 0.0255x + 0.2611 \quad \text{(Eq. 3)}$$

The linear relationship expressed in Eq. 3 features an excellent statistical fit, where R-squared equals 0.9931, confirming a direct and systematic microstructural dilution and pore-expanding effect governed by the simulated fly ash additions. Conversely, the compressive strength, plotted on the right vertical axis in MPa, exhibits a profound non-linear degradation behavior that mirrors the porosity expansion. The reference mortar matrix (0% FA) achieves its maximum mechanical capacity with a compressive strength of approximately 29.76 MPa. Upon the introduction of fly ash, the load-bearing capacity undergoes a linear, steep decline. This systematic strength loss drops steadily through intermediate replacement levels, registering around 15.58 MPa at 40% FA and falling further to 7.81 MPa at 60% FA. After a minor localized stabilization plateau between 60% and 70% FA, the modeled mechanical strength drops to its absolute minimum of 2.86 GPa at 90% FA replacement. This global degradation pattern is represented by a robust linear regression model:

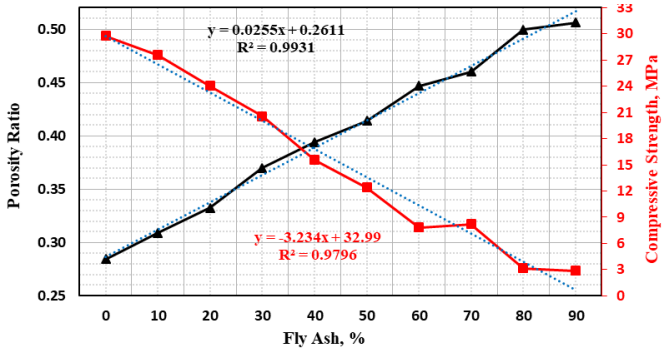
$$y = -3.234x + 32.99 \quad \text{(Eq. 4)}$$

The regression equation provided in Eq. 4 captures the mechanical softening with a high correlation coefficient, where R-squared equals 0.9796.The simultaneous expansion of internal porosity regulated by Eq. 3 and the linear degradation of bulk compressive strength described by Eq. 4 clearly reveal a fundamental transformation in the simulated internal structure of the mortar skeleton. The steady rise in porosity proves that replacing the dense, space-filling primary cement hydration products with slow-reacting fly ash particles significantly increases the volume of capillary voids within the modeled

matrix. Concurrently, the sharp reduction in compressive strength confirms that this porous, less cohesive skeletal framework drastically lowers the overall load-bearing resistance under simulated uniaxial compression. This clear inverse relationship demonstrates that high-volume fly ash replacement directly trades microstructural density for volumetric porosity, fundamentally dictating the bulk mechanical degradation of the modeled composite material.

The study argues that rising fly ash replacement increases porosity and depresses 72-hour compressive strength, and that inverse pattern is well aligned with the literature. Early-age studies consistently report that higher FA contents increase porosity or pore size while reducing early compressive strength, especially in high-volume systems. The simulated linear rise in porosity agrees with experimental evidence that FA significantly affects pore structure at early age and commonly raises total porosity in blended cement pastes and mortars (Yu & Ye, 2013).

Figure 3. Compressive strengths and porosity ratios of mortars at 72 days of age, depending on FA content.



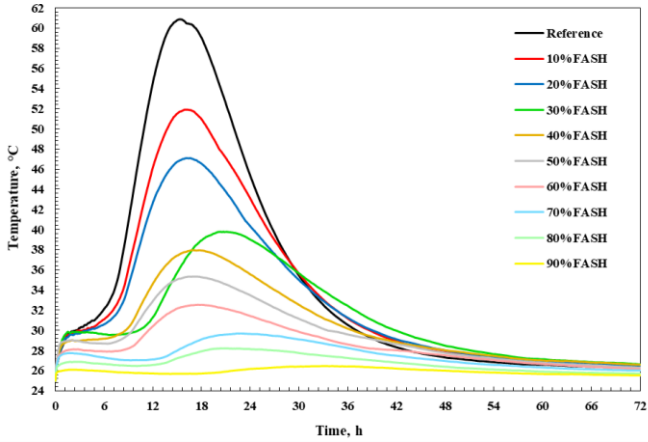
Hydration Kinetics and Thermal Evolution

When evaluating the 72-hour hydration temperature evolution of simulated mortar mixtures, progressively diluting Portland cement clinker with fly ash (FA) leads to a direct and systematic reduction in exothermic kinetics and peak temperatures. The control mixture (0% FA) exhibits classic multi-stage behavior, transitioning from an initial 2-hour dissolution phase into a rapid acceleration stage that reaches a sharp peak of 60.8 °C at approximately 15 hours, driven by primary clinker phase hydration (C3S and C3A). Incorporating 10%, 20%, and

30% FA systematically reduces maximum temperatures to 51.9 °C, 47.1 °C, and 39.8 °C, while delaying peak times to 17, 18, and 21 hours, respectively, as slow-reacting fly ash spheres retard the nucleation and growth of hydration products. Beyond a 40% substitution threshold, the acceleration peak diffuses into a low-intensity thermal dome, whereas extreme replacements (70% to 90% FA) entirely suppress exothermic peaks, leaving the 90% FA mixture nearly horizontal between 24.0 °C and 26.0 °C across the entire 72 hours. Ultimately, high-volume fly ash substitution minimizes the chemical heat generation capacity of the binder skeleton, severely weakening early-age hydration kinetics during the critical first 3 days.

The observed trend is consistent with calorimetry studies reporting that increasing fly ash content prolongs the induction period, delays the acceleration stage, and weakens the main exothermic peak (Kuryłowicz-Cudowska, 2022). In particular, it has been reported that this retarding effect becomes more pronounced with increasing replacement ratios in high-volume fly ash mixtures and significantly suppresses early-age hydration up to 48 hours (Narmluk & Nawa, 2011). Therefore, the near disappearance of the peak in the 70–90% FA range is plausible as an extreme consequence of clinker dilution and low early-age reactivity (De la Varga et al., 2018).

Figure 4. Variation of hydration temperature of FA-doped mortars over time.



The calculated chemical shrinkage profiles of the simulated mortar mixtures over 72 hours, as a function of fly ash (FA)

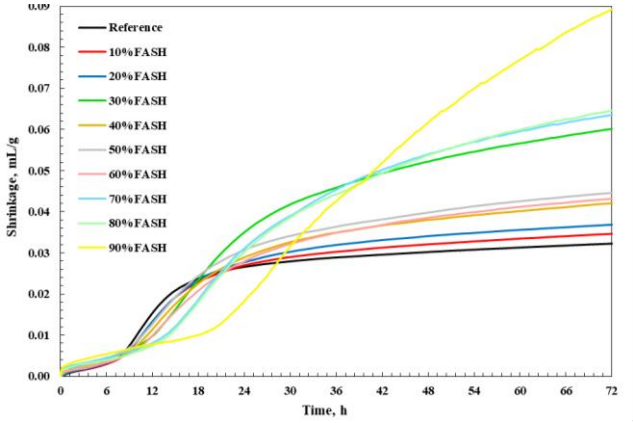
replacement levels, are presented in Figure 5. The transient curves reveal a time-dependent crossover behavior, with the final chemical shrinkage changing significantly as the FA content increases. During the first 12–18 hours, the shrinkage kinetics generally follow a dilution trend. The reference mixture (0% FA) and low-FA mixtures (10% and 20%) show a rapid increase in shrinkage between 6 and 15 hours, reaching higher values than high-volume FA mixtures such as 80% and 90% FA. This early behavior is mainly associated with the rapid hydration of highly reactive clinker phases, particularly C_3S and C_3A, which produce substantial chemical shrinkage. In contrast, high-FA mixtures remain relatively dormant during the initial hydration period.

A significant kinetic crossover occurs after approximately 18 hours. Between 24 and 72 hours, the chemical shrinkage of high-volume FA mixtures accelerates sharply and progressively exceeds that of the reference and low-FA mixtures. At 72 hours, the reference mixture exhibits the lowest final shrinkage of approximately 0.032 mL/g. With increasing FA replacement from 10% to 30%, the final shrinkage rises to approximately 0.035, 0.037, and 0.060 mL/g, respectively. This increase becomes more pronounced at higher FA levels, reaching approximately 0.064 mL/g for 80% FA and a maximum of 0.089 mL/g for 90% FA. The nearly linear increase observed in the 90% FA mixture after 24 hours indicates that, although high FA contents initially dilute clinker hydration, subsequent water interactions, absorption by porous ash particles, and possible early reactions substantially increase chemical shrinkage. Overall, the results demonstrate that high FA replacement levels can significantly increase 72-hour chemical shrinkage and thereby affect the volume stability of the modeled cementitious paste.

The central finding of the results is that high-volume fly ash replacement suppresses chemical shrinkage during the first few hours but may accelerate it during the 24–72-hour period. This early-age retardation is consistent with the literature, as the low early-age reactivity of fly ash, longer setting time, and lower degree of hydration generally result in lower chemical shrinkage during the first week. This interpretation is also supported by the general framework that chemical shrinkage is proportional to the degree of hydration and that the early-

age hydration of C3S and C3A generates substantial heat and volumetric contraction (Kapeluszna & Kotwica, 2024).

Figure 5. Time-dependent shrinkage values of FA-doped mortars.



Porosity Evolution and Clinker Phase Consumption Kinetics

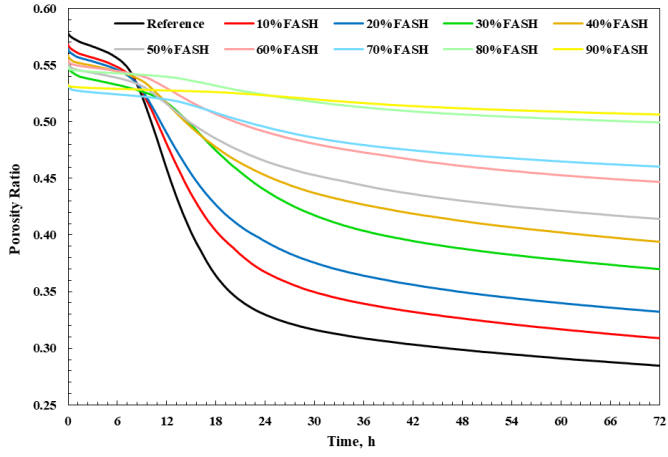
The numerical evolution of the porosity ratio of the simulated mortar mixtures over 72 hours, as a function of fly ash (FA) replacement levels, is presented in Figure 6. The time-dependent porosity profiles show a strong relationship with the hydration temperature profiles in Figure 4 and the predicted microstructural phase distributions. For the reference mixture (0% FA), the porosity ratio decreases sharply after approximately 6 hours, falling from an initial value of 0.578 to a minimum of about 0.285 at 72 hours. This rapid pore-filling behavior corresponds to the intense hydration and exothermic peak observed around 15 hours. The formation of hydration products from C_3S and C_2S progressively fills the capillary pores, producing a denser and more interconnected matrix.

Increasing the FA replacement from 10% to 90% progressively reduces the rate of porosity development and results in higher residual porosity at 72 hours. The final porosity ratios for 10%, 20%, and 30% FA mixtures are approximately 0.310, 0.332, and 0.370, respectively. This increase in residual pore volume is consistent with the reductions in Young's modulus and compressive strength shown in Figure 3. At high replacement levels, particularly 70–90% FA, porosity reduction is largely suppressed. The 80% and 90% FA mixtures remain at high-

porosity plateaus, reaching approximately 0.501 and 0.507 at 72 hours, respectively. This limited pore refinement corresponds to the low and nearly inactive hydration temperatures in Figure 4, indicating insufficient heat generation and hydration-product formation. Consequently, the unreacted fly ash particles remain loosely distributed, leaving an interconnected and highly porous capillary structure at 72 hours.

This interpretation of porosity is largely consistent with the literature in terms of early-age behavior over 72 hours. Previous studies have shown that increasing fly ash replacement levels significantly affect the pore structure at early ages, with the total porosity generally remaining higher and being closely associated with hydration kinetics. The rapid decrease in porosity observed in the reference mixture is consistent with the pore-filling effect associated with clinker hydration; in contrast, the limited reaction of fly ash during the first two days in high-volume fly ash systems reduces the rate of porosity refinement (Deschner et al., 2012). The increase in the most probable pore diameter with increasing fly ash content, together with the fact that total porosity decreases with age but remains at a higher level, supports the interpretation of the "flattening of the curves" described in the results (Zhao et al., 2018).

Figure 6. Change in the porosity ratio of FA-doped mortars over time.



The results for the unhydrated tricalcium silicate (C_3S) volume fraction over 72 hours, as a function of fly ash (FA) replacement levels,

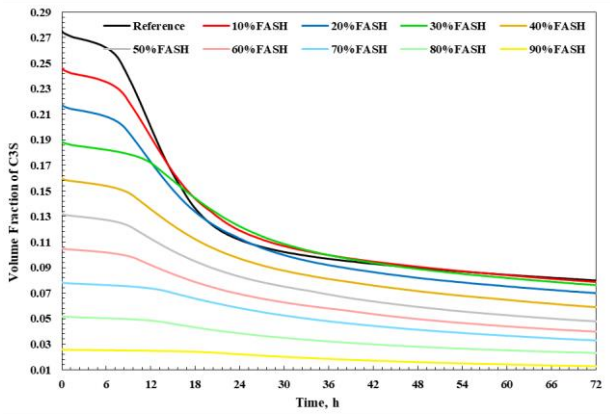
are presented in Figure 7. The depletion curves show a clear relationship with the hydration temperature profiles (Figure 4) and porosity evolution (Figure 6). For the reference mixture (0% FA), the initial C_3S volume fraction is approximately 0.275. After a short induction period during the first 6 hours, C_3S undergoes rapid depletion between 6 and 24 hours, reaching approximately 0.081 at 72 hours. This intense consumption corresponds to the major hydration peak at 15 hours and the sharp porosity reduction observed in Figure 6, confirming that C_3S dissolution promotes the formation of space-filling C-S-H gels and the development of a dense microstructural framework.

As FA replacement increases from 10% to 90%, the initial C_3S volume fraction progressively decreases due to clinker dilution. At low FA levels (10–30%), the C_3S curves still show a pronounced decline between 12 and 24 hours, indicating active early-age hydration of the remaining clinker. In contrast, at high replacement levels, particularly 70–90% FA, C_3S consumption is largely suppressed. For the 90% FA mixture, the initial C_3S fraction is only about 0.026 and remains nearly unchanged throughout 72 hours. This limited dissolution explains the inactive hydration temperature profiles in Figure 4 and the high porosity plateaus in Figure 6. The insufficient formation of hydration gels prevents the development of an interconnected microstructural framework, leaving unreacted FA particles in a loose, highly porous structure and contributing to the pronounced reduction in Young's modulus and compressive strength.

The retardation of early-age hydration in high-volume fly ash systems has been well documented; fly ash delays cement hydration during the initial period, and this effect becomes more pronounced as the replacement level increases (Narmluk & Nawa, 2011). In particular, the extension of the induction period from approximately 1.5 to 15 hours in a pure C3S system containing 50% fly ash, together with the substantially lower degree of hydration at 24 hours compared with pure C3S, directly corresponds to the weaker C3S depletion observed in the results during the 12–24-hour period. The underlying mechanism is not limited to clinker dilution; Ca^{2+} adsorption, a lower calcium concentration in the pore solution, and hindered C-S-H nucleation also

contribute to the suppression of early-age C3S hydration (De la Varga et al., 2018; Narmluk & Nawa, 2011).

Figure 7. Time-dependent variation of C3S in mortars with varying proportions of FA admixture.



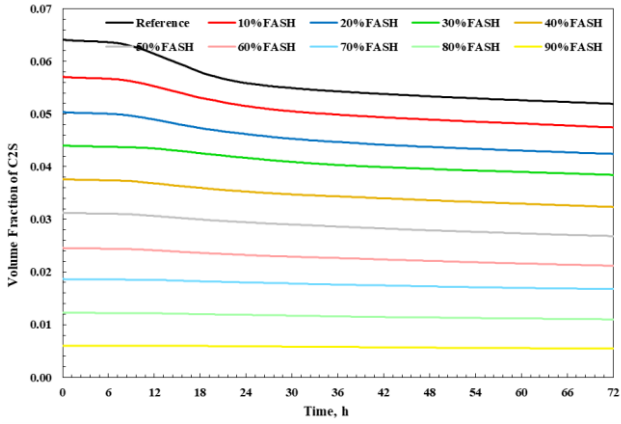
The numerical evolution of the unhydrated dicalcium silicate (C_2S) volume fraction over 72 hours, as a function of fly ash (FA) replacement, is presented in Figure 8. The depletion curves differ markedly from the rapid C_3S consumption shown in Figure 7 and are closely related to the porosity and mechanical stiffness trends in Figures 6 and 3. For the reference mixture (0% FA), the initial C_2S volume fraction is approximately 0.064. After a prolonged induction period of about 12 hours, C_2S is gradually consumed, decreasing to approximately 0.052 at 72 hours. This slow depletion reflects the inherently sluggish early-age hydration of the belite (C_2S) phase. Compared with the rapid C_3S hydration responsible for the main exothermic peak at 15 hours, C_2S contributes only modestly to early C-S-H formation, leaving a significant fraction unreacted within the microstructure.

As FA replacement increases from 10% to 90%, the initial C_2S volume fraction decreases due to clinker dilution. In all FA mixtures, the consumption curves remain relatively flat throughout the 72-hour period. At high replacement levels, the 80% and 90% FA mixtures remain nearly horizontal at approximately 0.012 and 0.006, respectively, indicating very limited or negligible C_2S dissolution. Thus, high FA dilution suppresses the early-age reaction of C_2S and limits the formation of additional space-filling hydration products. This

behavior contributes to the persistence of capillary pores and helps explain the substantial reduction in compressive strength and Young's modulus observed at high FA replacement levels.

The markedly lower early-age reactivity of C2S compared with C3S is strongly consistent with the existing literature; atomistic and molecular studies have demonstrated that the initial hydration of C3S proceeds more rapidly than that of C2S, whereas Ca dissolution in C2S remains relatively sparse and less pronounced. The explanation that the decrease in the initial C2S content with increasing fly ash replacement is primarily associated with clinker dilution is also consistent with the literature; in high-volume fly ash mixtures, the loss of early-age strength is mainly attributed to the dilution effect and the slow pozzolanic reaction (Zou et al., 2020).

Figure 8. Time-dependent variation of C2S in mortars with varying proportions of FA admixture.

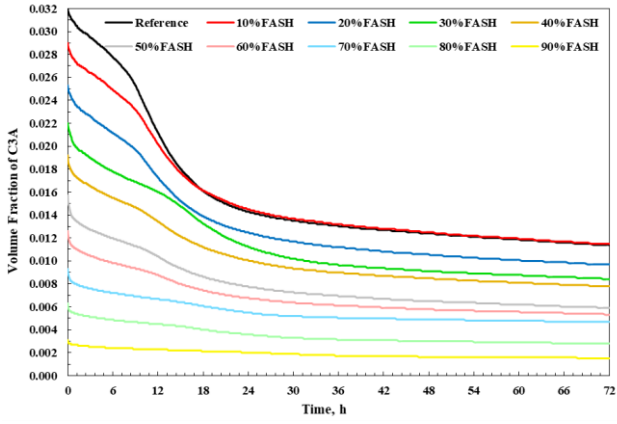


The simulated evolution of the unhydrated tricalcium aluminate (C_3A) volume fraction over 72 hours, as a function of fly ash (FASH) replacement, is presented in Figure 9. For the reference mixture (0% FASH), the initial C_3A volume fraction is approximately 0.032. During the first 18 hours, C_3A undergoes rapid consumption, decreasing to about 0.016. This high reactivity contributes to the early heat release peak at 15 hours (Figure 4). After 18 hours, the depletion rate slows considerably and reaches approximately 0.011 at 72 hours, suggesting that the formation of early hydration products progressively limits further C_3A dissolution. With increasing FASH replacement from 10%

to 90%, the initial C_3A volume fraction decreases due to clinker dilution. At low-to-intermediate replacement levels (10–40% FASH), C_3A continues to show substantial consumption during the first 18 hours, indicating active early-age hydration. In contrast, at high replacement levels, particularly 70–90% FASH, the reaction kinetics become nearly inactive. The 90% FASH mixture starts with only about 0.003 C_3A and remains almost unchanged throughout 72 hours. This limited C_3A consumption is consistent with the low hydration activity shown in Figure 4 and contributes to insufficient early-age hydration-product formation, limiting the development of a connected microstructure and resulting in reduced compressive strength.

The results are consistent with the literature regarding the very high reactivity of C3A during the first few hours and its substantial contribution to early heat release; C3A is identified as the most reactive clinker phase in Portland cement and has a pronounced influence on early-age heat development and rheological evolution. The sharp decrease observed during the first 18 hours is also consistent with studies indicating that C3A rapidly forms ettringite (AFt) upon contact with water, followed by AFm/hydrogarnet-type products; this process accounts for the aluminate peak observed in calorimetric measurements (Ming et al., 2024).

Figure 9. Time-dependent variation of C3A in mortars with varying proportions of FA admixture.



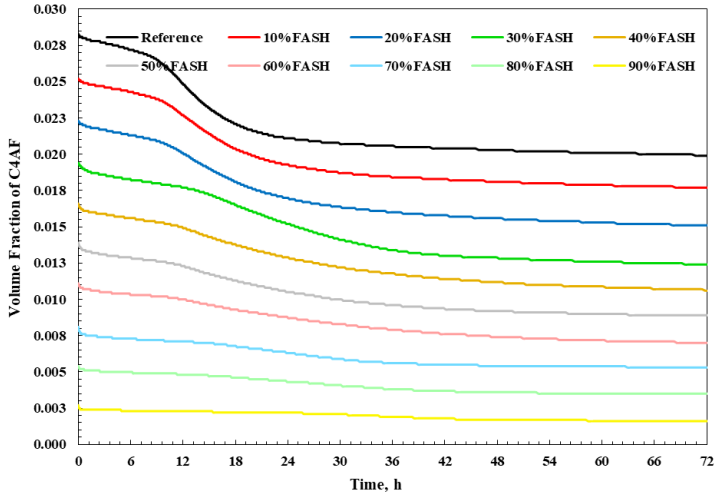
The calculated evolution of the unhydrated tetracalcium aluminoferrite (C_4AF) volume fraction over 72 hours, as a function of

fly ash (FASH) replacement, is presented in Figure 10. The depletion profile shows delayed and low-intensity consumption, resembling the sluggish behavior of C_2S (Figure 8) and contrasting with the rapid C_3A depletion shown in Figure 9. For the reference mixture (0% FASH), the initial C_4AF volume fraction is approximately 0.028. During the first 12 hours, the C_4AF fraction remains nearly unchanged. Between 12 and 24 hours, moderate consumption reduces the fraction to approximately 0.021, followed by a nearly constant plateau at about 0.020 through 72 hours. This behavior confirms the low early-age reactivity of C_4AF, which contributes only minimally to early heat release and space-filling hydration products, leaving a considerable amount unreacted in the microstructure.

As FASH replacement increases from 10% to 90%, the initial C_4AF volume fraction decreases due to clinker dilution. At low-to-intermediate replacement levels (10–50% FASH), the depletion curves remain nearly parallel, indicating that FA addition does not significantly accelerate C_4AF dissolution. At high replacement levels, particularly 70–90% FASH, C_4AF consumption is almost completely suppressed. The 90% FASH mixture starts at only about 0.002 and remains essentially unchanged over 72 hours. This lack of C_4AF hydration further limits early-age microstructural development and contributes to the pronounced reduction in compressive strength and Young's modulus at high FASH replacement levels.

The interpretation that tetracalcium aluminoferrite (C4AF) in the mixtures exhibits low reactivity and delayed consumption during the first 72 hours is largely consistent with the literature; C4AF is traditionally considered to have relatively low hydration reactivity in Portland cement, and a high ferrite content may delay early-age hydration (Zhang et al., 2024). The limited early-age consumption and plateau behavior are also supported by studies indicating that C4AF hydration involves a complex mechanism governed by the nucleation and growth of hydration products following dissolution (Ye et al., 2024). Furthermore, C3A has been reported to hydrate considerably faster than C4AF, with a pronounced difference in the hydration rates of the aluminate phases; therefore, the C4AF–C3A contrast presented in the text is well justified (Plowman & Cabrera, 1984).

Figure 10. Time-dependent variation of C4AF in mortars with varying proportions of FA admixture.



Phase Transformations and Synthesis of Early-Age Hydration Matrices

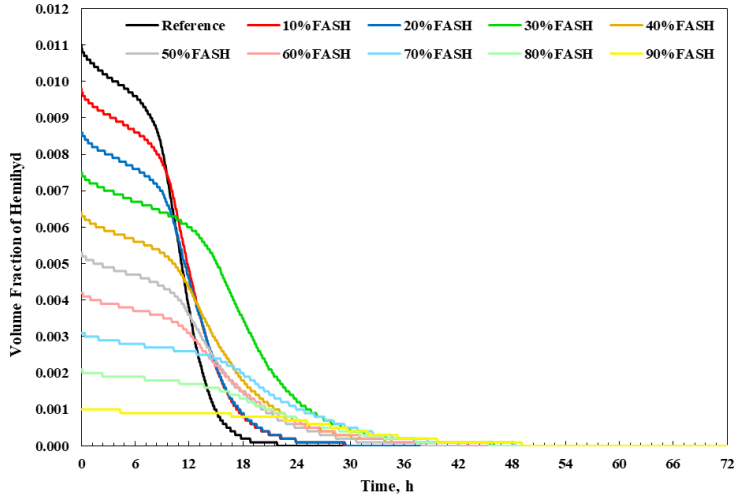
The numerical simulation results in Figure 11 show the time-dependent depletion of the hemihydrate volume fraction over 72 hours as a function of fly ash (FASH) replacement. The curves indicate a two-stage kinetic behavior, consisting of initial clinker dilution followed by different transformation rates depending on the FASH content. During the first 10 hours, the initial hemihydrate volume fraction decreases systematically with increasing FASH replacement. The reference mixture (0% FASH) starts at approximately 0.011, whereas the 90% FASH mixture begins at only about 0.001, confirming the direct dilution of the initial sulfate balance caused by Portland cement replacement.

A pronounced kinetic divergence occurs between 10 and 24 hours. The reference, 10%, and 20% FASH mixtures show rapid hemihydrate consumption after 10 hours, with the reference mixture approaching complete depletion around 18 hours. This behavior corresponds to the main exothermic hydration peak at 15 hours (Figure 4) and the rapid C_3A consumption shown in Figure 9, indicating that hemihydrate dissolution supplies sulfate ions required to regulate the highly reactive aluminate phases during early hydration. In contrast, intermediate replacement levels such as 30% FASH exhibit delayed

consumption, maintaining a higher plateau until approximately 18 hours. At high replacement levels (70–90% FASH), hemihydrate depletion follows a prolonged, step-like pattern due to the low hydration activity. Despite these differences, all mixtures converge after approximately 40 hours, reaching zero hemihydrate fraction and indicating its complete consumption across the simulated systems.

The decrease in the initial hemihydrate volume fraction with increasing fly ash content in the simulation is consistent with the literature indicating that fly ash volumetrically dilutes the cement and alters the initial sulfate balance of the system (Narmluk & Nawa, 2011). The sharp consumption observed between 10 and 24 hours in the reference and low-replacement mixtures is also an expected result, because hemihydrate dissolves more rapidly than gypsum, provides a higher sulfate concentration during the initial hours, promotes greater ettringite formation, and consequently advances the timing of the aluminate peak (Andrade Neto et al., 2021). Therefore, associating hemihydrate consumption with the rapid early-age hydration of C3A and the calorimetric peak is also strongly supported by the literature (Zunino & Scrivener, 2020).

Figure 11. Time-dependent hemihydrate transformation of mortars containing FA at different ratios.



The numerical simulation results in Figure 12 show the progressive precipitation of calcium hydroxide (CH) in the modeled

binder matrix over 72 hours as a function of fly ash (FASH) replacement. The reference mixture (0% FASH) exhibits the highest CH development, with a sharp increase after a 6-hour induction period that continues until approximately 24 hours. This behavior corresponds closely to the rapid C_3S depletion shown in Figure 7 and the main exothermic hydration peak in Figure 4. At 72 hours, the reference mixture reaches a maximum CH volume fraction of approximately 0.123.

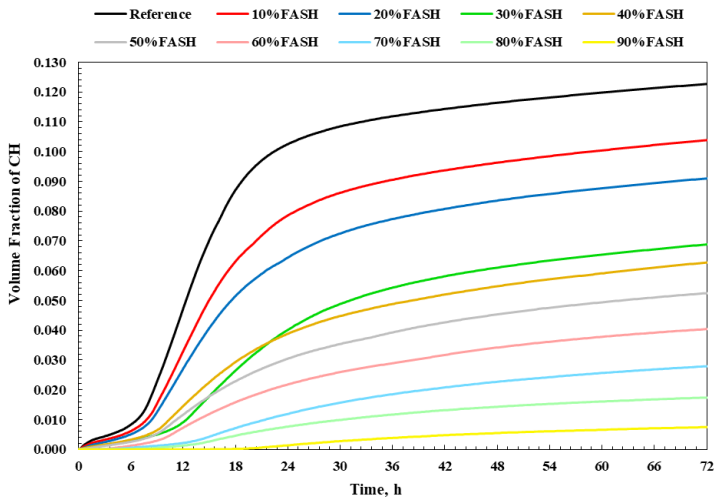
As FASH replacement increases, CH accumulation decreases systematically, with each 10% increase in FASH reducing both the formation rate and final CH volume fraction. At 40% FASH, the 72-hour CH content decreases to approximately 0.062, nearly half that of the reference mixture. At high replacement levels (70–90% FASH), CH precipitation is strongly suppressed. The 90% FASH mixture remains nearly inactive until 24 hours and reaches only about 0.007 at 72 hours. This substantial reduction in CH formation indicates limited primary clinker hydration and helps explain the high residual porosity and reduced compressive strength observed at high FASH replacement levels.

The interpretation that the rapid increase in CH during the first few hours in the reference mixture is primarily attributable to primary clinker hydration, particularly early silicate reactions associated with heat evolution, is consistent with the literature (Wu et al., 2025). The systematic decrease in CH formation and the final CH level at 72 hours with increasing fly ash content is also broadly supported by previous studies; experimental, modeling, and microstructural investigations have demonstrated that higher fly ash contents generally result in lower heat evolution, degree of hydration, and CH content (Moghaddam et al., 2019). This trend can be attributed to the fact that fly ash remains largely inert during the early ages in most systems, while its effects primarily arise from dilution and changes in pore-solution chemistry (Deschner et al., 2012).

The transient simulation results in Figure 13 show the nucleation and growth of calcium silicate hydrate (CSH) gel over 72 hours. In the reference mixture (0% FASH), CSH formation accelerates sharply after a 6-hour dormant period, with the main production

occurring between 6 and 24 hours. This process corresponds to the rapid C_3S consumption shown in Figure 7 and the main heat evolution peak at 15 hours in Figure 4. At 72 hours, the reference mixture reaches a maximum CSH volume fraction of approximately 0.311.

Figure 12. Time-dependent variation of CH in mortars with varying proportions of FA admixture.

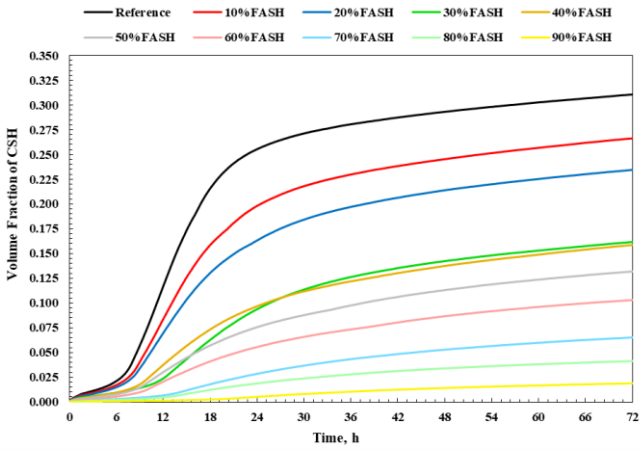


The transient simulation results in Figure 13 show the nucleation and growth of calcium silicate hydrate (CSH) gel over 72 hours. In the reference mixture (0% FASH), CSH formation accelerates sharply after a 6-hour dormant period, with the main production occurring between 6 and 24 hours. This process corresponds to the rapid C_3S consumption shown in Figure 7 and the main heat evolution peak at 15 hours in Figure 4. At 72 hours, the reference mixture reaches a maximum CSH volume fraction of approximately 0.311.

Increasing FASH replacement progressively suppresses CSH formation. At 40% FASH, CSH development is delayed by approximately 15 hours and reaches only 0.158 at 72 hours. At high replacement levels (70–90% FASH), CSH accumulation becomes minimal; the 90% FASH mixture reaches only about 0.018. The reduced CSH formation is consistent with the flattened hydration temperature profiles (Figure 4), persistent high porosity (Figure 6), and the ~70% reduction in compressive strength at high FASH contents.

Atomistic and kinetic studies have demonstrated that C-S-H nucleation and growth control hydration kinetics, that C-S-H formation can accelerate silicate dissolution, and that the main hydration peak results from the combined effects of C_3S dissolution and C-S-H growth (Shen et al., 2022). The relationship between the sharp accumulation of C-S-H in the reference mixture over the 6–24 h period and the 15-h exothermic peak is also supported by early-age calorimetry and kinetic modeling studies (Wu et al., 2025). The downward shift of the C-S-H accumulation curves with increasing fly ash content is also consistent with the general trend reported in the literature; high replacement levels reduce the nucleation density at early ages, suppress C-S-H nucleation and growth, and extend the induction period (Wu et al., 2025).

Figure 13. Time-dependent variation of CSH in mortars with varying proportions of FA admixture.

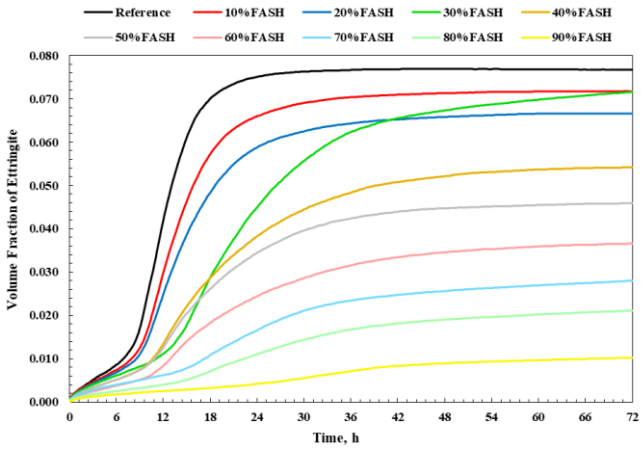


An examination of the crystallization profiles captured in Figure 14 highlights how fly ash (FASH) replacement alters ettringite nucleation kinetics over 72 hours. The control matrix establishes a rapid growth trajectory, accelerating sharply between 6 and 18 hours to stabilize at a maximum volume fraction of approximately 0.076. This rapid accumulation window directly corresponds to the early depletion of the highly reactive aluminate phase (C3A) observed in Figure 9.

As clinker content is diluted, the total ettringite volume decreases systematically. Interestingly, the 30% FASH blend exhibits a delayed acceleration but undergoes a late kinetic crossover, matching the 10% FASH curve at roughly 0.072 by the 72-hour terminal

threshold. Conversely, at extreme substitution levels (70% to 90% FASH), ettringite synthesis is heavily suppressed, with the 90% FASH profile flattening beneath a baseline of 0.010, indicating that excessive dilution severely restricts early crystalline framework development. In the control mixture, ettringite rapidly accumulates, consistently with the rapid early hydration of C_3A, while the early-age kinetics are progressively delayed with increasing fly ash content, accurately reflecting the observed hydration behavior (Wu et al., 2025). However, the literature indicates that fly ash does not necessarily reduce ettringite formation at moderate replacement levels; in the presence of sulfate, alumina, and limestone, delayed but sustained, and in some cases stabilized, AFt formation may occur (Feng & Xu, 2025). In contrast, the suppression of early-age hydration and nucleation at very high replacement levels supports a substantial restriction of ettringite formation (De la Varga et al., 2018).

Figure 14. Time-dependent ettringite variation in mortars with varying proportions of FA additives.



Conclusions

Based on the multi-phase numerical simulations of cement pastes incorporating up to 90% fly ash (FASH) replacement over a 72-hour hydration period, the following conclusions are drawn:

Thermal and Kinetic Suppression: Increasing FASH content systematically diminishes early-age hydration kinetics. The maximum exothermic peak falls from 60.8 °C (0% FASH) to a nearly horizontal

profile at 90% substitution, which completely suppresses chemical heat release.

Phase Depletion and Retardation: Volumetric dilution drastically restricts the chemical dissolution of major clinker components. Unreacted fractions of C3S, C2S, C3A, and C4AF exhibit up to a 90% drop in early consumption rates. Concurrently, initial sülfat regulation is altered, with hemihydrate depleting universally across all blends within 40 hours.

Microstructural Degradation: The severe reduction in clinker hydration limits the precipitation of essential space-filling binder networks. The accumulation of CSH gel and crystalline CH drops by roughly 94% at maximum replacement, while ettringite growth decreases by 87%. Consequently, the framework fails to form interconnecting structural bridges.

Physical and Mechanical Softening: This lack of primary hydration gel leaves the microstructural matrix highly porous. Terminal capillary porosity spikes from 0.285 to a loose plateau over 0.50. This structural instability triggers an accelerated 70% linear drop in bulk compressive strength and Young's modulus, alongside a sharp increase in lateral Poisson's ratio.

Synthesizing these numerical and phase outcomes, a fly ash replacement threshold exceeding 20% severely degrades early-age properties, making higher substitution ratios unfavorable for structural configurations requiring early skeletal stability.

References

Andrade Neto, J. da S., De la Torre, A. G., & Kirchheim, A. P. (2021). Effects of sulfates on the hydration of Portland cement – A review. *Construction and Building Materials*, *279*, 122428. https://doi.org/10.1016/j.conbuildmat.2021.122428

Bu, J., Liu, Q., Zhang, L., Li, S., & Zhang, L. (2025). Dynamic Compressive Behavior and Fracture Mechanisms of Binary Mineral Admixture-Modified Concrete. *Materials*, *18*(12), 2883. https://doi.org/10.3390/ma18122883

Bullard, J. W. (2014). Virtual Cement and Concrete Testing Laboratory. *National Institute of Standards and Technology (NIST) Special Publication 1173*, 1–55.

De la Varga, I., Castro, J., Bentz, D. P., Zunino, F., & Weiss, J. (2018). Evaluating the hydration of high volume fly ash mixtures using chemically inert fillers. *Construction and Building Materials*, *161*, 221–228. https://doi.org/10.1016/j.conbuildmat.2017.11.132

Deschner, F., Winnefeld, F., Lothenbach, B., Seufert, S., Schwesig, P., Dittrich, S., Goetz-Neunhoeffer, F., & Neubauer, J. (2012). Hydration of Portland cement with high replacement by siliceous fly ash. *Cement and Concrete Research*, *42*(10), 1389–1400. https://doi.org/10.1016/j.cemconres.2012.06.009

Feng, S., & Xu, L. (2025). Influence of coal fly ash on early-age and late-age hydration of Portland cement. *Cement Wapno Beton*, *29*(6), 413–430. https://doi.org/10.32047/CWB.2024.29.6.4

Huang, H.-S., Peng, Y., Zhang, X.-C., & Chen, X.-F. (2026). Age-Dependent Effects of Graphene Oxide on Hydration-Gel Evolution and Strength Development of Fly Ash-Blended Cementitious Materials. *Gels*, *12*(4), 312. https://doi.org/10.3390/gels12040312

Kapeluszna, E., & Kotwica, Ł. (2024). New insights into the role of highly reactive pozzolans in the early hydration process of C3S and C3A monitored by conductometry, calorimetry, phase

composition and microstructure analyses. *Construction and Building Materials*, *452*, 138950. https://doi.org/10.1016/j.conbuildmat.2024.138950

Kuryłowicz-Cudowska, A. (2022). Correlation between Compressive Strength and Heat of Hydration of Cement Mortars with Siliceous Fly Ash. *Minerals*, *12*(11), 1471. https://doi.org/10.3390/min12111471

Maysyurah, A., Aris, M., Fajar, M. N., Arifin, H., & Setya, D. (2025). Effect of Blended Cement Containing Fly Ash on the Elastic Modulus and Poisson's Ratio of Mortar. *Bentang : Jurnal Teoritis Dan Terapan Bidang Rekayasa Sipil*, *13*(2), 183–194. https://doi.org/10.33558/bentang.v13i2.11001

Ming, X., Yu, Q., Huo, P., Si, W., Li, Z., & Sun, G. (2024). Early-age hydration of tricalcium aluminate in chloride solutions. *Cement and Concrete Research*, *184*, 107626. https://doi.org/10.1016/j.cemconres.2024.107626

Moghaddam, F., Sirivivatnanon, V., & Vessalas, K. (2019). The effect of fly ash fineness on heat of hydration, microstructure, flow and compressive strength of blended cement pastes. *Case Studies in Construction Materials*, *10*, e00218. https://doi.org/10.1016/j.cscm.2019.e00218

Narmluk, M., & Nawa, T. (2011). Effect of fly ash on the kinetics of Portland cement hydration at different curing temperatures. *Cement and Concrete Research*, *41*(6), 579–589. https://doi.org/10.1016/j.cemconres.2011.02.005

Plowman, C., & Cabrera, J. G. (1984). Mechanism and kinetics of hydration of C3A and C4AF. Extracted from cement. *Cement and Concrete Research*, *14*(2), 238–248. https://doi.org/10.1016/0008-8846(84)90110-8

Quan, J., Fu, S., Chen, J., Yang, R., Luo, T., & Wang, D. (2023). Influence Mechanism of Initial Concreting Temperature and Water-Binder Ratio on Hydration Rate of Fly Ash Concrete. *Materials*, *16*(12), 4286. https://doi.org/10.3390/ma16124286

Shen, D., Wang, X., & Wu, S. (2022). Determining

hydration mechanisms for initial fall and main hydration peak in tricalcium silicate hydration using a two-scale hydration simulation model. *Cement and Concrete Research, 156*, 106763. https://doi.org/10.1016/j.cemconres.2022.106763

Wu, C.-R., Xiao, Z.-P., Wei, J.-J., Kou, S.-C., & Tang, M.-X. (2025). Early Hydration Behaviours and Kinetics of Portland Cement Composites Incorporating Low-Calcium Circulating Fluidized Bed Fly Ash. *Journal of Composites Science, 9*(12), 671. https://doi.org/10.3390/jcs9120671

Yang, C., You, J.-J., Huang, Y.-W., Ji, X.-M., Song, Q.-Y., & Liu, Q. (2023). Low-carbon enhancement of fly ash geopolymer concrete: Lateral deformation, microstructure evolution and environmental impact. *Journal of Cleaner Production, 422*, 138610. https://doi.org/10.1016/j.jclepro.2023.138610

Ye, S., Feng, P., & Liu, J. (2024). Dissolution and early hydration of tetracalcium aluminoferrite (C4AF) in water and in aqueous sulfate solutions. *Cement and Concrete Research, 186*, 107676. https://doi.org/10.1016/j.cemconres.2024.107676

Yu, Z., & Ye, G. (2013). The pore structure of cement paste blended with fly ash. *Construction and Building Materials, 45*, 30–35. https://doi.org/10.1016/j.conbuildmat.2013.04.012

Zhang, K., Wang, C., & Huang, X. (2024). Insight into discrepancies in hydration reactivity of ferrite phase in Portland cement clinker and synthetics. *Construction and Building Materials*, *412*, 134674. https://doi.org/10.1016/j.conbuildmat.2023.134674

Zhao, H., Qin, X., Liu, J., Zhou, L., Tian, Q., & Wang, P. (2018). Pore structure characterization of early-age cement pastes blended with high-volume fly ash. *Construction and Building Materials*, *189*, 934–946. https://doi.org/10.1016/j.conbuildmat.2018.09.023

Zou, F., Hu, C., Wang, F., Ruan, Y., & Hu, S. (2020). Enhancement of early-age strength of the high content fly ash blended cement paste by sodium sulfate and C–S–H seeds towards a greener binder. *Journal of Cleaner Production, 244*, 118566.

https://doi.org/10.1016/j.jclepro.2019.118566

Zunino, F., & Scrivener, K. (2020). Factors influencing the sulfate balance in pure phase C3S/C3A systems. *Cement and Concrete Research*, *133*, 106085. https://doi.org/10.1016/j.cemconres.2020.106085

BÖLÜM 2

EFFECT OF PILE SPACING ON THE BEHAVIOR OF QUAY PILES UNDER LINEAR WAVE LOADING

MUHAMMET ENSAR YİĞİT [1]
ÜMİT GÖKKUŞ [2]

Introduction

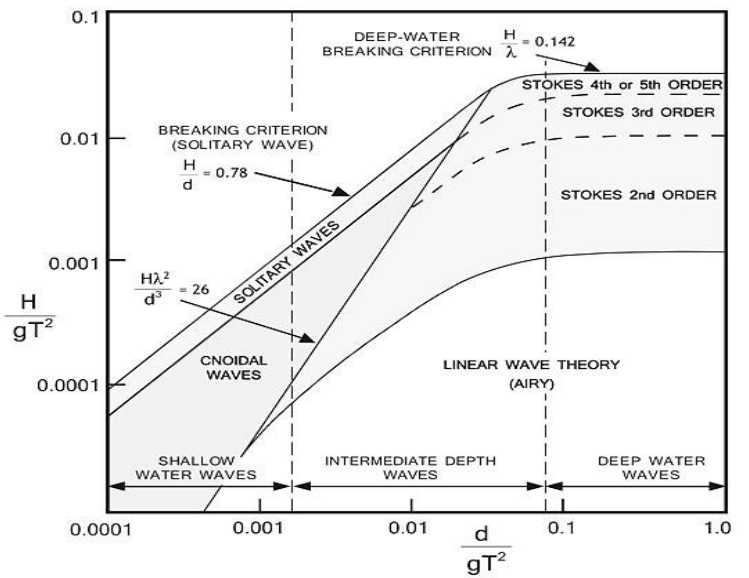
The literature contains numerous studies addressing wave-induced hydrodynamic effects around piles used in dock and quay structures. For cylindrical piles subjected to wave action under unsteady flow conditions, the resulting hydrodynamic forces can be estimated theoretically using various wave theories. These theories are generally classified into two categories: small-amplitude wave theories and finite-amplitude wave theories. In wave statistics and design procedures, the characteristic wave parameters, particularly wave height and wave period, are selected based on their probability of occurrence and the associated level of risk. In addition, the design wave conditions depend strongly on the water depth at the pile installation location. Consequently, the selection of appropriate

[1] Corresponding, Associate Professor, Manisa Celal Bayar University, Engineering and Natural Sci. Faculty, Civil Engineering Department, Manisa/Türkiye, Orcid: 0000-0003-0161-7144 ensar.yigit@cbu.edu.tr
[2] Retired Professor, Orcid: 0000-0002-2422-6392 pentaprofcon@gmail.com

design wave parameters is a critical factor in determining the hydrodynamic forces acting on the piles.

The Le-Méhauté diagram (Figure 1), which defines the applicability ranges of different wave theories, indicates that a pile installed at a given water depth may be subjected to wave conditions corresponding to more than one wave theory throughout its service life. This depends primarily on the values of the dimensionless parameters (d/gT^2) and (H/gT^2). Even at a constant water depth, variations in the design wave height and period may result in different applicable wave theories. Such variations can lead to changes in the hydrodynamic loading along the pile due to differences in wave-induced particle velocities and accelerations. Therefore, the design of cylindrical steel dock piles should consider the range of hydrodynamic forces that may develop under different design wave conditions throughout their expected service life.

Figure 1. Limits of validity of wave theories (Le-Mehaute, 1969).



Steel cylindrical dock piles operating in marine environments are subjected to several types of loading, including hydrodynamic and hydraulic actions, ship berthing forces, seismic effects, operational loads, and lateral soil pressures. Among these, hydraulic-hydrodynamic and lateral soil loads are particularly important in fluid–structure interaction analyses. For hydrodynamic loading, the flow regime, whether steady or unsteady, must be appropriately defined, while the mechanical response of the seabed requires consideration of whether the soil behaves as an elastic medium or undergoes liquefaction. Accordingly, fluid–structure interaction modelling of cylindrical steel dock piles requires the dynamic behavior of both water and surrounding soil to be adequately represented along the pile length. Such problems can be investigated analytically by formulating equations of motion using single-degree-of-freedom (SDOF) or multi-degree-of-freedom (MDOF) systems, or numerically through computational approaches based on finite difference, finite element, boundary element, and finite volume methods.

Material and method

Mathematical Model for the Movement of Dock Piles

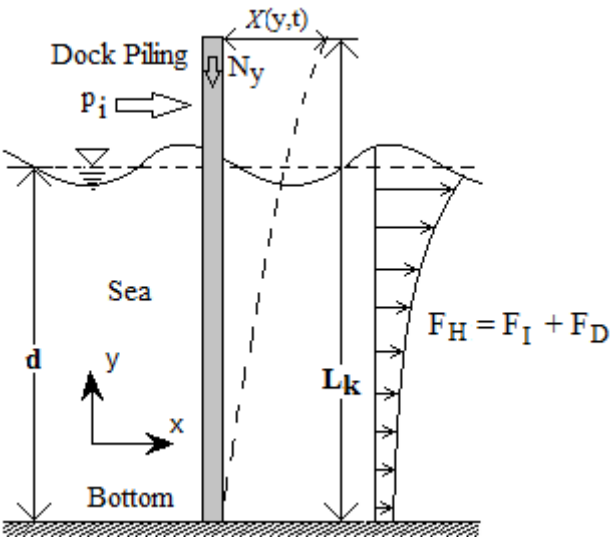
The dynamic response of an individual dock pile under time-dependent loads can be described using generalized mass, damping, stiffness, and external force parameters. These properties may vary along the pile and can be obtained by integrating their spatial distributions over its length. Accordingly, the displacement response can be expressed as functions of position and time, with the displacement function separated into spatial and temporal components following Clough and Penzien (1993).

$$X_D(y,t) = \psi(y)X(t) \tag{1}$$

Here, $\psi(y)$ represents the spatial shape function, whereas $X(t)$ denotes the time-dependent vibration function (Figure 2). Based on this separation, the governing equation of motion can be expressed in the form of a generalized single-degree-of-freedom (SDOF) system.

$$m^* \frac{\partial^2 X}{\partial t^2} + c^* \frac{\partial X}{\partial t} + k^* X(t) = F^*(t) \tag{2}$$

Figure 2. Single dock pile and acting loads.



The resulting equation of motion can be formulated in dynamic form and solved using either analytical or numerical approaches. The generalized mass, damping, stiffness, and external force terms are determined by considering their spatial and temporal dependencies, following the formulation given by Clough and Penzien (1993).

$$m^* = \int_0^{Lk} m_S(y)\psi(y)^2 dy + \frac{N_y}{g} \tag{3}$$

$$c^* = a_1 E \int_0^{Lk} I_m(y) \left(\frac{\partial^2 \psi}{\partial y^2}\right)^2 dy \tag{4}$$

$$k^* = E\int_0^{Lk} I_m(y)\left(\frac{\partial^2\psi}{\partial y^2}\right)^2 dy - N_y\int_0^{Lk}\left(\frac{\partial\psi}{\partial y}\right)^2 dy \quad (5)$$

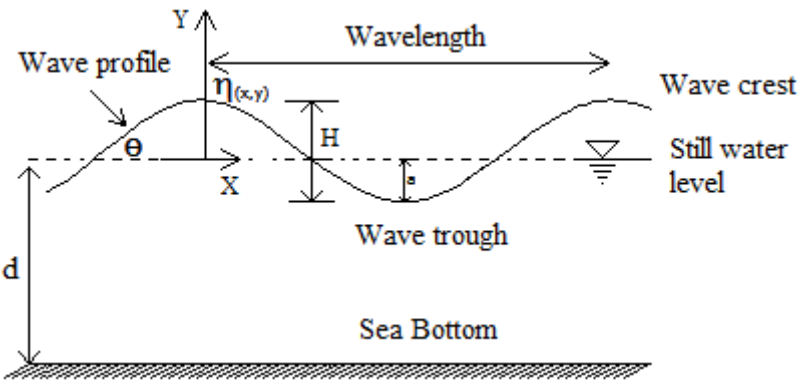
$$F^*(t) = \sum p_i(t)\psi_i(y) + \int_0^d F_H(y,t)\psi(y)dy \quad (6)$$

Here; m^*: generalized mass, c^*: generalized damping, k^*: generalized rigidity, m_S: structural mass, a_1: damping coefficient, $F^*(t)$: external load, X_D: displacement, g: gravitational acceleration, γ_d: sea water unit volume weight$E$: elasticity modulus, , N_y: axial load, I_m: moment of inertiaL_k: pile length, , d: water depth, p_i: singular force in x-direction, $F_I(y,t)$: hydrodynamic inertia force, $F_D(y,t)$: hydrodynamic drag force (Ölmez, Yiğit, & Solmaz, 2011).

Wave Theories

The selection of an appropriate wave theory depends primarily on the local water depth, wave period, and wave height (Figure 3). For pile-based coastal structure analyses, these parameters can be evaluated at the installation depth of each pile to determine the applicable wave theory.

Figure 3. General definition of linear wave parameters.



The wave field is assumed to be two-dimensional in the (x)-(y) plane over a flat, undisturbed seabed, with waves propagating in the positive (x)-direction (Figure 1). The water depth (*d*), wave

period (T), height (H), and wavelength (L) define the principal wave parameters. The propagation speed is determined by the relationship between wavelength and period and is expressed as follows.

$$c = L/T \tag{7}$$

If the boundary value problem is summarized as two-dimensional.

Differential (Laplace) equation: $$\frac{\partial^2 \Phi}{\partial x^2} + \frac{\partial^2 \Phi}{\partial y^2} + \frac{\partial^2 \Phi}{\partial z^2} = 0 \tag{8}$$

Base boundary condition: for $y = -d$ $$\partial \Phi / \partial y = 0 \tag{9}$$

Free surface kinematic condition: f*or* $y=\eta$

$$\frac{\partial \eta}{\partial t} + \frac{\partial \Phi}{\partial x}\frac{\partial \eta}{\partial x} - \frac{\partial \Phi}{\partial y} = 0 \tag{10}$$

Free surface dynamic condition: for $y=\eta$

$$\frac{\partial \Phi}{\partial t} + \frac{1}{2}\left[\left(\frac{\partial \Phi}{\partial x}\right)^2 - \left(\frac{\partial \Phi}{\partial y}\right)^2\right] + g\eta = 0 \tag{11}$$

Relations can be obtained. Here Φ is the velocity potential. The potential function must satisfy the Laplace equation and three boundary conditions (Russell, 1844) (Karaturp, 2007).

Linear Wave Theory

For a given wave theory, the flow field is characterized by determining the velocity potential (Φ) or, equivalently, the stream function (Ψ). The formulation of the linear (Stokes first-order) wave theory follows Chakrabarti (1987). Accordingly, the free-surface elevation (η) and wavelength (L) are obtained from Equations (12) and (14), respectively (Stokes, 1980).

$$\eta = \frac{H}{2} cos\, \Theta \{\Theta = (kx - \omega t), \tag{12}$$

$$k = \frac{2\pi}{L}, \qquad \omega = \frac{2\pi}{T} \tag{13}$$

$$L = \frac{gT^2}{2\pi} tanh\, k\, d \tag{14}$$

As seen in Equation (14), the wavelength can be calculated depending on T and d. The velocity and acceleration of a fluid particle in the x-direction are expressed as follows.

$$u = \frac{\pi H}{T} \frac{cosh\, ks}{sinh\, kd} cos\, \Theta \tag{15}$$

$$\frac{\partial u}{\partial t} = \frac{2\pi^2 H}{T^2} \frac{cosh\, ks}{sinh\, kd} sin\, \Theta \tag{16}$$

Here, s represents the height from the sea floor. The hydrodynamic pressure (p) formed on the sea floor is given in equation (17) according to the first order.

$$p = \rho g \frac{H}{2} \frac{cosh\, ks}{cosh\, kd} cos\, \Theta \tag{17}$$

Hydrodynamic Wave Forces

Wave-induced forces on piles are primarily governed by water-particle velocity and acceleration. For vertical piles, the horizontal flow components, pile diameter (D), and fluid properties such as density ($\rho = \gamma/g$) and kinematic viscosity (υ) are key parameters. Following Morison et al. (1950), the hydrodynamic load consists mainly of drag and inertia components, which can be expressed per unit pile width as follows (Morison, 1950):

$$F_D = \frac{1}{2} C_D \rho_d D u|u| \quad , \qquad F_I = \frac{\pi D^2}{4} C_M \rho_d \frac{\partial u}{\partial t} \tag{18}$$

It is expressed by the formula (Morison, 1950) (Tsuchiya & Yasuda, 1980). Here, C_D: Drag coefficient, C_M: Inertia coefficient, ρ_d: Unit volume weight of water. Other quantities are as defined before.

Hydraulic Modelling

Abaqus/CFD finite element software was used to calculate the fluid characteristics (Gökkuş, Yiğit, & Gücüyen, 2017).

Conservation of mass; $$\nabla V = 0 \quad (19)$$

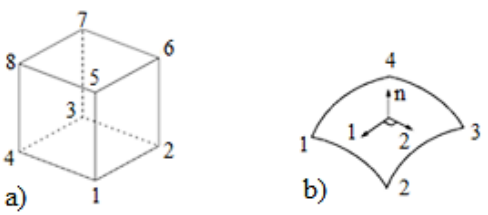
Conservation of momentum; $$\left(\frac{\partial V}{\partial t} + V \times \nabla V\right) = \nabla \sigma + \rho g \quad (20)$$

Conservation of energy; $$\frac{\partial E}{\partial t} + \nabla\left(V(E_t + P)\right) = 0 \quad (21)$$

The governing equations were numerically solved using the finite element approach implemented in the selected software, while the prescribed boundary conditions were incorporated into the computational procedure. Here, *V:* denotes the velocity vector, *P:* represents pressure, E_t: is the total energy, *t*: denotes time, and σ: corresponds to surface tension.

The fluid domain is discretized using three-dimensional continuum hexahedral elements of type FC3D8, while the cylindrical dock pile is represented by four-node reduced-integration shell elements (S4R) with a defined wall thickness (Figure 4). In the FC3D8 designation, "*F*" fluid, "*C*" continuous, "3D" three-dimensional continuum, and "8" the number of nodes. Similarly, S4R represents a shell element with four nodes and reduced integration. These element formulations are suitable for fluid and pipe-section modelling, respectively (Abaqus, 2014).

Figure 4. a) Fluid element geometry, b) Shell element geometry



Modelling Fluid-Structure Interaction

The fluid–structure interaction is defined by specifying the contact surfaces between the fluid and pile, allowing hydrodynamic forces and structural deformations to be exchanged during the coupled solution. In the fluid solver, the subscript (*f*) denotes the fluid domain, and the flow-induced forces acting on the pile are obtained from the governing fluid equations (Abaqus, 2014).

$$k_f u_f = F_f(t) \tag{22}$$

The fluid displacement (u_f) is determined as a function of pressure (p), velocity components ($\dot{u}_x\ \dot{u}_y\ \dot{u}_z$), temperature ($T_a$), and time ($t$).

$$u_f = \{p\dot{u}_x\dot{u}_y\dot{u}_z T_a\}^t \tag{23}$$

The resulting fluid forces are subsequently transferred to the structural solver, where the pile response is calculated using the corresponding equation of motion (Gökkuş, Yiğit, & Gücüyen, 2017).

$$m_S \frac{\partial^2 u}{\partial t^2} + c_S \frac{\partial u}{\partial t} + k_S u = F_{FS}(t) \tag{24}$$

The structural displacement is determined from the corresponding governing equation. The interaction between the fluid and structural domains is established by transferring the relevant solution variables between the two computational domains. In this formulation, $F_{FS}\ (t)$ denotes the hydrodynamic force acting on the solid body as a function of time, while the subscript "*s*" refers to the structural domain. All remaining variables are defined as stated previously.

Von-Mises Stresses on Pile in Fluid-Structure Interaction

According to the von Mises criterion, yielding occurs when the distortion (deviatoric) strain energy reaches a critical value,

making it particularly applicable to ductile materials (von Mises, 1913).

$$W = \frac{1}{2}\sigma' : \varepsilon' \tag{25}$$

Since von Mises stress is governed by the deviatoric stress components, Hooke's law can be incorporated to express the strain energy independently of displacement.

$$\varepsilon' = \frac{1}{2G}\sigma' \tag{26}$$

Although von Mises stress can be formulated in several equivalent forms, Abaqus evaluates it using the following expressions.

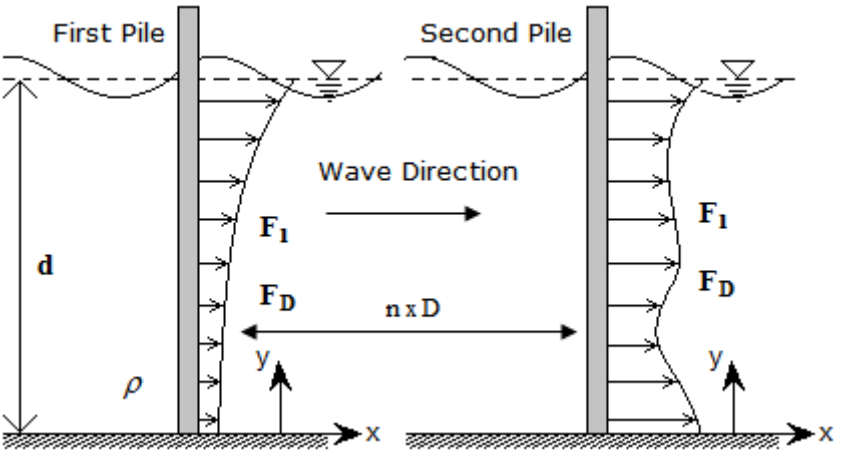
$$\sigma_{VM} = \sqrt{\frac{3}{2}\sigma_{ij}\sigma_{ij} - \frac{1}{2}(\sigma_{kk})^2} \tag{27}$$

Case Study

In this section, three models with different pile spacings are analyzed to determine the flow velocity and pressure distribution around successive pier piles in a marine environment, and the displacement and stress values that will be created on the piles by hydrodynamic loads calculated according to linear wave theory. The displacement and stress values of successive pier piles under the influence of hydrodynamic forces are calculated according to the distance between the piles. Successive pier piles with fixed supports, having a circular cross-sectional diameter D=1.0 m and a height L=30 m, are placed in a wavy marine environment with rectangular cross-sectional dimensions (X,Y, Z) = (50 m, 25 m, 5 m) (Figure 7). Within the finite element framework, the seawater domain is simulated using the Computational Fluid Dynamics (Abaqus/CFD) solver, whereas the pier pile is analyzed through the Dynamic Finite Element (Abaqus/Explicit) solver. This coupled numerical formulation enables the fluid and structural domains to be considered simultaneously. According to the scheme shown in

Figure 5, the displacement and stress values of the piles will be examined in relation to the fluid velocity and pressure.

Figure 5. Schematic representation of consecutive quay piles.



Material Section and Properties

The mechanical properties assigned to the pile component are summarized in Table 1, while the corresponding seawater properties adopted in the numerical model are listed in Table 2. The wave characteristics considered in the numerical simulations based on linear wave theory are presented in Table 3. For the circular pile, the drag and inertia coefficients were specified as C_D = 1.16 and C_M = 2.0, respectively (Yiğit & Gökkuş, 2025) (Yiğit & Gökkuş, 2026) (Altiok, Cetin, & Demir, 2025).

Table 1. Pile parameters (Yiğit, 2019).

ρ_k (t/m³)	γ_k (kN/m³)	D (m)	s (m)	E (kN/m²)	N_y (kN)	ν
7.834	76.85	1.00	0.014	2.1x10⁸	700.0	0.3

Table 2. Water parameters (Yiğit, 2019).

C_0 (m/s)	κ	Γ_0	ρ (t/m³)	γ (kN/m³)	μ (N.s/m²)
1450	0	0	1.029	10.09	$1.002x10^{-3}$

Table 3. Linear Wave parameters (Yiğit, 2019).

H (m)	T (s)	d (m)	ρ_d (t/m³)	γ_d (kN/m³)
0.4	9	25.0	1.029	10.09

Mesh Design

The fluid domain is discretized using hexahedral FC3D8 elements, while the dock pile is modeled with four-node S4R shell elements (Figure 6). To ensure accurate fluid–structure interaction, a finer mesh is adopted near the fluid–pile contact interface.

Figure 6. Mesh structure of the marine-pile interaction model.

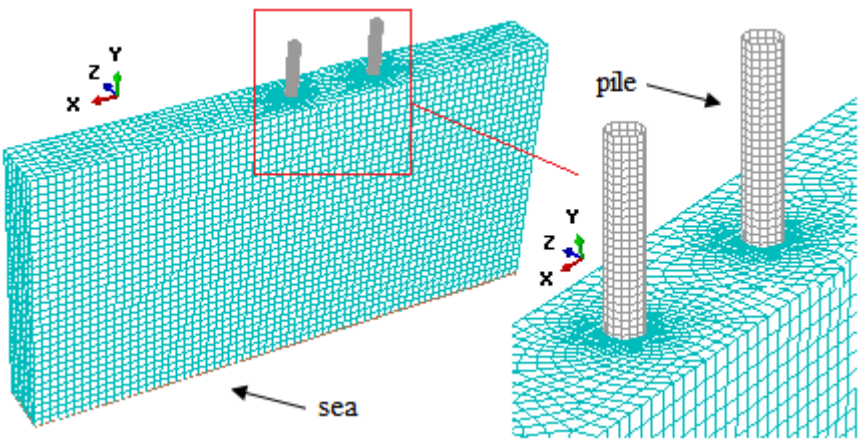
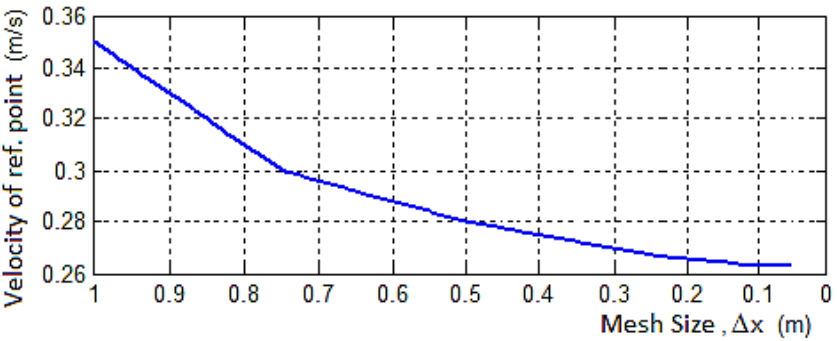


Figure 7. Convergence analysis.



As illustrated in Figure 8, a nominal mesh size of 0.50 m was adopted throughout the computational domain, while a finer element size of 0.10 m was employed in the vicinity of the pile to improve the accuracy of the numerical results. The seawater domain consisted of 115,659 nodes and 105,210 elements, whereas the steel dock pile was discretized into 12,276 nodes and 12,245 elements. These intervals were determined by the convergence analysis (Figure 7). Convergence analysis verifies the reliability and network independence of numerical results. (Altıok, 2019).

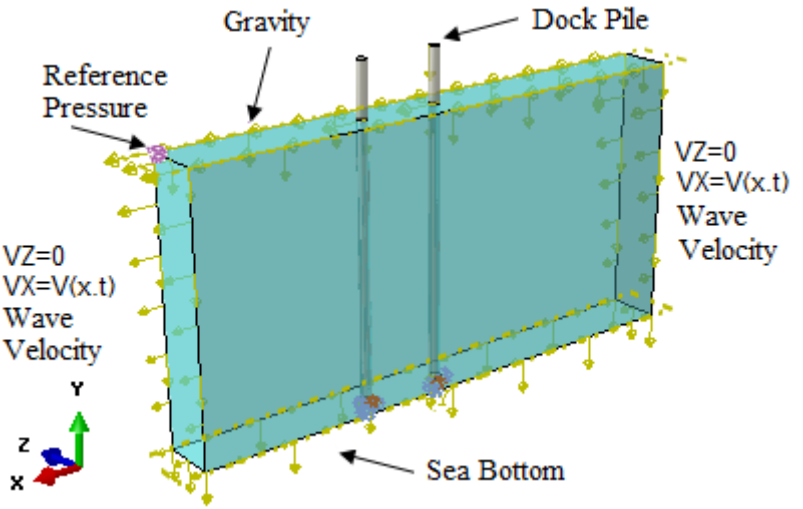
Boundary Conditions

For the numerical model presented in Figure 8, the velocity component in the *z*-direction was constrained to zero $V_Z=0$. A gravitational acceleration of ($g_Y = -9.81 m/s^2$) was imposed along the vertical (*y*)-axis. The bottom boundary of the computational domain was assigned a fixed support condition, with all translational degrees of freedom constrained ($U_X = U_Y = U_Z = 0$).

At the still-water level, the reference pressure was set to (P_{ref}= 0 kN/m^2). The pile was considered free at its upper end, whereas its lower end was fully restrained at the seabed. Accordingly, the seabed connection was defined by fixing both

translational and rotational degrees of freedom ($U_X = U_Y = U_Z = 0$), ($R_X = R_Y = R_Z = 0$).

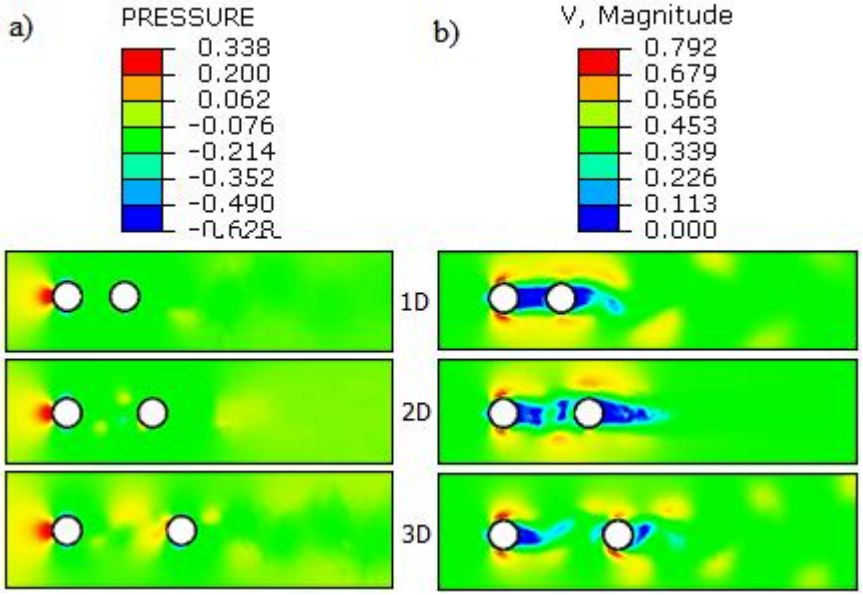
Figure 8. Boundary conditions.



Results

Figure 9 presents the pressure and velocity distributions on successive piles for different (D) spacings using contour plots. The displacement and stress distributions are presented as contour plots in Figures 10–11 and as graphical results in Figures 12–14. These results provide a comprehensive representation of the hydrodynamic response of the pile system and the interaction effects associated with different pile spacings. The obtained distributions also allow the variation of hydrodynamic effects along the pile length to be evaluated. In particular, the changes in pressure and velocity provide an indication of the load transfer between the fluid and pile. The results are subsequently used to assess the influence of pile spacing on the overall structural response.

Figure 9. a) Fluid pressure (kN/m^2) and b) Velocity (m/s) distribution around successive piles.



In Figure 9-a, as the fluid passes around the pile, the water particles encounter an obstacle in the upstream direction, resulting in the highest-pressure value at this point. As the water particles spread to both sides of the pile and continue flowing, the lowest pressure values are observed as negative pressure. In the downstream direction, a vortex forms, and negative pressure is observed here as well.

Similarly, in Figure 9-b, as the fluid passes around the pile, the water particles encounter an obstacle in the upstream direction, resulting in a slower particle velocity. As the water particles spread to both sides of the pile and continue flowing, the highest velocity values are observed. In the downstream direction, a vortex forms, and the lowest flow velocity is observed here.

Figure 10. Displacement values U(m) on consecutive piles with different spacing D.

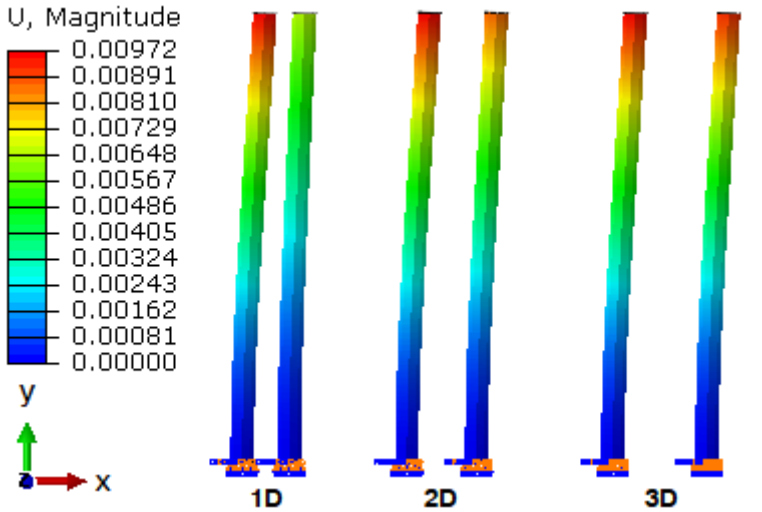
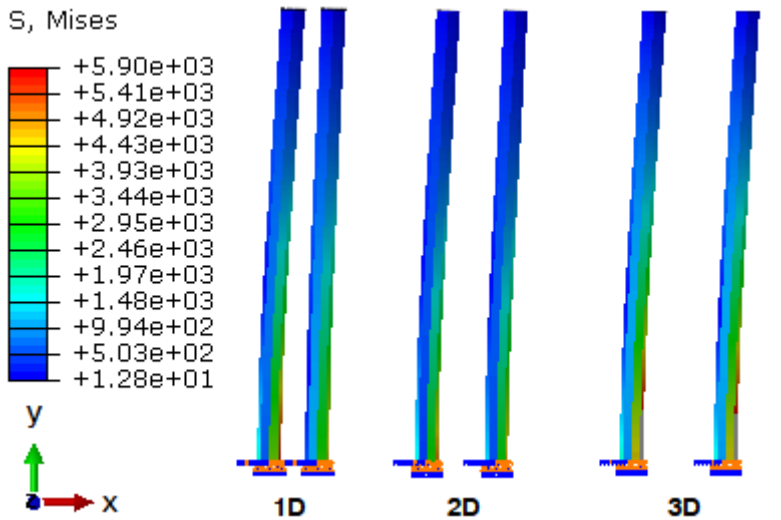


Figure 11. Mises stress values S(kN/m^2) on successive piles with different spacing D.



As a result of the hydrodynamic forces acting on the structure, a displacement of 0.00972 m at the apex and a Mises stress of 5904.11 kN/m² at the base of the steel pile with a wall thickness of t=14 mm was calculated (Figure 10). The variation of these values over time is given in Figures 11–14. The analysis results show that hydrodynamic loads change the stresses and deformations along the pile over time. According to the accepted wave parameters, it was observed that in arrangements where the distance between piles is 1D and 2D, the flow field of neighboring piles and the hydrodynamic load distribution are affected, thus a significant inter-pile interaction occurs. It was determined that this interaction decreased significantly and became negligible by increasing the distance between piles to 3D and above. This result shows that with increasing the pile spacing, the behavior of the piles under hydrodynamic loads becomes more independent of each other.

Figure 12. a) Displacement-time graph, b) Stress-time graph formed on successively spaced 1D piles.

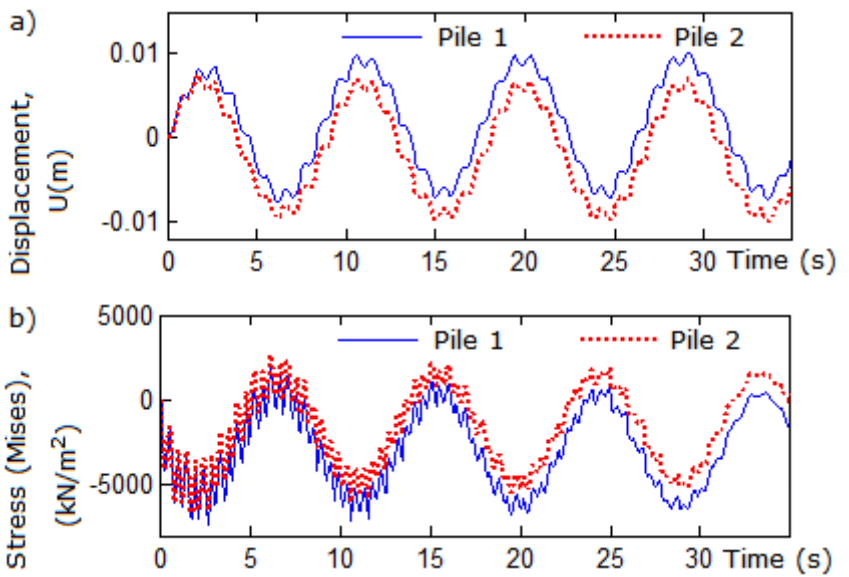


Figure 13. a) Displacement-time graph, b) Stress-time graph formed on successively spaced 2D piles.

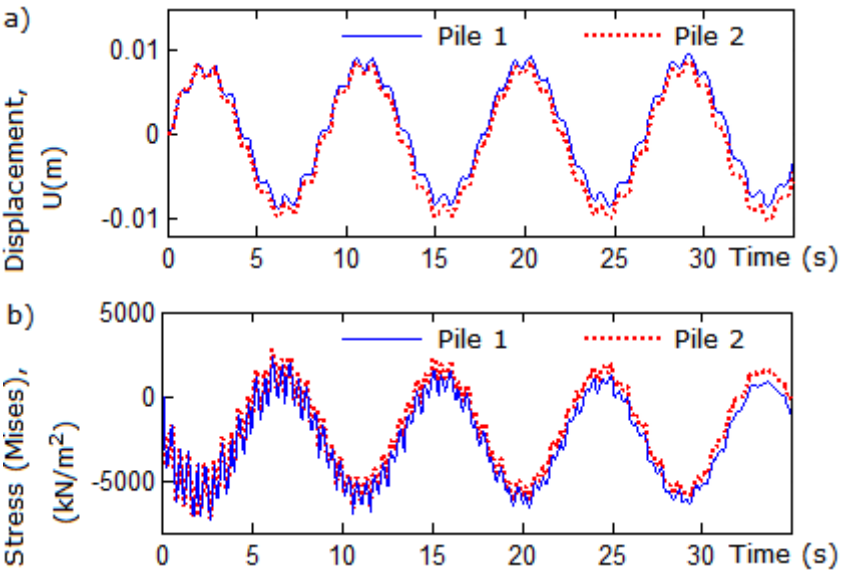
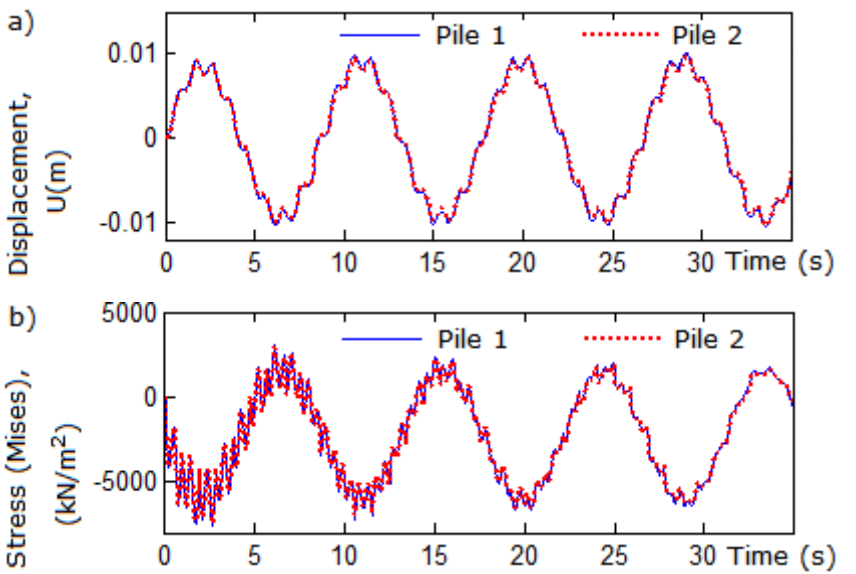


Figure 14. a) Displacement-time graph, b) Stress-time graph formed on successively spaced 3D piles.



Conclusion

In conclusion, this study analyses the external effects that sequential quay piles under linear wave influence may encounter throughout their service life, according to the determined parameters. Calculations revealed that the behavior of the system consisting of sequential piles under hydrodynamic loads is significantly dependent on the distance between the piles. Contour diagrams showing the velocity and pressure distributions around the piles revealed that neighboring piles significantly affect the flow field and hydrodynamic load distribution, especially in 1D and 2D pile spacing. Displacement and Mises stress distributions in the pile cross-sections, as well as stress-time variations at the pile tip and base, also demonstrate the reflections of this interaction on the structural behavior. Under the examined wave conditions, it was observed that increasing the distance between piles to 3D and above significantly reduced the hydrodynamic interaction and made the behavior of the piles more independent of each other.

However, it should be emphasized that these findings are limited to the wave height, period, water depth, and other hydrodynamic parameters considered in this study and should not be generalized to different wave conditions. This study presents a methodological approach for numerically investigating pile-to-pile hydrodynamic interaction under specific wave conditions through velocity, pressure, displacement, and stress distributions. Similar analyses using different wave conditions, particularly Stokes' 2nd and 3rd order wave theories and other wave theories, would provide a more comprehensive understanding of the relationship between pile spacing and hydrodynamic interaction. Therefore, the results should be considered not as a general design criterion, but as a guiding framework for numerical analyses of similar problems.

References

Abaqus. (2014, 01 12). *Analysis User's Manual, V6.6*. Abaqus documentation: http://62.108.178.35:2080/v6.14/books/usb/default.htm adresinden alındı

Altıok, T. Y. (2019). *Tarihi minarelerin dinamik özelliklerinin deneysel ve nümerik yöntemler ile araştırılması.* Manisa: Master's dissertation, Manisa Celal Bayar University.

Altiok, T., Cetin, K., & Demir, A. (2025). Effect of shear wall opening and reinforcement around opening on the structural strengthening. *Bull Earthquake Eng*, 3421-3449.

Amoudry, L., & Souza, A. (2011). eterministic Coastal Morphological and Sediment Transport Modeling: A Review and Discussion. *Reviews of Geophysics, 49*, 1-21.

Chakrabarti, S. (1987). *Hydrodynamics of Offshore Structures.* Berlin: Springer-Verlag.

Clough, R. W., & Penzien, J. (1993). *Dynamics of Structures (2nd edition).* Singapore: : Mc Graw–Hill, Inc, .

Fredsoe, J., & Deigaard, R. (1992). *Mechanics of Coastal Sediment Transport, vo- lume 3 of Advanced Series on Ocean Engineering.* New Jersey: World Scientific.

Gökkuş, Ü., Yiğit, M. E., & Gücüyen, E. (2017). Flexible Body Dynamics of Offshore Wind Turbine Under Extreme Loading Conditions. *International Journal of Sciences & Applied Research, 4*(2), 22-29.

Karaturp, F. (2007). Kıyı Hidrodinamiğine İlişkin Dalga Denklemlerinin Çözümlenmesinde Kısmi Diferansiyel Denklem Uygulamaları. *Yüksek Lisans Tezi*. Manisa.

Kırca, V. (2013). *Dalga Kırılma Bölgesi Dışında Katı Madde Hareketi, İstanbul Teknik Üniversitesi.* İstanbul: İstanbul Teknik Üniversitesi Ders Notu.

Le-Mehaute, B. (1969). *An Introduction to Hydrodynamics and Water Waves.* Berlin: Springer.

Luque, R., & Beek, R. (1976). Erosion and transport of bed load sediment. *Journal of Hydraulic Research, 14*(2), 127-144.

Morison, J. O. (1950). The Forces Exerted by Surface Waves on Piles. *Petroleum Trans, 189*, 149-157.

Nielsen, P. (1992). *Coastal Bottom Boundary Layers and Sediment Transport.* World Scientific: World Scientific.

Ölmez, İ. H., Yiğit, M. E., & Solmaz, B. (2011). Düzenli Dalgalar Etkisindeki Deniz Tabanına Serbest Oturan Boruhatlarının Dinamik Analizi. *5nci Ulusal Su Mühendisliği Sempozyumu* (s. 95-105). İstanbul: DSİ.

Russell, J. (1844). *Report on Wave. Report of the 14th Meeting of the British Association for the Advancement of Science.* York.

Soulsby, R. &. (2005). Bedload Sediment Transport in Coastal Waters. *Coastal Engineering, 52*, 673-689.

Soulsby, R. (1997). *Dynamics of Marine Sands.* London: Thomas Telford Pub.,.

Stokes, G. (1980). *On the Theory of Oscillatory Waves.* Cambridge: Cambridge University Press.

Tsuchiya, Y., & Yasuda, T. (1980). A New Approach to Stokes Wave Theory. *Bulletin of the Disaster Prevention Research Institute, 31*(1), 17-34.

Von-Mises, R. (1913). Nachrichten von der Gesellschaft der Wissenschaften zu Göttingen. *Mathematisch-Physikalische Klasse, 1913*, 582-592.

Wilson, K., & Nnadi, F. (1990). Behaviour of mobile beds at high shear stress, In Behaviour of mobile beds at high shear stress. *In Proceedings of 22th ICCE, 3*, 25-36.

Yiğit, M. E. (2019). Dalga, Sediment ve Sıvılaşan Zemin İtkilerine Maruz Rıhtım Kazıklarının Dinamik Davranışlarının Modellenmesi. *Doktora Tezi*. Manisa: Manisa Celal bayar Üniversitesi, Fen Bilimleri Enstitüsü.

Yiğit, M. E., & Gökkuş, Ü. (2025). Dynamic Analysis of Dock Piles under the Effects of Different Sea Waves and Sediment Movement. A. KUMBASAROĞLU içinde, *İNŞAATTA DİJİTALLEŞME VE MODERN* (s. 52-80). Ankara: Bidge Yayınları.

Yiğit, M. E., & Gökkuş, Ü. (2026). Investigation of Consecutive Quay Piles Under the Effect of Submarine Landslide. *Journal of Naval Sciences and Engineering*, 217-241.

BÖLÜM 3

FLEXURAL BEHAVIOR OF RAPIDLY COOLED CJP GROOVE WELDS ON ULTRA HIGH STRENGTH STEEL

EMİR ALTIPARMAK [1] & ERAY ÖZBEK[2]

Introduction

Background of the Study

Ultra-High-strength cold-drawn steels are widely utilized in modern structural engineering due to their superior strength-to-weight ratio and performance under dynamic effects. Within this scope, ultra-high-strength steel (UHSS) may become a critical material, particularly in high-rise steel frames, bridges, and moment-resisting connections, as it optimizes the load-bearing capacity while reducing structural self-weight. To ensure continuous stress transfer in structural steel assemblies, Complete Joint Penetration (CJP) groove welding is the most prevalent joining technique due to its mechanical stability and reliability.

[1] Gazi University Eng. Faculty, Civil Engineering Dept., Orcid: 0009-0008-4346-7969
[2] Assoc. Prof. Dr., Gazi University Eng. Faculty, Civil Engineering Dept., Orcid: 0000-0001-6738-7789

Aim and Scope

According to the Turkish Steel Building Design Code (ÇYHY 2018), the design strength of the weld metal in CJP groove welds must be equal to or greater than the nominal strength of the connected base metal to ensure full strength continuity. Thus, neither does failure occur at the weld cross-section, nor is there any need for design calculations. However, for UHSS elements manufactured through cold-drawing processes, locating a commercially compatible matching electrode metal that satisfies this Code requirement is highly challenging, inevitably leading to an undermatching joint connection where the weld zone acts as the weak link.

This research proposes and evaluates an experimental methodology aimed at mitigating this undermatching deficit. The primary objective of this study is to converge strength and mechanical behavior of the weld metal closer to the UHSS base metal by utilizing accelerated post-weld thermal histories (immediate water quenching). To systematically quantify the efficiency of this technique, an experimental program involving three-point bending tests was conducted. A total of three test specimens possessing the properties specified below were tested.

- Specimen 1 (Reference): A seamless, monolithic 200 mm long reference UHSS plate without any welding application.
- Specimen 2 (Air-Cooled): Two 100 mm long plates were connected by CJP groove welds and allowed to cool naturally at ambient room temperature. For the welding process, the two pieces were placed with a 1 mm gap between them and connected by Gas Metal Arc Welding (GMAW).

- Specimen 3 (Water-Cooled): Two 100 mm long plates were connected by CJP groove welds as in Specimen 2, but, immediately afterwards, submerged into a water bucket for 10 seconds for accelerated cooling.

These 200 mm long specimens were subjected to standard three point bending tests with a net span length of 150 mm. The applied force versus mid-span deflection data was recorded and analyzed in terms of strength, ductility, stiffness, and energy dissipation. Subsequently, the results were evaluated by comparing specimens among each other.

LITERATURE REVIEW

Structural Significance of Cold-Drawn Steel and CJP Groove Welds

UHSS elements have gained a significant role in modern structural applications due to their exceptional yield strength thresholds, which frequently approach or exceed 900 MPa. This type of steel is primarily engineered through cold-drawing fabrication processes, which induce severe strain hardening and dislocation accumulation within the crystalline lattice. To maintain full strength continuity across these high-demand components, CJP groove welding is strictly mandated by modern design codes (AWS, 2020). However, connecting strain hardened steel matrices presents a profound metallurgical challenge. Commercially available welding consumables generally possess nominal strengths designed for standard hot-rolled structural steel grades, inevitably establishing an "undermatching" joint configuration where the welded section exhibits lower mechanical properties than the adjacent base metal (Wang et al., 2020). In performance-based seismic design, understanding the flexural behavior of these undermatching full-penetration joints is vital, as the weld line acts as a localized

structural weak link under severe plastic hinge rotation demands (Bruneau et al., 2011).

Microstructural Evolution and Cooling Rate Effects

The final mechanical attributes of CJP groove welds are fundamentally controlled by the post weld thermal dissipation rate, which governs the kinetics of microstructural phase transformations within the molten weld pool (Lancaster, 1999). Under standard ambient air cooling conditions, the slow thermal cycle allows for equilibrium diffusion, resulting in coarser, softer microstructural phases such as proeutectoid ferrite and pearlite, which exacerbate the strength deficit of the undermatching weld (Bayram et al., 1999). Conversely, when the welded part is subjected to accelerated cooling via immediate water quenching, the rapid thermal extraction bypasses equilibrium transformation pathways. This rapid cooling forces a diffusionless solid-state transformation, traps carbon atoms within the iron lattice, and converts the face-centered cubic (FCC) austenite directly into a highly strained body centered tetragonal (BCT) acicular martensite matrix (Shi & Han, 2008). This martensitic transformation induces profound localized microstructural hardening, which can be strategically leveraged to elevate the mechanical properties of an undermatching weld zone.

Solidification Kinetics, Dislocation Locking, and Brittle Fracture

The scientific mechanism driving the macroscopic strength enhancement in rapidly cooled weldments lies within the principles of dislocation dynamics and lattice strain (Withers & Bhadeshia, 2001). The forced formation of acicular martensite creates an extremely high density of internal crystal boundaries and micro-twins. These structural boundaries act as severe pinning sites that effectively lock and restrict the mobility of dislocations under external mechanical loading. Because dislocation movement is the

primary mechanism of plastic deformation, locking these slip planes artificially elevates the stress threshold required to initiate yielding, thereby maximizing the peak load-bearing capacity of the joint. However, this microstructural immobilization introduces a severe drawback. The lack of dislocation mobility eliminates the material's capacity for plastic stress redistribution, while simultaneously trapping severe, multi-axial tensile residual stress fields (Withers & Bhadeshia, 2001). When superimposed with external flexural demands, these localized constraints inhibit micro-void coalescence and trigger instantaneous, catastrophic brittle cleavage fracture along the connection centerline (Shi & Han, 2008).

EXPERIMENTAL PROGRAM

Material Properties and Specimen Geometry

UHSS plates were utilized as the base metal in the experimental program. Expected yield strength of this plate material was 900 MPa and this value was verified in the reference specimen test. All specimens maintained a nominal cross-sectional profile of 50 mm in width and 5 mm in thickness. To ensure geometric standardization across the laboratory tests, the final length of the evaluated elements was established as 200 mm. The reference specimen was cut directly to these dimensions, whereas the welded specimens were fabricated by aligning two separate 100 mm long segments. Weld electrode (metal) grade was E550 which corresponds to a 470 MPa characteristic yield stress and 550 MPa ultimate stress. That grade is the maximum commercially available one if rare ones are excluded.

Welding Procedure and Post-Weld Thermal Conditions

GMAW process was utilized to assemble the welded specimens. Two 100 mm plate segments were secured in a welding fixture, maintaining a precise 1 mm root opening. The welding

process was executed in a single pass under constant current and voltage to achieve a complete CJP groove weld.

- Air-Cooling Protocol: The first welded set was left inside the laboratory environment (20°C ± 2) to cool naturally via ambient air convection without any external intervention.
- Water-Cooling Protocol: The second welded set was submerged into a water-filled container immediately (within 1-2 seconds) after the extinction of the welding arc. The specimen was held inside the water for exactly 10 seconds to induce an abrupt thermal shock, and the accelerated cooling process was completed upon removal.

Three-Point Bending Test Setup

To measure the flexural performance of the three specimens, a standard three-point bending test assembly was calibrated in the laboratory (Image 1). The technical parameters of the testing mechanism were governed by the following constraints:

- Support Span: The net distance between the two lower roller supports (span length) was fixed at exactly 150 mm. The specimens were placed symmetrically on the supports, leaving a 25 mm overhang at each boundary (Image 1).
- Loading Point: The upper loading plate was positioned at the mid-span (L = 100 mm), aligning directly with the critical 1 mm weld line of the welded specimens.
- Machine Configurations: The hydraulic actuator and data acquisition unit were calibrated for a 30 mm vertical displacement limit. During testing, the mid-span vertical

load (P, kN) and corresponding deflection (Δ in mm) were continuously recorded at a high acquisition frequency.

Image 1: Experimental Setup



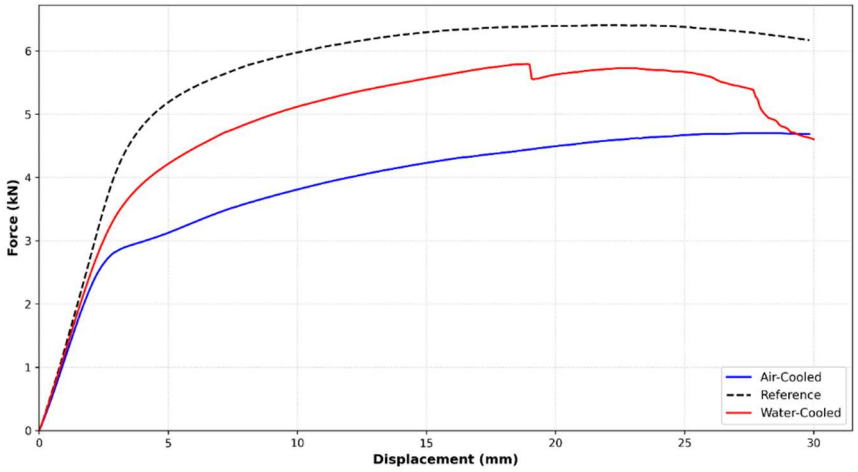
Source: Captured by the author during experimental testing

RESULTS AND DISCUSSION

Analysis of Load-Displacement Curves

The raw data extracted from the three-point bending tests were used to plot Force-Displacement curves to evaluate individual and comparative structural responses (Figure 1). The numerical outputs reveal distinct mechanical behaviors among the configurations. Those experimental load-displacement profiles (Figure 1) clearly illustrate the structural consequences of welding an ultra-high-strength cold-drawn steel matrix with standard consumables. Because the base metal possesses an exceptionally high yield strength due to its cold-drawn fabrication history, the standard weld deposit acts as an undermatching joint zone. The air-cooled specimen exhibited the lowest peak flexural capacity of 4.70 kN. This marked capacity degradation stems from the unmitigated undermatching state of the filler metal combined with localized thermal grain enlargement within the heat affected zone, which creates a soft zone susceptible to early plastic deformation (Bayram et al., 1999).

Figure 1: Comparison of Flexural Behavior (CJP Groove Welds)



Source: Plotted by the author from experimental measurements

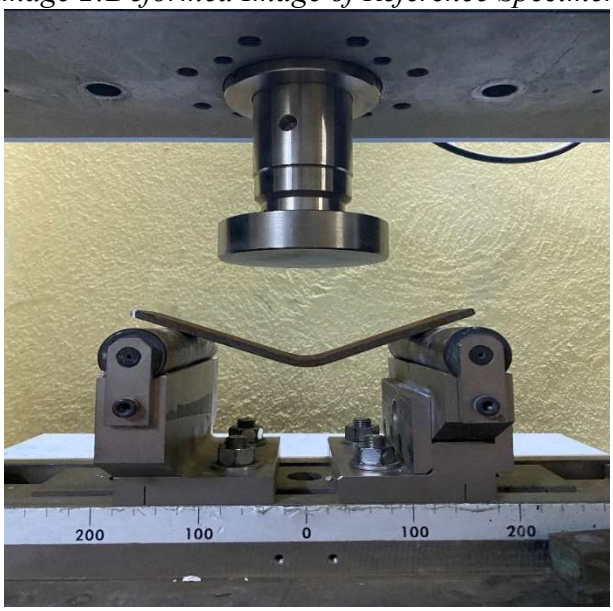
- Reference Specimen Response (Figure 1): The unwelded monolithic cold drawn steel plate exhibited a linear elastic region followed by a stable, well-distributed plasticization, reaching a peak flexural capacity of 6.41 kN (Image 2). This ultimate load was achieved at a vertical displacement of 22.3 mm. Due to the absence of geometric discontinuities or thermal alterations, this reference specimen provided the highest load-bearing capacity. Yield point can be accepted as 5kN and this value corresponds to a 900 MPa tensile stress if linear elastic calculation is considered.
- Air-Cooled Specimen Response (Figure 1): Following the GMAW process, the specimen allowed to cool naturally in the air demonstrated a reduced peak load capacity of 4.70 kN. This degradation is attributed to the lower weld metal capacity and high heat input of the welding process, which induces localized thermal softening in the base metal matrix. Yielding occurred at 2.8 kN and this value corresponds to a 504 MPa tensile stress if linear elastic calculation considered. It should be noted that weld metal had 470 MPa characteristic tensile yield strength which is very close to the experimental value. This specimen attained its peak load at a high displacement of 28.1 mm, exhibiting significant ductility and plastic deformation capacity (Image 4).
- Water-Cooled Specimen Response (Figure 1): The rapidly cooled welded specimen revealed a striking mechanical transformation. Due to the microstructural hardening induced by the immediate water quenching, the peak flexural capacity escalated to 5.80 kN, significantly outperforming the air-cooled specimen (4.70 kN).

Failure Mechanisms and Behavior Evaluation

The water-quenched specimen successfully demonstrated the intended strength approximation behavior and almost (90%) reached the reference value of 6.41 kN. If a higher-grade electrode or a slightly lower-strength UHSS had been used, a perfect match could have been achieved. Water quenching increases the strength capacity by 23% (Table 1). This clear capacity increase is scientifically justified by the forced kinetics of rapid thermal dissipation. The rapid water shock suppresses diffusion-controlled phase transformations, triggering a diffusionless transformation that generates a highly hardened, acicular martensitic microstructure within the undermatching weld core (Shi & Han, 2008). On a microscopic scale, the dense, interlocking needle-like structure of acicular martensite severely restricts and locks dislocation movement along the active slip planes of the crystal lattice. By immobilizing these dislocations, the material requires a significantly higher external stress to undergo slip, which manifests macroscopically as a substantial increase in flexural load capacity and joint rigidity (recovering to 1.35 kN/mm as seen in Table 1).

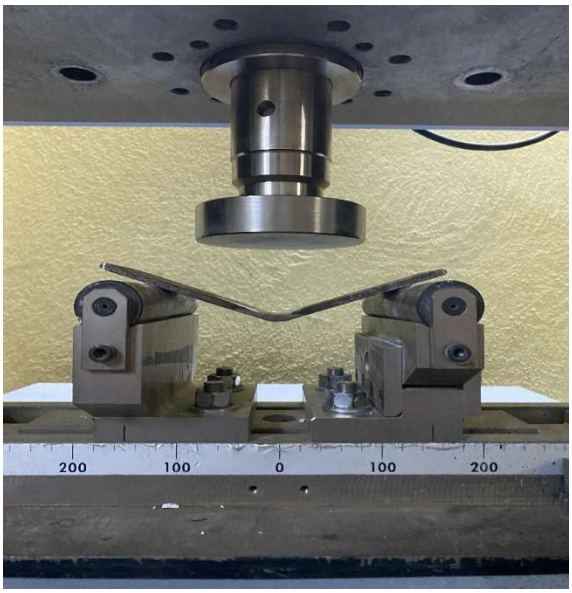
However, this localized hardening decreased the ductility as expected. Nevertheless, ductility ratio of 7.8 was achieved which cannot be considered brittle failure (Table 1 and Image 4).

Image 2:Deformed Image of Reference Specimen



Source: Captured by the author during experimental testing

Image 3:Deformed Image of Air-Cooled Specimen



Source: Captured by the author during experimental testing

Image 4:Deformed Image of Water-Cooled Specimen



Source: Captured by the author during experimental testing

Quantitative Performance Metrics and Comparative Analysis

The raw datasets extracted from the three-point bending tests were systematically evaluated in terms of strength, ductility, stiffness, and energy dissipation (Table 1). The point where the curve begins to level off was taken as the yield strength (P_y). Ultimate load was the peak point strength (P_{max}). The ductility index was the ratio of ultimate deformation without significant (15%) strength loss to the yield deformation ($\mu = \Delta u / \Delta y$). The initial elastic stiffness values, evaluated via the linear elastic slopes of the load-displacement profiles. Finally dissipated energy (E) values were obtained by calculating the area under the load-displacement curves.

Table 1. Quantitative Flexural Performance of Specimens

Specimen Type	Py (kN)	Δy (mm)	σy (MPa)	Pmax (kN)	Ductility (μ)	Stiffness (kN/mm)	E (joule)
Reference	5.05	3.90	982.8	6.41	≥ 7.7	1.45	≥169.2
Air-Cooled	2.82	2.42	507.6	4.70	≥ 7.8	1.21	≥116.1
Water-Cooled	4.54	3.62	817.2	5.80	7.8	1.35	146.5

Source: Compiled by the author from three-point bending test results

The monolithic reference specimen developed the highest nominal flexural strength of 6.41 kN due to its undisturbed structural configuration. Following the application of the CJP groove welding procedure, a capacity degradation down to 4.70 kN was recorded for the air-cooled configuration, representing a net strength loss of 36.4%. This performance deficit is directly linked to the lower weld metal (electrode) capacity and high heat input of the welding process, which induces localized thermal softening in the base metal matrix. On the other hand, for the water-cooled configuration, the immediate post-weld water quenching effectively increased the strength up to 24%. Consequently, the peak flexural capacity escalated back to 5.80 kN, achieving a notable strength recovery.

The initial elastic stiffness values, evaluated via the linear elastic slopes of the load-displacement profiles, indicated a parallel structural trend (Table 1). The baseline rigidity of 1.45 kN/mm from the reference monolithic plate was reduced to 1.21 kN/mm in the air-cooled specimen due to the geometric and structural discontinuities introduced at the joint zone. For the water-cooled specimen, the highly constrained lattice paths partially restored the flexural stiffness to 1.35 kN/mm.

The reference specimen achieved a ductility ratio greater than 7.7. It might have reached higher ratios, but the experiment was not continued once this point was deemed sufficient for structural engineering purposes. As can be seen in Image 2-4, even achieved plastic deformations are much higher than serviceability limits. Air-cooled specimen showed similar behavior to reference specimen in terms of ductility and reached ductility ratios greater than 7.8 (Table 1). On the other hand, water-cooled specimen reached an exact ductility ratio of 7.8. At that ratio, specimen significantly lost its strength (at least 15%) (Figure 1). However, this kind of failure cannot be accepted as brittle (Image 4).

The reference specimen successfully dissipated energy greater than 169.2 J, driven by its extensive and stable plastic yield plateau. Owing to its lower load plateau, the air-cooled joint seemed to be limited to an energy capacity of 116.1 J (Figure 1). The water-cooled joint accumulated a significant energy envelope of 146.5 J due to its higher load pathway (Table 1).

CONCLUSIONS

The implications of post-weld cooling rates on the flexural behavior of CJP groove welded cold-drawn UHSS plates were successfully quantified through an experimental investigation. Based on the laboratory three-point bending tests and subsequent integrated numerical interpretations of load displacement profiles, critical mechanical alterations driven by post-weld thermal histories and microstructural kinetics were verified. The following structural conclusions are derived from this research.

Rapid post-weld water quenching successfully achieved the core engineering objective of narrowing the mechanical strength gap between the structurally undermatching weld metal and the UHSS cold-drawn base metal. Immediate water shock effectively recovered the flexural capacity from 4.70 kN up to 5.80 kN, almost approaching the Reference specimen of 6.41 kN at the rate of 90%. This type of significant recovery was also obtained for stiffness and energy dissipations by maintaining sufficient ductility.

It should be noted that the obtained data is based on a limited number of tests; therefore, absolute judgements should be avoided.

Bibliography

American Welding Society. (2020). *Structural Welding Code - Steel (AWS D1.1/D1.1M:2020).* Miami, FL: AWS.

Bayram, A., Uguz, A., & Ula, M. (1999). Effects of microstructure and notches on the mechanical properties of dual-phase steels. *Materials Characterization*, 259-269.

Bruneau, M., Uang, C.-M., & Sabelli, R. (2011). *Ductile Design of Steel Structures.* New York, NY: McGraw-Hill Professional.

Çevre, Şehircilik ve İklim Değişikliği Bakanlığı. (2018). *Çelik Yapıların Tasarım, Hesap ve Yapım Esaslarına Dair Yönetmelik (ÇYHY 2018).* Ankara: Resmi Gazete.

Lancaster, J. F. (1999). *Metallurgy of Welding.* Cambridge, UK: Woodhead Publishing.

Shi, Y. W., & Han, Z. X. (2008). Effect of weld thermal cycle on microstructure and impact toughness of HAZ in high strength low alloy steel. *Journal of Materials Processing Technology*, 30-39.

Wang, P., Pei, S., & Shi, G. (2020). Experimental study on undermatching welded connections of high-strength steel. *Journal of Constructional Steel Research*, 1-15.

Withers, P. J., & Bhadeshia, H. K. (2001). Residual stress. Part 2 - Nature and origins. *Materials Science and Technology*, 366-375.

BÖLÜM 4

GOOGLE EARTH ENGINE FOR WATER RESOURCES MONITORING: DATASETS, APPLICATIONS AND LIMITATIONS

YILDIRIM BAYAZIT[1]

Introduction

Water managers in semi-arid regions rarely suffer from a shortage of questions. What they lack is consistent observation. Rain gauges are sparse and records have gaps. Satellite remote sensing has filled part of this gap for decades, but until recently the practical cost of using it was high. Tracing the shoreline of a single lake over thirty years meant downloading and correcting hundreds of Landsat scenes before the first hydrological question could be asked.

Google Earth Engine (GEE) changed this workflow by moving the analysis to the data instead of moving the data to the analyst (Gorelick et al., 2017). The platform joins a multi-petabyte catalogue of satellite imagery and gridded geophysical products with a parallel processing system that users reach through JavaScript or Python. Since its public release, the number of studies built on it has grown quickly in land cover mapping, agriculture, forestry and

[1] Doçent Dr., Bilecik Şeyh Edebali University, Faculty of Engineering, Department of Civil Engineering, ORCID: 0000-0002-8699-4741

hydrology (Amani et al., 2020; Kumar & Mutanga, 2018; Tamiminia et al., 2020), and bibliometric analyses place water-related topics among its most frequent applications (Velastegui-Montoya et al., 2023; Zhao et al., 2021).

Interest is particularly strong where water stress is rising. The Mediterranean basin is warming faster than the global average and is projected to face longer and more frequent droughts (Cramer et al., 2018). Türkiye lies on the eastern edge of this region, and its closed basins, shrinking lakes and heavily pumped aquifers make it a useful setting for testing what cloud-based Earth observation can and cannot deliver. This chapter looks at GEE from the point of view of a water resources researcher. It explains how the platform works, reviews its main hydrological applications with examples from Türkiye, and closes with its limitations and likely future developments.

How Google Earth Engine Works

GEE rests on three components: a public data catalogue, a computation service running on Google's infrastructure, and client libraries in which users write their scripts (Gorelick et al., 2017). The user never downloads the images. A script simply describes what should happen, for example filtering a collection by date and area, masking clouds, computing an index and summarising the result over a region. These instructions are sent to the server, executed in parallel on many machines and returned as a map layer, a chart, a table or an exported file. The same script can therefore be run for a small catchment or for a whole country with very few changes.

Two features are especially useful in hydrology. The first is the image collection, in which every scene of a satellite archive is stored as a georeferenced image with its metadata. A time series analysis then becomes a matter of applying a function to every image and reducing the collection, for instance by taking the median of all

cloud-free observations in a month. The second is the family of reducers that summarise pixel values within polygons, so that a basin boundary can be used directly to extract area-averaged rainfall, evapotranspiration or water extent. The geemap package (Wu, 2020) brings these tools into Python notebooks.

GEE is not the only platform built on this idea. Microsoft Planetary Computer, services based on the openEO interface and the Copernicus Data Space Ecosystem offer similar functions with different data holdings and licensing terms (Gomes et al., 2020). GEE is still the most widely used in published research, mainly because of its early start, the breadth of its catalogue and the large amount of openly shared code (Tamiminia et al., 2020; Velastegui-Montoya et al., 2023).

Datasets for Water Resources in the Earth Engine Catalogue

For hydrology, the strength of GEE lies less in its algorithms than in the data stored next to them. Table 1 lists the products that appear most often in water studies. Optical archives such as Landsat and Sentinel-2 provide the spatial detail needed for lakes, reservoirs and irrigated fields (Wulder et al., 2016). Sentinel-1 radar complements them when clouds or darkness block optical sensors, which matters most during floods. Derived products take away much of the preprocessing work. The JRC Global Surface Water dataset, for example, records the presence of water every month from 1984 onward at 30 m resolution (Pekel et al., 2016).

Climate and water balance variables are just as easy to reach. CHIRPS, PERSIANN-CDR and IMERG supply satellite-based precipitation with different resolutions and record lengths (Ashouri et al., 2015; Funk et al., 2015). ERA5-Land and TerraClimate provide temperature, evaporation, soil moisture and runoff within a consistent modelling framework (Abatzoglou et al., 2018; Muñoz-Sabater et al., 2021). MODIS evapotranspiration, GRACE terrestrial

water storage anomalies and global hydrography layers such as HydroSHEDS complete the set (Mu et al., 2011; Tapley et al., 2004). None of these products is free of error, yet having all of them in one place, under the same access rules, makes it far easier to compare and combine them.

Table 1. Selected Earth Engine Datasets Commonly Used in Water Resources Studies

Dataset	**Variable**	**Spatial resolution**	**Period**	**Typical use**
Landsat 5, 7, 8 and 9	Surface reflectance, thermal bands	30 m	1984 to present	Lake and reservoir extent, land use
Sentinel-2 MSI	Surface reflectance	10 to 20 m	2015 to present	Small water bodies, irrigated fields
Sentinel-1 SAR	C-band radar backscatter	10 m	2014 to present	Flood mapping under cloud
JRC Global Surface Water	Water occurrence and change	30 m	1984 onward	Long-term surface water change
CHIRPS	Precipitation	0.05° (about 5.5 km)	1981 to present	Rainfall trends, SPI and SPEI
PERSIANN-CDR	Precipitation	0.25° (about 27 km)	1983 to present	Long precipitation records
GPM IMERG	Precipitation	0.1° (about 11 km)	2000 to present	Sub-daily rainfall, floods
ERA5-Land	Temperature, evaporation, soil moisture, runoff	0.1° (about 9 km)	1950 to present	Water balance, SPEI
TerraClimate	Climatic water balance	about 4 km	1958 to present	Long-term drought analysis

Dataset	Variable	Spatial resolution	Period	Typical use
MOD16A2	Actual ET	500 m	2001 to present	Basin and crop water use
GRACE and GRACE-FO	Terrestrial water storage anomaly	About 300 km (native)	2002 to present, gap in 2017 to 2018	Groundwater storage change
HydroSHEDS	Basins and river networks	90 m to 500 m	Static	Catchment delineation

Source: Compiled by the author from the Earth Engine Data Catalog and the dataset descriptions cited in the text.

Surface Water, Lakes and Reservoirs

Mapping open water is the most mature hydrological use of GEE. Water absorbs strongly in the near-infrared and shortwave infrared parts of the spectrum, so simple band ratios separate it from land with reasonable accuracy. The Normalized Difference Water Index uses the green and near-infrared bands (McFeeters, 1996), while its modified version replaces near-infrared with shortwave infrared to reduce false signals from built-up areas (Xu, 2006). In GEE these indices can be computed for every available scene, thresholded and aggregated into monthly or annual water masks without leaving the browser.

Global studies show what this makes possible. Pekel et al. (2016) processed more than three million Landsat scenes to show where permanent water disappeared and where new water appeared between 1984 and 2015, and found that most of the net loss was concentrated in the Middle East and Central Asia. More recently, Donchyts et al. (2022) reconstructed surface area changes for more than 71,000 small and medium-sized reservoirs and showed that small reservoirs vary much more from year to year than larger ones, which leaves the communities depending on them more exposed to drought. Combining satellite altimetry with optical records, Yao et

al. (2023) found that more than half of the world's large lakes lost water storage between 1992 and 2020.

Türkiye provides several clear examples. Lake Burdur, a saline closed-basin lake in the Lakes Region, has been shrinking for decades. Using 570 Landsat images processed in GEE, Abujayyab et al. (2021) showed that its surface area fell from about 207 km² to about 126 km² between 1984 and 2019, and related the decline to temperature, evaporation, precipitation and vegetation cover. Albarqouni et al. (2022) compared Burdur with Lakes Eğirdir and Beyşehir and found that Burdur lost more than a fifth of its water surface between 2000 and 2021 while the other two changed little. They concluded that human pressures, rather than climate alone, explain the contrast. At the national scale, Dervisoglu (2021) used GEE to follow the inland Ramsar sites of the country from 1985 to 2020 and reported that their spring-season wetland area shrank by about 31% over that period. These studies share a practical lesson. The remote sensing step is no longer the bottleneck. The harder question is attribution, that is, separating the effects of climate, irrigation withdrawals and reservoir operation.

Precipitation, Climate and Drought

Precipitation is the main input of almost every hydrological analysis, and ground networks rarely capture its variability in mountainous terrain. Satellite and blended products help fill this gap, although their accuracy depends on region, season and rainfall intensity (Sun et al., 2018). For Türkiye, Aksu and Akgül (2020) evaluated CHIRPS against station observations and found that its agreement with the gauges is considerably better at monthly than at daily time steps. Evaluations of this kind are a necessary first step before any product is used to compute drought indices or to drive a hydrological model.

Drought indices follow naturally from these inputs. The Standardized Precipitation Index (SPI) expresses the precipitation total over a chosen accumulation period as a standardised anomaly of a fitted probability distribution (McKee et al., 1993). The Standardized Precipitation Evapotranspiration Index (SPEI) applies the same idea to the climatic water balance, so that rising temperature and evaporative demand also enter the calculation (Vicente-Serrano et al., 2010). Both indices can be built in GEE with CHIRPS for precipitation and ERA5-Land or TerraClimate for potential evapotranspiration (Abatzoglou et al., 2018; Muñoz-Sabater et al., 2021), although fitting distributions pixel by pixel is often easier after exporting monthly series to Python. In semi-arid basins SPEI is usually the more informative of the two, because a warm year with near-average rainfall can still end with a clear water deficit.

Evapotranspiration and Agricultural Water Use

In irrigated basins, evapotranspiration (ET) is the largest consumptive use of water and the term of the water balance that is hardest to measure. Satellite ET models estimate it either from the surface energy balance or from vegetation and meteorological inputs. The MOD16 product, which is based on the Penman-Monteith equation, is available in GEE at 500 m resolution and eight-day intervals (Mu et al., 2011). Energy balance approaches such as SSEBop use land surface temperature to scale reference ET and can be run on Landsat imagery to obtain field-scale estimates (Senay et al., 2013). Several such models have been rewritten to run inside GEE, which allows ET to be mapped for entire irrigation districts over several decades.

In Türkiye, where agriculture accounts for the large majority of water withdrawals, field-scale ET maps could support allocation decisions in basins such as Konya, Gediz and the lower Seyhan. The

main obstacle is validation. Eddy covariance stations are scarce in the country, so most estimates can only be checked indirectly. ET maps should therefore be read as estimates whose uncertainty can be substantial at the field scale, and at least two independent products should be compared before firm conclusions are drawn.

Groundwater and Terrestrial Water Storage

The GRACE mission, launched in 2002, and its successor GRACE Follow-On, launched in 2018, measure monthly changes in the Earth's gravity field. Over land, most of these changes reflect water moving into or out of storage (Tapley et al., 2004). Gridded GRACE solutions in GEE provide terrestrial water storage anomalies that combine snow, surface water, soil moisture and groundwater. When soil moisture and surface storage simulated by land surface models are subtracted, what remains is an estimate of groundwater change. Rodell et al. (2018) applied this reasoning at the global scale and identified several hotspots of declining freshwater storage, among them parts of the Middle East where groundwater pumping and drought act together.

The Konya Closed Basin is the best documented case in Türkiye. Koycegiz et al. (2023) analysed GRACE-based storage anomalies together with model outputs and well records and found marked declines in both terrestrial water storage and groundwater levels. They also reported that groundwater in this karstic basin responds to precipitation with a delay of roughly six months. The coarse native resolution of GRACE, a few hundred kilometres, means that results apply to large basins rather than to individual aquifers or irrigation districts.

Floods

Flood mapping is where radar is most valuable. Sentinel-1 sees through clouds, and calm floodwater appears dark in its images because the smooth surface reflects the signal away from the sensor.

DeVries et al. (2020) developed a change detection method in GEE that compares backscatter during a flood with a historical baseline, and combined Sentinel-1 with Landsat to produce flood maps quickly after an event. At the global scale, Tellman et al. (2021) mapped 913 large flood events between 2000 and 2018 from MODIS imagery in GEE and found that the population living in flooded areas grew faster than the population as a whole. In Türkiye, where flash floods regularly cause damage along the Black Sea and Mediterranean coasts, these tools offer a fast way to document flood extent after an event. Narrow valleys and radar shadow in steep terrain, however, remain difficult to handle.

Limitations and Practical Considerations

Easy access to data does not remove the need for hydrological judgement. Several limitations appear again and again in the literature and in day-to-day work (Amani et al., 2020; Tamiminia et al., 2020; Yang et al., 2022):

- Validation still depends on ground data. Satellite products can show plausible spatial patterns while being biased in magnitude, and without gauges, wells or field observations the size of that bias stays unknown.
- Resolution often does not match the question. A 25 km precipitation product cannot represent rainfall in a narrow valley, and an eight-day ET product misses short irrigation cycles.
- Cloud cover, terrain shadow, ice and mixed pixels along shorelines affect optical water mapping, so small reservoirs and rivers only a few pixels wide are especially vulnerable.

- Computation is free for research but not unlimited. Very large or deeply nested operations may time out, and long exports need careful planning.
- Reliance on a commercial provider raises questions of continuity, licensing and data sovereignty, since users have little control over changes to the catalogue or the terms of use.
- Shared scripts are not automatically reproducible, because datasets are reprocessed and their versions change over time.

None of these points is an argument against the platform. They are arguments for recording dataset versions and processing dates, keeping a copy of every extracted time series, and treating satellite results as one line of evidence among several.

Future Directions

Three developments are likely to shape the coming years. The first is closer integration with machine learning. GEE already includes classifiers such as random forests and support vector machines, and its links to cloud-based deep learning services allow trained models to be applied over large areas (Yang et al., 2022). For water resources this could improve the mapping of small water bodies, irrigated crops and flood extent, provided that training data represent local conditions well.

The second is the arrival of new satellite missions. The Surface Water and Ocean Topography (SWOT) satellite, launched at the end of 2022, measures the water surface elevation of rivers and lakes. Combined with water area from optical imagery, such measurements may allow changes in lake and reservoir volume to be estimated more directly than before.

The third concerns how results reach decision makers. For Türkiye, a national system that follows lake and reservoir extent, drought indices and basin-scale ET in near real time is technically feasible with existing data. The harder problems are institutional: agreeing on validated methods, linking satellite outputs with ground networks run by different agencies, and keeping such systems running after the original project ends.

Conclusion

Google Earth Engine has lowered the cost of asking hydrological questions with satellite data. Tasks that once took weeks can now be completed in hours. Studies from Türkiye, from the shrinking lakes of the Lakes Region to the depleted aquifers of the Konya Closed Basin, show that these methods speak directly to the water problems of the country.

The main constraint today is interpretation rather than data access. Satellite products need ground validation, their resolution has to match the scale of the question, and their results must be read with an understanding of the processes behind them. Used with this care, GEE is a practical tool for researchers and water managers facing climate change and growing demand, especially in semi-arid regions where ground observations alone cannot keep up with the changes under way.

References

Abatzoglou, J. T., Dobrowski, S. Z., Parks, S. A., & Hegewisch, K. C. (2018). TerraClimate, a high-resolution global dataset of monthly climate and climatic water balance from 1958–2015. *Scientific Data, 5*, 170191. https://doi.org/10.1038/sdata.2017.191

Abujayyab, S. K. M., Almotairi, K. H., Alswaitti, M., Abu Amr, S. S., Alkarkhi, A. F. M., Taşoğlu, E., & Hussein, A. M. (2021). Effects of meteorological parameters on surface water loss in Burdur Lake, Turkey over 34 years Landsat Google Earth Engine time-series. *Land, 10*(12), 1301. https://doi.org/10.3390/land10121301

Aksu, H., & Akgül, M. A. (2020). Performance evaluation of CHIRPS satellite precipitation estimates over Turkey. *Theoretical and Applied Climatology, 142*(1–2), 71–84. https://doi.org/10.1007/s00704-020-03301-5

Albarqouni, M. M. Y., Yagmur, N., Balcik, F. B., & Sekertekin, A. (2022). Assessment of spatio-temporal changes in water surface extents and lake surface temperatures using Google Earth Engine for Lakes Region, Türkiye. *ISPRS International Journal of Geo-Information, 11*(7), 407. https://doi.org/10.3390/ijgi11070407

Amani, M., Ghorbanian, A., Ahmadi, S. A., Kakooei, M., Moghimi, A., Mirmazloumi, S. M., Moghaddam, S. H. A., Mahdavi, S., Ghahremanloo, M., Parsian, S., Wu, Q., & Brisco, B. (2020). Google Earth Engine cloud computing platform for remote sensing big data applications: A comprehensive review. *IEEE Journal of Selected Topics in Applied Earth Observations and Remote Sensing, 13*, 5326–5350. https://doi.org/10.1109/JSTARS.2020.3021052

Ashouri, H., Hsu, K.-L., Sorooshian, S., Braithwaite, D. K., Knapp, K. R., Cecil, L. D., Nelson, B. R., & Prat, O. P. (2015). PERSIANN-CDR: Daily precipitation climate data record from multisatellite observations for hydrological and climate studies. *Bulletin of the American Meteorological Society, 96*(1), 69–83. https://doi.org/10.1175/BAMS-D-13-00068.1

Cramer, W., Guiot, J., Fader, M., Garrabou, J., Gattuso, J.-P., Iglesias, A., Lange, M. A., Lionello, P., Llasat, M. C., Paz, S., Peñuelas, J., Snoussi, M., Toreti, A., Tsimplis, M. N., & Xoplaki, E. (2018). Climate change and interconnected risks to sustainable development in the Mediterranean. *Nature Climate Change, 8*(11), 972–980. https://doi.org/10.1038/s41558-018-0299-2

Dervisoglu, A. (2021). Analysis of the temporal changes of inland Ramsar sites in Turkey using Google Earth Engine. *ISPRS International Journal of Geo-Information, 10*(8), 521. https://doi.org/10.3390/ijgi10080521

DeVries, B., Huang, C., Armston, J., Huang, W., Jones, J. W., & Lang, M. W. (2020). Rapid and robust monitoring of flood events using Sentinel-1 and Landsat data on the Google Earth Engine. *Remote Sensing of Environment, 240*, 111664. https://doi.org/10.1016/j.rse.2020.111664

Donchyts, G., Winsemius, H., Baart, F., Dahm, R., Schellekens, J., Gorelick, N., Iceland, C., & Schmeier, S. (2022). High-resolution surface water dynamics in Earth's small and medium-sized reservoirs. *Scientific Reports, 12*, 13776. https://doi.org/10.1038/s41598-022-17074-6

Funk, C., Peterson, P., Landsfeld, M., Pedreros, D., Verdin, J., Shukla, S., Husak, G., Rowland, J., Harrison, L., Hoell, A., & Michaelsen, J. (2015). The climate hazards infrared precipitation with stations—a new environmental record for

monitoring extremes. *Scientific Data, 2*, 150066. https://doi.org/10.1038/sdata.2015.66

Gomes, V. C. F., Queiroz, G. R., & Ferreira, K. R. (2020). An overview of platforms for big earth observation data management and analysis. *Remote Sensing, 12*(8), 1253. https://doi.org/10.3390/rs12081253

Gorelick, N., Hancher, M., Dixon, M., Ilyushchenko, S., Thau, D., & Moore, R. (2017). Google Earth Engine: Planetary-scale geospatial analysis for everyone. *Remote Sensing of Environment, 202*, 18–27. https://doi.org/10.1016/j.rse.2017.06.031

Koycegiz, C., Sen, O. L., & Buyukyildiz, M. (2023). An analysis of terrestrial water storage changes of a karstic, endorheic basin in central Anatolia, Turkey. *Ecohydrology & Hydrobiology, 23*(4), 688–702. https://doi.org/10.1016/j.ecohyd.2023.07.002

Kumar, L., & Mutanga, O. (2018). Google Earth Engine applications since inception: Usage, trends, and potential. *Remote Sensing, 10*(10), 1509. https://doi.org/10.3390/rs10101509

McFeeters, S. K. (1996). The use of the Normalized Difference Water Index (NDWI) in the delineation of open water features. *International Journal of Remote Sensing, 17*(7), 1425–1432. https://doi.org/10.1080/01431169608948714

McKee, T. B., Doesken, N. J., & Kleist, J. (1993). The relationship of drought frequency and duration to time scales. In *Proceedings of the 8th Conference on Applied Climatology* (pp. 179–184). American Meteorological Society.

Mu, Q., Zhao, M., & Running, S. W. (2011). Improvements to a MODIS global terrestrial evapotranspiration algorithm.

Remote Sensing of Environment, 115(8), 1781–1800. https://doi.org/10.1016/j.rse.2011.02.019

Muñoz-Sabater, J., Dutra, E., Agustí-Panareda, A., Albergel, C., Arduini, G., Balsamo, G., Boussetta, S., Choulga, M., Harrigan, S., Hersbach, H., Martens, B., Miralles, D. G., Piles, M., Rodríguez-Fernández, N. J., Zsoter, E., Buontempo, C., & Thépaut, J.-N. (2021). ERA5-Land: A state-of-the-art global reanalysis dataset for land applications. *Earth System Science Data, 13*(9), 4349–4383. https://doi.org/10.5194/essd-13-4349-2021

Pekel, J.-F., Cottam, A., Gorelick, N., & Belward, A. S. (2016). High-resolution mapping of global surface water and its long-term changes. *Nature, 540*(7633), 418–422. https://doi.org/10.1038/nature20584

Rodell, M., Famiglietti, J. S., Wiese, D. N., Reager, J. T., Beaudoing, H. K., Landerer, F. W., & Lo, M.-H. (2018). Emerging trends in global freshwater availability. *Nature, 557*(7707), 651–659. https://doi.org/10.1038/s41586-018-0123-1

Senay, G. B., Bohms, S., Singh, R. K., Gowda, P. H., Velpuri, N. M., Alemu, H., & Verdin, J. P. (2013). Operational evapotranspiration mapping using remote sensing and weather datasets: A new parameterization for the SSEB approach. *Journal of the American Water Resources Association, 49*(3), 577–591. https://doi.org/10.1111/jawr.12057

Sun, Q., Miao, C., Duan, Q., Ashouri, H., Sorooshian, S., & Hsu, K.-L. (2018). A review of global precipitation data sets: Data sources, estimation, and intercomparisons. *Reviews of Geophysics, 56*(1), 79–107. https://doi.org/10.1002/2017RG000574

Tamiminia, H., Salehi, B., Mahdianpari, M., Quackenbush, L., Adeli, S., & Brisco, B. (2020). Google Earth Engine for geo-big data applications: A meta-analysis and systematic review. *ISPRS Journal of Photogrammetry and Remote Sensing, 164*, 152–170. https://doi.org/10.1016/j.isprsjprs.2020.04.001

Tapley, B. D., Bettadpur, S., Ries, J. C., Thompson, P. F., & Watkins, M. M. (2004). GRACE measurements of mass variability in the Earth system. *Science, 305*(5683), 503–505. https://doi.org/10.1126/science.1099192

Tellman, B., Sullivan, J. A., Kuhn, C., Kettner, A. J., Doyle, C. S., Brakenridge, G. R., Erickson, T. A., & Slayback, D. A. (2021). Satellite imaging reveals increased proportion of population exposed to floods. *Nature, 596*(7870), 80–86. https://doi.org/10.1038/s41586-021-03695-w

Velastegui-Montoya, A., Montalván-Burbano, N., Carrión-Mero, P., Rivera-Torres, H., Sadeck, L., & Adami, M. (2023). Google Earth Engine: A global analysis and future trends. *Remote Sensing, 15*(14), 3675. https://doi.org/10.3390/rs15143675

Vicente-Serrano, S. M., Beguería, S., & López-Moreno, J. I. (2010). A multiscalar drought index sensitive to global warming: The standardized precipitation evapotranspiration index. *Journal of Climate, 23*(7), 1696–1718. https://doi.org/10.1175/2009JCLI2909.1

Wu, Q. (2020). geemap: A Python package for interactive mapping with Google Earth Engine. *Journal of Open Source Software, 5*(51), 2305. https://doi.org/10.21105/joss.02305

Wulder, M. A., White, J. C., Loveland, T. R., Woodcock, C. E., Belward, A. S., Cohen, W. B., Fosnight, E. A., Shaw, J., Masek, J. G., & Roy, D. P. (2016). The global Landsat archive: Status, consolidation, and direction. *Remote Sensing*

of Environment, 185, 271–283. https://doi.org/10.1016/j.rse.2015.11.032

Xu, H. (2006). Modification of normalised difference water index (NDWI) to enhance open water features in remotely sensed imagery. *International Journal of Remote Sensing, 27*(14), 3025–3033. https://doi.org/10.1080/01431160600589179

Yang, L., Driscol, J., Sarigai, S., Wu, Q., Chen, H., & Lippitt, C. D. (2022). Google Earth Engine and artificial intelligence (AI): A comprehensive review. *Remote Sensing, 14*(14), 3253. https://doi.org/10.3390/rs14143253

Yao, F., Livneh, B., Rajagopalan, B., Wang, J., Crétaux, J.-F., Wada, Y., & Berge-Nguyen, M. (2023). Satellites reveal widespread decline in global lake water storage. *Science, 380*(6646), 743–749. https://doi.org/10.1126/science.abo2812

Zhao, Q., Yu, L., Li, X., Peng, D., Zhang, Y., & Gong, P. (2021). Progress and trends in the application of Google Earth Engine. *Remote Sensing, 13*(18), 3778. https://doi.org/10.3390/rs13183778

BÖLÜM 5

DEEP LEARNING FOR STREAMFLOW PREDICTION: LONG SHORT-TERM MEMORY NETWORKS AND THE CHANGING PRACTICE OF HYDROLOGICAL MODELLING

YILDIRIM BAYAZIT[1]

Introduction

Predicting how much water a river will carry tomorrow, next month or in a future climate is one of the oldest tasks in hydrology. For most of the twentieth century the answer came from conceptual or physically based models. These models describe a catchment as a set of connected stores, such as snow, soil and groundwater, and route water between them with equations whose parameters are calibrated against observed discharge. They have served water management well, but they share two persistent weaknesses. Calibration is tied to individual gauged catchments, so transferring parameters to ungauged basins is difficult, and model structures carry assumptions that may not hold everywhere.

Over the last decade a different approach has moved from the margins of the field to its centre. Deep learning models, and in

[1] Doçent Dr., Bilecik Şeyh Edebali University, Faculty of Engineering, Department of Civil Engineering, ORCID: 0000-0002-8699-4741

particular Long Short-Term Memory (LSTM) networks, learn the relationship between meteorological inputs and streamflow directly from data. When trained on hundreds of catchments at once, they have repeatedly matched or outperformed well-established hydrological models in benchmark studies (Kratzert et al., 2018; Kratzert, Klotz, Shalev, et al., 2019). In 2024 an LSTM-based system was shown to provide reliable flood forecasts in ungauged watersheds at a global scale and is now used operationally in more than 80 countries (Nearing et al., 2024).

This chapter reviews that development from the point of view of a water resources engineer. It briefly traces the path from early neural networks to deep learning, explains how an LSTM represents a catchment, and summarises the evidence on its performance. It then discusses prediction in ungauged basins, extremes, uncertainty and climate change, as well as the growing interest in hybrid models that combine learning with physical knowledge. The final sections consider what these methods mean for Türkiye and offer practical guidance for researchers who want to use them.

From Artificial Neural Networks to Deep Learning

Neural networks are not new to hydrology. By the late 1990s, feedforward networks had been applied widely to rainfall-runoff modelling, river stage forecasting and water quality prediction, and an ASCE task committee reviewed their concepts and early results (ASCE Task Committee on Application of Artificial Neural Networks in Hydrology, 2000). Studies in this period, including early work on river flow modelling with neural networks (Kişi, 2004), showed that such models could reproduce observed flows well. Reviews covering the following fifteen years documented a steady growth in artificial intelligence methods for streamflow forecasting, from neural networks to support vector machines and hybrid approaches (Mosavi et al., 2018; Yaseen et al., 2015).

Most of these early models, however, were small, trained on a single station and fed with lagged values of rainfall and flow chosen by the modeller. Their success often depended on careful input selection, and they had no natural way to represent the slow storage processes that make catchments remember past conditions. Deep learning changed the scale and the structure of the problem. Larger networks, better training algorithms and cheaper computation made it possible to train models on long sequences and on many catchments at once (Shen, 2018; Sit et al., 2020).

How an LSTM Represents a Catchment

The LSTM was proposed to overcome a basic difficulty of recurrent neural networks: their inability to learn dependencies that extend over many time steps (Hochreiter & Schmidhuber, 1997). Its key element is a cell state, a vector that is carried from one time step to the next and modified by three gates. The forget gate decides how much of the previous state to keep, the input gate decides how much new information to add, and the output gate decides what part of the state is passed on to produce the prediction. All three gates are learned from data.

This structure has an intuitive hydrological reading. The cell state behaves like a set of storages that fill and drain over time, and the gates control inflow, retention and release. Kratzert et al. (2018) showed that individual cells in a trained LSTM can track quantities resembling snow accumulation and melt, even though the model was never told that snow exists. Lees et al. (2022) later found that LSTMs trained only on meteorological inputs develop internal states that closely track soil moisture and snow storage. These results do not make an LSTM a physical model, but they explain why it handles memory effects better than earlier networks.

Large-Sample Datasets and Regional Training

A deep network has many parameters, and training it on a single catchment invites overfitting. The breakthrough came from training one model on many catchments simultaneously, using static catchment attributes such as area, elevation, soil properties and climate indices as additional inputs. This approach depends on large-sample datasets. CAMELS, which provides daily meteorology, streamflow and attributes for 671 catchments in the contiguous United States, became the standard test bed (Addor et al., 2017). Similar datasets followed for Great Britain, Brazil, Chile, Australia and other regions, and Caravan brought several of them together into a single global collection of 6,830 catchments with harmonised forcing and attributes (Kratzert et al., 2023).

Training across such samples allows the network to learn how hydrological behaviour varies with catchment characteristics. Kratzert, Klotz, Shalev, et al. (2019) trained a single LSTM variant on 531 CAMELS basins and showed that it outperformed conceptual and process-based models that had been calibrated either regionally or separately for each basin. The lesson is important for regions with limited data: a model that has seen many catchments can carry knowledge from data-rich to data-poor places.

Performance Against Established Models

The evidence that LSTMs are competitive with established hydrological models now comes from several continents and from independent research groups. Table 1 summarises a selection of benchmark studies. Performance in these studies is usually measured with the Nash-Sutcliffe efficiency or the Kling-Gupta efficiency, both of which compare simulated and observed flows over long periods (Gupta et al., 2009).

Table 1. Selected Benchmark Studies Comparing LSTM Networks with Established Hydrological Models

Study	Region and sample	Benchmark models	Main result
Kratzert et al. (2018)	241 CAMELS catchments, United States	SAC-SMA coupled with Snow-17	LSTM performed comparably to or better than the benchmark
Kratzert, Klotz, Shalev, et al. (2019)	531 CAMELS catchments, United States	Conceptual and process-based models calibrated per basin and regionally	One LSTM variant trained on all basins outperformed the benchmarks on average
Gauch et al. (2021)	516 catchments, United States	US National Water Model	Higher median NSE at both daily and hourly time steps
Lees et al. (2021)	669 catchments, Great Britain	Four lumped conceptual models	Median NSE of 0.88 for the LSTM, above all benchmarks
Arsenault et al. (2023)	148 catchments, northeastern North America (ungauged mode)	Three conceptual models with six regionalisation methods	Median NSE of 0.78 against 0.58 to 0.63
Nearing et al. (2024)	5,680 gauges, global	GloFAS	Five-day forecasts as reliable as GloFAS nowcasts for events up to a 5-year return period

Source: Compiled by the author from the cited studies. NSE: Nash-Sutcliffe efficiency.

Two points stand out from these comparisons. First, the advantage of LSTMs is not limited to one dataset or one country. Second, the gap tends to be largest when models are evaluated outside the conditions they were trained on, which is exactly where hydrological practice needs the most help. Gauch et al. (2021) also showed that one network can produce consistent daily and hourly

predictions, while Feng et al. (2020) demonstrated that feeding recent discharge observations into the model improves short-term forecasts considerably.

Prediction in Ungauged Basins and Global Flood Forecasting

Prediction in ungauged basins has long been one of the central problems of hydrology. Kratzert, Klotz, Herrnegger, et al. (2019) tested LSTMs on basins that were completely excluded from training and found that these out-of-sample predictions were, on average, at least as accurate as those of a conceptual model calibrated on the same basins. Arsenault et al. (2023) reached a similar conclusion for 148 catchments in northeastern North America, where an LSTM achieved a median Nash-Sutcliffe efficiency of 0.78 in ungauged mode, compared with 0.58 to 0.63 for three conceptual models combined with six regionalisation methods.

The most visible application to date is global flood forecasting. Nearing et al. (2024) trained an LSTM-based system on 5,680 streamflow gauges and compared it with the Global Flood Awareness System (GloFAS). For events with return periods of up to five years, forecasts with a lead time of five days were as reliable as GloFAS nowcasts, even though the evaluation basins were treated as ungauged. The system now produces public forecasts in more than 80 countries. For countries whose gauge networks are sparse or whose data are not openly shared, this is a strong argument for regional and global learning.

Extremes, Uncertainty and Climate Change

A common objection to data-driven models is that they cannot extrapolate beyond the range of their training data. The evidence here is more encouraging than many expected, but it is not settled. Frame et al. (2022) withheld large events from training and found that LSTMs still predicted extreme flows more accurately than conceptual and process-based benchmarks. Interestingly, adding a

mass conservation constraint to the network did not improve these predictions.

Uncertainty is another practical concern, since a forecast without a measure of confidence is of limited use to a reservoir operator or a flood warning centre. Klotz et al. (2022) developed benchmarking procedures for probabilistic deep learning and showed that mixture density networks can produce well-calibrated predictive distributions for streamflow. Climate change projections pose a harder test, because future temperature and evaporative demand may move outside the historical range. Wi and Steinschneider (2022) found that LSTMs can respond to warming in physically questionable ways, and that training on many diverse basins or adding information from process-based models leads to more plausible projections. Studies that use deep learning for climate impact assessment should therefore test the response of their models to controlled changes in temperature before using them for projections.

Interpretability and Hybrid Models

High accuracy alone does not satisfy hydrologists, who also want models that are right for the right reasons (Kirchner, 2006). Nearing et al. (2021) argued that machine learning does not make hydrological science obsolete but changes its role: theory becomes a source of hypotheses to be tested against what the networks have learned, and of constraints where data are scarce. Tools that examine internal states, such as the probing of LSTM cells for soil moisture and snow, are one way to open the black box (Lees et al., 2022).

A second response is to merge learning with physical structure. Process-guided deep learning adds physical constraints to the loss function or the architecture, an idea demonstrated early on for lake temperature prediction (Read et al., 2019). Jiang et al. (2020) embedded a conceptual hydrological model inside a neural network,

while Feng et al. (2022) introduced differentiable models in which a neural network learns the parameters of a process-based model across regions. These models approach the accuracy of a pure LSTM while producing physically meaningful variables such as evapotranspiration and storage that were not used in training. Newer architectures are also being tested. Liu et al. (2024) found that a standard Transformer performs poorly for streamflow but that a modified version can match LSTM accuracy, which suggests that the memory structure of the LSTM remains well suited to hydrological problems.

Opportunities in Türkiye

Türkiye has a long history of hydrological measurement but faces several conditions that make the international findings especially relevant. Many rivers are regulated by dams and irrigation diversions, flow records are not always continuous or openly available, and climate projections point to lower water availability in much of the country, especially in the south and west. Deep learning studies in Türkiye have so far mostly focused on single stations. Kilinc and Haznedar (2022) combined an LSTM with a genetic algorithm to forecast daily flows at two stations on the Euphrates, and Haznedar et al. (2023) coupled an LSTM with particle swarm optimisation for three stations in the Seyhan Basin, reporting higher accuracy than standalone LSTM and neuro-fuzzy models.

These studies show that the methods work with Turkish data, but they do not yet exploit the main strength of modern LSTMs, which is learning across many catchments. Türkiye was not among the regions covered in the first release of Caravan (Kratzert et al., 2023). A national large-sample dataset that combines streamflow from the State Hydraulic Works and other agencies with meteorological forcing and catchment attributes would allow

regional models to be trained and tested in a consistent way. It would also make it possible to evaluate global systems such as the one described by Nearing et al. (2024) against local observations, which is a necessary step before such forecasts are used in national flood warning.

Practical Guidance for Researchers

For researchers starting with deep learning in hydrology, the experience gathered over recent years suggests several good practices:

- Train on many catchments where possible, and include static attributes so that the model can distinguish between them.
- Split data by time and, for regionalisation studies, by basin, so that test catchments are never seen during training.
- Compare results with at least one calibrated conceptual model and report the same metrics for both, since a high efficiency score has meaning only relative to a benchmark.
- Report uncertainty, either through probabilistic outputs or through ensembles of independently trained networks.
- Examine the behaviour of the model under altered inputs, for example warmer temperatures, before using it outside the observed range.
- Share code and data splits so that others can reproduce the results, which is now common practice in the field.

Conclusion

In less than a decade, LSTM networks have gone from an experimental idea to a standard benchmark in streamflow prediction and to the core of an operational global flood forecasting system. Their success rests less on the network itself than on large-sample datasets and on training strategies that let one model learn from many catchments. The open questions now concern extremes, climate change and interpretability, and the most promising answers combine learning with hydrological knowledge rather than replacing it.

For Türkiye, the immediate opportunity is clear. Building an open, national large-sample dataset and testing regional and hybrid models on it would allow the country to benefit from these advances and to evaluate them critically against its own rivers. Hydrological understanding remains essential in this work, because it is what allows us to judge when a model is right and, just as importantly, why.

References

Addor, N., Newman, A. J., Mizukami, N., & Clark, M. P. (2017). The CAMELS data set: Catchment attributes and meteorology for large-sample studies. *Hydrology and Earth System Sciences, 21*(10), 5293–5313. https://doi.org/10.5194/hess-21-5293-2017

Arsenault, R., Martel, J.-L., Brunet, F., Brissette, F., & Mai, J. (2023). Continuous streamflow prediction in ungauged basins: Long short-term memory neural networks clearly outperform traditional hydrological models. *Hydrology and Earth System Sciences, 27*(1), 139–157. https://doi.org/10.5194/hess-27-139-2023

ASCE Task Committee on Application of Artificial Neural Networks in Hydrology. (2000). Artificial neural networks in hydrology. I: Preliminary concepts. *Journal of Hydrologic Engineering, 5*(2), 115–123. https://doi.org/10.1061/(ASCE)1084-0699(2000)5:2(115)

Feng, D., Fang, K., & Shen, C. (2020). Enhancing streamflow forecast and extracting insights using long-short term memory networks with data integration at continental scales. *Water Resources Research, 56*(9), e2019WR026793. https://doi.org/10.1029/2019WR026793

Feng, D., Liu, J., Lawson, K., & Shen, C. (2022). Differentiable, learnable, regionalized process-based models with multiphysical outputs can approach state-of-the-art hydrologic prediction accuracy. *Water Resources Research, 58*(10), e2022WR032404. https://doi.org/10.1029/2022WR032404

Frame, J. M., Kratzert, F., Klotz, D., Gauch, M., Shalev, G., Gilon, O., Qualls, L. M., Gupta, H. V., & Nearing, G. S. (2022).

Deep learning rainfall–runoff predictions of extreme events. *Hydrology and Earth System Sciences, 26*(13), 3377–3392. https://doi.org/10.5194/hess-26-3377-2022

Gauch, M., Kratzert, F., Klotz, D., Nearing, G., Lin, J., & Hochreiter, S. (2021). Rainfall–runoff prediction at multiple timescales with a single Long Short-Term Memory network. *Hydrology and Earth System Sciences, 25*(4), 2045–2062. https://doi.org/10.5194/hess-25-2045-2021

Gupta, H. V., Kling, H., Yilmaz, K. K., & Martinez, G. F. (2009). Decomposition of the mean squared error and NSE performance criteria: Implications for improving hydrological modelling. *Journal of Hydrology, 377*(1–2), 80–91. https://doi.org/10.1016/j.jhydrol.2009.08.003

Haznedar, B., Kilinc, H. C., Ozkan, F., & Yurtsever, A. (2023). Streamflow forecasting using a hybrid LSTM-PSO approach: The case of Seyhan Basin. *Natural Hazards, 117*(1), 681–701. https://doi.org/10.1007/s11069-023-05877-3

Hochreiter, S., & Schmidhuber, J. (1997). Long short-term memory. *Neural Computation, 9*(8), 1735–1780. https://doi.org/10.1162/neco.1997.9.8.1735

Jiang, S., Zheng, Y., & Solomatine, D. (2020). Improving AI system awareness of geoscience knowledge: Symbiotic integration of physical approaches and deep learning. *Geophysical Research Letters, 47*(13), e2020GL088229. https://doi.org/10.1029/2020GL088229

Kilinc, H. C., & Haznedar, B. (2022). A hybrid model for streamflow forecasting in the basin of Euphrates. *Water, 14*(1), 80. https://doi.org/10.3390/w14010080

Kirchner, J. W. (2006). Getting the right answers for the right reasons: Linking measurements, analyses, and models to

advance the science of hydrology. *Water Resources Research, 42*(3), W03S04. https://doi.org/10.1029/2005WR004362

Kişi, Ö. (2004). River flow modeling using artificial neural networks. *Journal of Hydrologic Engineering, 9*(1), 60–63. https://doi.org/10.1061/(ASCE)1084-0699(2004)9:1(60)

Klotz, D., Kratzert, F., Gauch, M., Keefe Sampson, A., Brandstetter, J., Klambauer, G., Hochreiter, S., & Nearing, G. (2022). Uncertainty estimation with deep learning for rainfall–runoff modeling. *Hydrology and Earth System Sciences, 26*(6), 1673–1693. https://doi.org/10.5194/hess-26-1673-2022

Kratzert, F., Klotz, D., Brenner, C., Schulz, K., & Herrnegger, M. (2018). Rainfall–runoff modelling using Long Short-Term Memory (LSTM) networks. *Hydrology and Earth System Sciences, 22*(11), 6005–6022. https://doi.org/10.5194/hess-22-6005-2018

Kratzert, F., Klotz, D., Herrnegger, M., Sampson, A. K., Hochreiter, S., & Nearing, G. S. (2019). Toward improved predictions in ungauged basins: Exploiting the power of machine learning. *Water Resources Research, 55*(12), 11344–11354. https://doi.org/10.1029/2019WR026065

Kratzert, F., Klotz, D., Shalev, G., Klambauer, G., Hochreiter, S., & Nearing, G. (2019). Towards learning universal, regional, and local hydrological behaviors via machine learning applied to large-sample datasets. *Hydrology and Earth System Sciences, 23*(12), 5089–5110. https://doi.org/10.5194/hess-23-5089-2019

Kratzert, F., Nearing, G., Addor, N., Erickson, T., Gauch, M., Gilon, O., Gudmundsson, L., Hassidim, A., Klotz, D., Nevo, S., Shalev, G., & Matias, Y. (2023). Caravan - A global

community dataset for large-sample hydrology. *Scientific Data, 10*, 61. https://doi.org/10.1038/s41597-023-01975-w

Lees, T., Buechel, M., Anderson, B., Slater, L., Reece, S., Coxon, G., & Dadson, S. J. (2021). Benchmarking data-driven rainfall–runoff models in Great Britain: A comparison of long short-term memory (LSTM)-based models with four lumped conceptual models. *Hydrology and Earth System Sciences, 25*(10), 5517–5534. https://doi.org/10.5194/hess-25-5517-2021

Lees, T., Reece, S., Kratzert, F., Klotz, D., Gauch, M., De Bruijn, J., Kumar Sahu, R., Greve, P., Slater, L., & Dadson, S. J. (2022). Hydrological concept formation inside long short-term memory (LSTM) networks. *Hydrology and Earth System Sciences, 26*(12), 3079–3101. https://doi.org/10.5194/hess-26-3079-2022

Liu, J., Bian, Y., Lawson, K., & Shen, C. (2024). Probing the limit of hydrologic predictability with the Transformer network. *Journal of Hydrology, 637*, 131389. https://doi.org/10.1016/j.jhydrol.2024.131389

Mosavi, A., Ozturk, P., & Chau, K.-W. (2018). Flood prediction using machine learning models: Literature review. *Water, 10*(11), 1536. https://doi.org/10.3390/w10111536

Nearing, G., Cohen, D., Dube, V., Gauch, M., Gilon, O., Harrigan, S., Hassidim, A., Klotz, D., Kratzert, F., Metzger, A., Nevo, S., Pappenberger, F., Prudhomme, C., Shalev, G., Shenzis, S., Tekalign, T. Y., Weitzner, D., & Matias, Y. (2024). Global prediction of extreme floods in ungauged watersheds. *Nature, 627*(8004), 559–563. https://doi.org/10.1038/s41586-024-07145-1

Nearing, G. S., Kratzert, F., Sampson, A. K., Pelissier, C. S., Klotz, D., Frame, J. M., Prieto, C., & Gupta, H. V. (2021). What role does hydrological science play in the age of machine learning?. *Water Resources Research, 57*(3), e2020WR028091. https://doi.org/10.1029/2020WR028091

Read, J. S., Jia, X., Willard, J., Appling, A. P., Zwart, J. A., Oliver, S. K., Karpatne, A., Hansen, G. J. A., Hanson, P. C., Watkins, W., Steinbach, M., & Kumar, V. (2019). Process-guided deep learning predictions of lake water temperature. *Water Resources Research, 55*(11), 9173–9190. https://doi.org/10.1029/2019WR024922

Shen, C. (2018). A transdisciplinary review of deep learning research and its relevance for water resources scientists. *Water Resources Research, 54*(11), 8558–8593. https://doi.org/10.1029/2018WR022643

Sit, M., Demiray, B. Z., Xiang, Z., Ewing, G. J., Sermet, Y., & Demir, I. (2020). A comprehensive review of deep learning applications in hydrology and water resources. *Water Science and Technology, 82*(12), 2635–2670. https://doi.org/10.2166/wst.2020.369

Wi, S., & Steinschneider, S. (2022). Assessing the physical realism of deep learning hydrologic model projections under climate change. *Water Resources Research, 58*(9), e2022WR032123. https://doi.org/10.1029/2022WR032123

Yaseen, Z. M., El-shafie, A., Jaafar, O., Afan, H. A., & Sayl, K. N. (2015). Artificial intelligence based models for stream-flow forecasting: 2000–2015. *Journal of Hydrology, 530*, 829–844. https://doi.org/10.1016/j.jhydrol.2015.10.038

BÖLÜM 6

OCCUPATIONAL SAFETY IN 3D CONCRETE PRINTING: HAZARD TRANSFORMATION AND A TASK-BASED RISK MANAGEMENT FRAMEWORK

ÖZGE ALBOĞA[1]

Introduction

Three-dimensional concrete printing (3DCP) is an additive manufacturing technique in which cementitious materials are deposited layer by layer according to a digitally defined printing path. Unlike conventional cast-in-place concrete construction, the process relies on automated material deposition using gantry-based or robotic-arm printing systems. However, the use of automated equipment does not mean that the entire construction process is automated. In their review of 137 large-scale 3DCP projects, Hasani and Dorafshan (2024) identified several practical limitations, including quality-control difficulties, manual interventions during printing, and the continued reliance on conventional construction activities. Their findings indicate that the level of automation varies

[1] Dr., Independent Researcher, ORCID: 0000-0002-2848-8373

across projects and that 3DCP should not be considered a complete replacement for conventional construction methods.

The coexistence of automated and manual operations has implications for construction planning and work organization. Activities such as equipment preparation, material handling, printing, inspection, and subsequent construction work must be coordinated within the overall production process. Sari et al. (2025) examined this issue in hybrid 3D-printed modular construction and developed a work breakdown structure and construction process framework covering off-site and on-site activities. Their study identified the sequencing and interdependencies of construction tasks, including points where automated and conventional operations are integrated. Although their framework primarily addresses construction planning and execution, the distinction between work activities provides a useful basis for examining occupational hazards at different stages of production.

Occupational safety and health (OSH) is an important consideration in the adoption of construction robotics. Automation may reduce workers' involvement in certain physically demanding or hazardous activities, but it can also introduce risks associated with moving equipment, human intervention, and interactions between workers and robotic systems. In a review of robotics and automation in construction, Earnest et al. (2026) identified mechanical, ergonomic, psychosocial, and environmental risk categories, including hazards relevant to additive manufacturing. More specifically, Rojas & Hasanzadeh (2025) examined human factors in 3DCP and identified different worker roles and levels of human–robot interaction (HRI). Their findings highlight the importance of considering workers who perform supporting activities during

printing, rather than focusing exclusively on the operation of the printer.

These observations suggest that safety in 3DCP should be assessed across the construction process, not only during material deposition. This chapter examines the coexistence of automated and human-performed activities and develops a task-based conceptual framework linking work stages, foreseeable exposure mechanisms, control priorities, and verification conditions. Its distinctive focus is on how hazards may be reduced or modified, retained or relocated, or introduced by changes in production and worker–robot interaction. The proposed framework is intended to organize preliminary hazard identification and preventive planning; it is not an empirically validated risk assessment method.

The discussion takes a narrative, concept-oriented approach: published 3DCP process studies, worker–robot interaction research, and occupational safety guidance are considered together to identify task-level safety questions. It does not claim to be an exhaustive or systematic review, and evidence from general robotics or industrial settings is distinguished from observations specific to 3DCP.

3D Concrete Printing Systems and Construction Processes

The application of 3DCP in building construction generally involves two production arrangements: on-site printing and off-site fabrication. In on-site applications, concrete elements are printed at the construction site, whereas off-site fabrication involves producing components at a separate facility and subsequently transporting them for installation. Hasani and Dorafshan (2024) identified both approaches in their review of completed 3DCP projects and discussed their practical differences, particularly in relation to

transportation, equipment requirements, and construction procedures. Off-site production can also be combined with conventional prefabrication techniques, allowing printed and non-printed components to be incorporated into the same building. The resulting construction process therefore depends not only on the printing technology but also on where production takes place and how the printed elements are integrated into the overall structure.

The printing system is another factor influencing the organization of construction activities. Gantry-based printers and robotic-arm systems are among the technologies used in large-scale 3DCP applications. Gantry systems operate within a defined printing area, while robotic arms provide different possibilities for nozzle movement and positioning. Their practical limitations also differ. Gantry-based equipment may require considerable assembly before printing begins, whereas robotic-arm systems have a limited operating reach unless they are repositioned or mounted on mobile platforms. Hasani and Dorafshan (2024) documented these differences and reported that gantry-based systems were the most frequently used configuration among the on-site projects examined in their review. These characteristics influence equipment selection, site preparation, and the arrangement of work around the printing system.

Regardless of the equipment configuration, concrete printing involves several activities beyond automated material deposition. Digital model preparation and toolpath generation precede printer setup, calibration, and material preparation. During printing, the movement of the print head and the delivery of cementitious material must be coordinated to produce the intended geometry. Sari et al. (2025) described these activities in a construction process

framework developed for hybrid 3D-printed modular buildings, which also includes dimensional inspection, material testing, curing, and preparation for transportation. The importance of coordinating material properties with printing operations is supported by Q. Wang et al. (2025) who investigated the relationships between rheological properties, printing parameters, and the characteristics of extruded cementitious filaments. Their findings demonstrate that the quality of printed material is influenced by the interaction between material behavior and printing conditions.

The integration of reinforcement remains an important consideration when 3DCP is used for structural applications. Unlike conventional concrete casting, the layer-by-layer deposition process requires reinforcement placement to be coordinated with the printing sequence or subsequent construction activities. Hasani and Dorafshan (2024) reported that conventional reinforcement was commonly installed manually in the large-scale projects they examined, limiting the degree of automation achieved in practice. Alternative reinforcement approaches continue to be investigated. For example, Cao et al. (2025) experimentally examined an in-situ mesh fabrication technique intended to improve reinforcement continuity within printed concrete elements. Although such developments demonstrate possibilities for further automation, they should be distinguished from reinforcement procedures already used in completed construction projects.

The relationship between printing and subsequent construction activities is particularly evident in prefabricated applications. Sari et al. (2025) developed a framework in which off-site production of printed and precast components is followed by transportation, lifting, positioning, connection, inspection, and

building services installation. More recently, H. Wang et al. (2026) presented a modular prefabricated 3D-printed concrete residence using a process that connects digital modeling, module division, factory production, and on-site assembly. These studies illustrate how the printing stage forms part of a broader construction sequence. However, the workflows developed for prefabricated modular systems should not be assumed to represent all on-site printing applications, where equipment deployment and construction activities may be organized differently.

For the purposes of this chapter, 3DCP is treated as a sequence of interconnected activities rather than an isolated automated operation. Differences in equipment, production location, reinforcement practices, and subsequent construction tasks determine where and when workers may encounter hazards.

Occupational Safety and Health Implications of 3D Concrete Printing

The occupational safety implications of 3DCP are closely related to changes in how construction activities are performed and how workers interact with automated equipment. Certain operations associated with conventional concrete construction may be reduced or modified, while others remain necessary throughout the printing process. At the same time, the introduction of robotic systems creates hazards that are less prominent in conventional construction. Rojas et al. (2026) identified both traditional hazards, including falls and struck-by incidents, and emerging concerns involving robotic equipment, new materials, and operator workload. Similarly, Earnest et al. (2026) emphasized that the safety implications of construction automation depend on the technology and the tasks being performed. These findings suggest that the adoption of 3DCP should not be interpreted as an overall reduction in occupational risk without

considering the activities that remain and the additional hazards associated with automation.

One potential safety benefit of 3DCP is the reduction of worker involvement in selected conventional construction operations. Depending on the printing method and structural requirements, formwork installation and removal, manual concrete placement, and vibration-related activities may be reduced or avoided. Rojas & Hasanzadeh (2025) examined industry perceptions of these benefits through a survey of 553 architecture, engineering, and construction professionals. Their findings indicated that respondents generally viewed 3DCP as having the potential to reduce exposure to hazards associated with conventional concrete construction. However, these findings reflect professional perceptions rather than measured reductions in occupational injuries. Furthermore, the continued use of reinforcement, temporary supports, and other conventional construction activities means that the extent of hazard reduction is likely to depend on the specific printing process and project configuration.

Mechanical hazards are among the more immediate safety concerns associated with robotic construction equipment. Workers may be exposed to struck-by or caught-in/between hazards when entering areas containing moving robotic arms, print heads, or other mechanical components. The importance of these mechanisms is supported by research on industrial robot incidents. Sanders et al. (2024) analyzed 77 robot-related accidents reported to the U.S. Occupational Safety and Health Administration between 2015 and 2022, identifying injury patterns associated with stationary and mobile robots. Zuo et al. (2025) examined 303 human–robot interaction incidents and identified seven incident archetypes,

including unexpected activation, faulty commands, and sensor or communication errors. Although neither dataset is specific to 3DCP, the findings provide evidence of accident mechanisms that warrant consideration when planning activities around robotic printing systems. Their relevance to individual 3DCP configurations must be assessed rather than assumed.

Occupational health concerns also require attention beyond direct contact with moving equipment. Earnest et al. (2026) classified risks associated with construction robotics into mechanical, ergonomic, psychosocial, and environmental categories. For additive manufacturing and 3D printing, their review identified potential concerns involving musculoskeletal disorders, noise, dust, electrical hazards, and working conditions. In 3DCP applications, material preparation, equipment operation, cleaning, and maintenance represent activities in which these concerns should be evaluated. Nevertheless, the hazards reported across additive manufacturing technologies cannot be directly translated into exposure levels for cement-based printing. Actual exposure depends on the materials, equipment, work environment, and protective measures used. Consequently, claims regarding reductions in dust exposure, noise, or musculoskeletal strain require task-specific evidence.

A further consideration is the stability of concrete elements during printing. Because successive layers are deposited before the material has fully hardened, the printed element must retain its geometry while supporting the increasing load from additional layers. Zhu et al. (2024) investigated buildability problems in complex 3D-printed concrete geometries using a peridynamic modeling approach, demonstrating the relevance of material

behavior and structural response during the printing process. Although their work addressed structural buildability rather than worker injury outcomes, it identifies a technical condition that is relevant when considering the safety of activities performed near freshly printed elements. The possibility of deformation or instability should therefore be distinguished from documented occupational incidents, for which separate evidence would be required.

Traditional construction hazards may also remain during activities performed before and after printing. In hybrid 3D-printed modular construction, Sari et al. (2025) described a sequence that includes site preparation, component transportation, lifting, positioning, mechanical connections, building services installation, and finishing activities. These operations are not eliminated by automating the fabrication of concrete components. Their presence indicates that safety assessment should extend beyond the operation of the printer to cover the supporting and subsequent construction tasks. The distinction is particularly important when comparing on-site printing with off-site fabrication, as the location and sequence of activities influence where workers and equipment operate.

The literature therefore supports distinguishing three patterns of hazard transformation: hazards reduced or modified when conventional tasks are replaced; hazards retained or relocated to supporting, handling, and installation operations; and hazards introduced or made more salient by robotic movement and shared workspaces. These are conceptual categories, not measured changes in accident frequency. The subsequent analysis considers how worker roles and equipment operating states shape the relevance of each pattern.

Human–Robot Interaction and Hybrid Construction Activities

HRI in 3DCP involves more than the operation of a robotic printer. Although material deposition follows a programmed sequence, human involvement remains necessary for preparing the equipment, monitoring the process, performing supporting activities, and responding to operational interruptions. The extent of this involvement varies according to the printing system and the organization of construction work. Rojas & Hasanzadeh (2025) distinguished several roles in 3DCP projects, including programmers, operators, maintenance personnel, supervisors, and workers performing complementary construction tasks. Their classification highlights an important distinction between personnel who monitor or control the equipment and those who must physically enter or work near the printing area. These roles cannot be assumed to involve the same level of interaction with the robotic system.

The timing of human involvement is particularly relevant to the organization of hybrid construction activities. Rojas & Hasanzadeh (2025) differentiated between contributory tasks performed during printing and sequential tasks that require printing operations to be interrupted. Examples of contributory tasks include placing supports and installing mechanical, electrical, and plumbing (MEP) boxes, whereas sequential tasks may involve installing structural supports or lintels. Their survey also showed that respondents from 3DCP companies considered MEP box placement during printing relatively straightforward. However, perceived task simplicity does not establish that an activity can be performed safely near moving robotic equipment. Whether a task can proceed during printing depends on the required worker access, the movements of the printer, and the protective measures available. These conditions

need to be considered when determining the sequence of construction activities.

Human–robot collaboration (HRC), which involves coordinated human and robotic contributions to a task, also introduces considerations beyond physical proximity. Antwi et al. (2026) systematically reviewed 163 studies of HRC in construction and organized the investigated human factors into cognitive, affective, physical, and perceived robot acceptance and usability dimensions. Their synthesis identified factors such as cognitive workload, attention, trust, situational awareness, physical exertion, and discomfort. The review further indicated that human responses vary with task allocation, communication, robot reliability, and workplace conditions. However, much of the available evidence was obtained in controlled or virtual environments. These findings are therefore relevant to understanding possible challenges in 3DCP operations but should not be interpreted as direct measurements of worker responses on active 3DCP construction sites.

The distribution of tasks between humans and robotic systems also influences the physical demands of construction work. Sawicki et al. (2026) conducted a small-scale experimental comparison between conventional reinforced concrete production and a collaborative shotcrete 3D printing process. The study involved two teams of two workers and examined productivity alongside physiological, biomechanical, and subjective responses. The collaborative process was associated with lower values for several physical-demand indicators, including carried weight, walking distance, and time spent in uncomfortable spinal positions. However, heart rate and blood lactate concentration did not show corresponding differences, and operating the robotic system

involved substantial mental demands. Given the limited sample and the specific production method examined, the findings cannot establish that 3DCP generally reduces occupational health risks. They nevertheless illustrate why physical and cognitive demands should be considered separately when evaluating human participation in automated construction.

The coordination of automated and conventional activities becomes more complex when printed components are integrated into modular construction. Sari et al. (2025) described a hybrid production sequence involving off-site fabrication, transportation, lifting, positioning, structural connections, and subsequent building services installation. Their framework identified the dependencies between these activities and the points at which automated processes are integrated with conventional construction operations. From an occupational safety perspective, this separation of activities provides a useful basis for identifying when workers interact directly with printing equipment and when they perform tasks involving other construction machinery or installed components. The framework itself, however, was developed for construction planning rather than occupational risk assessment.

Research on construction robotics has also examined methods for monitoring worker–robot separation during shared operations. Lin et al. (2025) proposed a digital twin-enabled safety monitoring system that integrates spatial information about workers, robots, and materials and adjusts protective separation distances in response to changing conditions. The approach was evaluated in static and dynamic conflict scenarios. Although it was not developed specifically for 3DCP, it demonstrates how spatial information can be incorporated into safety monitoring during worker–robot

operations. Such technological approaches do not remove the need to determine which activities require worker access, how equipment is stopped and restarted, and how responsibilities are assigned when work conditions change.

Worker involvement in 3DCP consequently needs to be examined in terms of the specific task, printer operating state, and required proximity or access. This distinction underpins the framework developed below and avoids treating all human–robot interactions as equivalent exposure situations.

A Task-Based Framework for Hazard Identification and Risk Control

A practical hazard assessment must follow the sequence of work as well as the sequence of printing. The proposed framework therefore begins with identifiable tasks—such as printer setup, material pumping, deposition, intervention, maintenance, and component installation—and then considers how the equipment state and worker access create exposure opportunities. The three hazard-transformation patterns described above help explain why reducing one conventional activity does not necessarily remove the associated risk from the overall project.

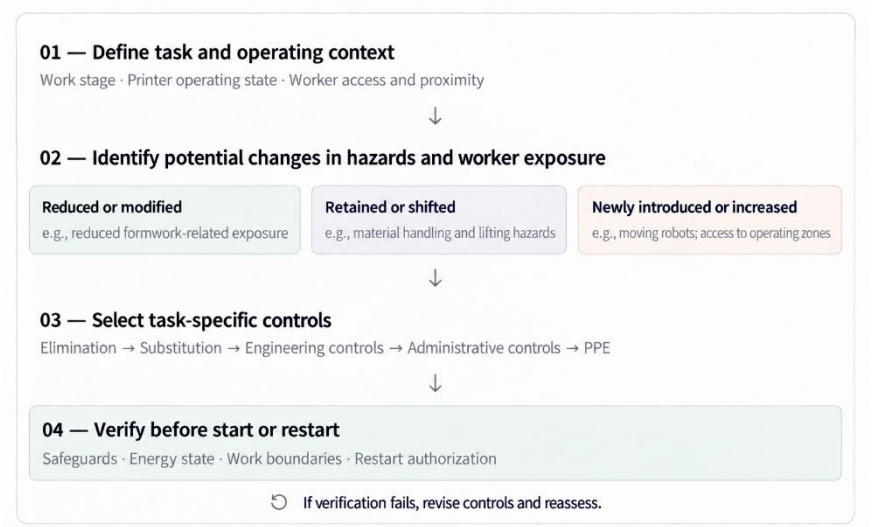
The approach is a conceptual synthesis of the 3DCP process and human–robot interaction literature discussed in this chapter, interpreted through established job hazard analysis (JHA) principles and the hierarchy of controls. It is not based on a systematic literature search or a formal quantitative evidence appraisal. JHA breaks work into activities to identify relationships among tasks, workers, equipment, and the environment (OSHA, 2002). Construction robotics research likewise advocates task-specific assessment,

prevention through design, and the hierarchy of controls (Earnest et al., 2026). Here, the construction stages documented by Sari et al., (2025) and the worker roles discussed by Rojas & Hasanzadeh, (2025) are used to structure the analysis.

The assessment follows four linked decisions. First, define the task, the printer's operating state, and the worker's required access. Second, identify the relevant hazard mechanism, including whether the exposure has been reduced, retained or transferred, or introduced through automation. Third, specify controls in priority order, favoring elimination, substitution, and engineering measures before administrative measures and personal protective equipment (National Institute for Occupational Safety and Health (NIOSH), 2024). Finally, verify the conditions for starting or resuming work. Monitoring from outside a safeguarded area, undertaking an assessed intervention after a controlled stop, and performing maintenance that requires hazardous-energy isolation are distinct situations and must not be assigned the same protective measures.

Figure 1 summarizes this task-based assessment pathway and the three patterns of hazard transformation. Table 1 translates the pathway into a concise matrix covering typical 3DCP activities. Entries indicate plausible exposure situations and illustrative controls, not observed 3DCP accidents or universal prescriptions. The final column identifies task-specific checks to be completed before work begins or resumes.

Figure 1. Proposed task-based framework for hazard identification and risk control in 3D concrete printing.



Source: Developed by the author based on OSHA (2002), NIOSH (2024), and the literature reviewed in this chapter.

The sequence in Figure 1 can be applied to a planned intervention at the print head. The initial task description identifies what the worker needs to do and whether the printer is depositing material, paused, or isolated. The hazard review then distinguishes exposures avoided through automation from those associated with worker entry and equipment restart. This leads to a control decision: preferably perform the task outside the operating envelope; otherwise evaluate the applicable safeguarded mode or hazardous-energy isolation requirement before entry. The verification step concerns the actual equipment state and authorization to resume production, not merely confirmation that the print head is stationary.

Table 1. Task-based hazard identification, control priorities, and verification points for 3D concrete printing.

Construction activity	Foreseeable hazard / exposure	Illustrative control priority	Verification before work
Planning and work zones	Conflicting routes; unintended entry near equipment	Separate work zones; define access limits and task sequence	Boundaries, responsibilities, and access routes agreed
Printer installation and calibration	Equipment shift; moving parts during setup or testing	Follow installation plan; stabilize equipment; guard test zone	Stable setup; guards and safety functions checked
Material mixing and pumping	Cement dust; wet cement; hose or pressure release	Control dust/contact; secure lines; use suitable PPE	Mixing and pressure-control procedures verified
Automated deposition	Robot/nozzle movement; entry into operating envelope	Prevent access; use appropriate engineered safeguarding	Operating envelope clear; protective functions tested
Planned worker access during printing	Contact during embedding, inspection, or adjustment	Prefer tasks outside envelope; assess safe stop or mode for entry	Printer state, access authority, and restart procedure confirmed
Cleaning and maintenance	Unexpected start; stored electrical, hydraulic, or pneumatic energy	Isolate hazardous energy where required; follow servicing procedures	Isolation and zero-energy checks completed as applicable
Post-printing site work	Unstable fresh element; conventional trades and equipment	Restrict proximity; check stability; coordinate subsequent trades	Element stability and work-area arrangements checked
Off-site component transport and installation	Suspended loads; transport movement; trapping or impact	Plan lift and placement; control exclusion zones	Lift plan, component integrity, and placement sequence verified

Source: Developed by the author based on OSHA (2002), NIOSH (2024), Hasani and Dorafshan (2024), Sari et al. (2025), Rojas and Hasanzadeh (2025), and Earnest et al. (2026).

The matrix distinguishes routine production from worker entry, intervention, maintenance, and downstream construction. The transformation categories shown in Figure 1 are deliberately not treated as risk scores: the same task may combine retained conventional exposures with newly introduced robotic hazards. The

controls and verification points must therefore be adapted to the printer configuration, manufacturer instructions, workforce, site layout, and applicable regulatory requirements.

Work requiring access to the operating space warrants a separate assessment of the necessary machine state. A production pause or emergency stop does not establish that hazardous energy has been isolated. Adjustment or troubleshooting may be possible only under a specifically assessed safeguarded operating mode; tasks involving servicing, unexpected startup, or stored energy may instead require lockout or other appropriate hazardous-energy isolation procedures. OSHA guidance distinguishes automatic operation from maintenance and entry into safeguarded spaces (OSHA, n.d.). The access decision and restart authorization should therefore be checked separately, rather than inferred from the fact that printing has stopped.

The assessment also needs to be repeated when the work arrangement changes. Moving a printer, introducing another trade, changing material-delivery routes, or modifying a lifting sequence can alter the exposure mechanism without changing the nominal task. Castleberry et al. (2026) recommended task-specific assessment in changing construction environments, while Lin et al. (2025) investigated dynamic worker–robot separation monitoring. Their findings support continued review, but do not demonstrate the effectiveness of this chapter's matrix.

The framework's intended contribution is a traceable link from construction activity and equipment state to foreseeable hazard, control priority, and a verifiable work condition. It does not estimate

accident probability, rank individual risks numerically, or certify that a safeguard is adequate. Such judgments require equipment- and project-specific evidence, and the framework itself still requires expert review and field evaluation.

Discussion and Practical Implications

The proposed framework adds an operational safety layer to research on human–robot task allocation in construction. Liu et al. (2025) organized this research around robot design, perception and interaction, and task allocation and execution; Y. Wang et al. (2026) incorporated hazard considerations into task allocation for a flooring application. The present framework addresses a related but different decision: after the work sequence has been defined, what exposure mechanisms, controls, and conditions for authorizing work should be considered at each stage of 3DCP? Its contribution lies in this task-to-control-to-verification link, rather than in a new robotics optimization method.

Production location changes which hazards persist beyond printing. Off-site fabrication moves much of deposition into a factory but introduces component handling, transportation, lifting, and on-site assembly; on-site fabrication places printer setup, material supply, and site access in the active construction environment. These differences are evident in the project reviews by Hasani & Dorafshan (2024) and the modular application documented by H. Wang et al. (2026). A single printer-focused assessment would overlook these downstream operations. The matrix retains them as separate tasks rather than assuming that off-site and on-site production share identical exposure profiles.

The greatest need for task-state differentiation arises during worker intervention. Zuo et al. (2025) reported patterns such as unexpected activation and command or communication faults in an industrial robot incident dataset, although their frequency cannot be extrapolated to 3DCP. Antwi et al. (2026) identified cognitive and organizational factors that may affect human–robot collaboration. For example, if a worker must place an embedded component near the print path, the assessment must identify whether placement can occur outside the operating envelope or requires a planned interruption, the protective state for entry, and the authority to restart. Merely describing the activity as 'collaborative' does not establish a safe operating method.

Practically, the matrix can support preconstruction coordination and short task-level safety reviews before printer setup, access to the safeguarded area, maintenance, or a change in work sequence. The verification column can be assigned to a designated responsible person and supported by project-specific records or checks. Where the required safeguard cannot be confirmed, the activity should not be authorized until its conditions have been assessed and addressed. Completion of the matrix alone is not evidence of legal compliance or safe performance.

The principal limitation is the conceptual basis of the framework. The sources reviewed cover 3DCP, industrial robotics, and broader construction automation, but they do not provide consistent injury or exposure measurements for all proposed task categories. The matrix has not been tested through site observations, expert consensus, or comparison with existing JHA records. Future validation should examine whether the task stages are sufficiently complete, whether users select appropriate controls, and whether

verification points can be applied reliably to both on-site and off-site systems.

Conclusions

Three-dimensional concrete printing changes the distribution of work rather than eliminating worker exposure. Some conventional activities may be reduced, while material handling, intervention, maintenance, and subsequent construction remain necessary. Robotic movement and shared workspaces also introduce different opportunities for hazardous contact.

This chapter distinguishes between reduced or modified, retained or relocated, and introduced hazards and uses that distinction to organize a task-based assessment pathway. The proposed matrix links construction activities and printer operating states with exposure mechanisms, control priorities, and verification conditions before work begins or resumes.

The framework is a preliminary planning aid, not a validated risk-scoring tool or a substitute for equipment-specific procedures. Future work should test its completeness and usability through expert evaluation and observation of actual 3DCP operations, particularly during worker access, maintenance, and the transition from printing to installation.

References

Antwi, N. K. A., Albeaino, G., & Nnaji, C. (2026). Human factors considerations for safe and scalable human-robot collaboration in construction: A systematic review. *Journal of Safety Research, 98*, 561–587. https://doi.org/10.1016/j.jsr.2026.08.009

Cao, X., Wu, S., & Cui, H. (2025). Experimental study on in-situ mesh fabrication for reinforcing 3D-printed concrete. *Automation in Construction, 170*, 105923. https://doi.org/10.1016/j.autcon.2024.105923

Castleberry, A., Haas, E. J., Socias-Morales, C. M., Cheng, M., & Peterson, D. R. (2026). *Safety in construction robotics*. National Institute for Occupational Safety and Health. https://www.cdc.gov/niosh/bulletin/2026/safety-in-construction-robotics.html

Earnest, G. S., Trout, D. B., Liang, C.-J., & Castleberry, A. (2026). Robotics and automation safety risks in construction. *Frontiers in Built Environment, 11*, Article 1653188. https://doi.org/10.3389/fbuil.2025.1653188

Hasani, A., & Dorafshan, S. (2024). Transforming construction? Evaluation of the state of structural 3D concrete printing in research and practice. *Construction and Building Materials, 438*, 137027. https://doi.org/10.1016/j.conbuildmat.2024.137027

Lin, X., Guo, Z., Jin, X., & Guo, H. (2025). Digital twin-enabled safety monitoring system for seamless worker-robot collaboration in construction. *Automation in Construction, 174*, 106147. https://doi.org/10.1016/j.autcon.2025.106147

Liu, J., Luo, H., & Wu, D. (2025). Human–robot collaboration in construction: Robot design, perception and interaction, and task allocation and execution. *Advanced Engineering Informatics, 65*, 103109. https://doi.org/10.1016/j.aei.2025.103109

National Institute for Occupational Safety and Health. (2024). *Hierarchy of controls*. Centers for Disease Control and Prevention. https://www.cdc.gov/niosh/hierarchy-of-controls/about/index.html

Occupational Safety and Health Administration. (2002). *Job hazard analysis* (OSHA 3071). U.S. Department of Labor. https://www.osha.gov/sites/default/files/publications/OSHA3071.pdf

Occupational Safety and Health Administration. (n.d.). *Industrial robot systems and industrial robot system safety*. Retrieved October 11, 2026, from https://www.osha.gov/otm/section-4-safety-hazards/chapter-4

Rojas, J., & Hasanzadeh, S. (2025). Human factor in 3D concrete printing for construction. *Proceedings of the Human Factors and Ergonomics Society Annual Meeting, 69*(1), 2160–2162. https://doi.org/10.1177/10711813251357898

Rojas, J., Trout, D., Earnest, G. S., & Hasanzadeh, S. (2026). Occupational safety and health considerations in 3D-printing construction. *Journal of Management in Engineering, 42*(5). https://doi.org/10.1061/JMENEA.MEENG-7383

Sanders, N. E., Şener, E., & Chen, K. B. (2024). Robot-related injuries in the workplace: An analysis of OSHA severe injury reports. *Applied Ergonomics, 121*, 104324. https://doi.org/10.1016/j.apergo.2024.104324

Sari, M., Berawi, M. A., Taswin, W. F., Saroji, G., & Miraj, P. (2025). Work breakdown structure and construction process framework for a hybrid 3D-printed modular building. *Journal of Information Technology in Construction, 30*, 1332–1353. https://doi.org/10.36680/j.itcon.2025.054

Sawicki, B., Düking, P., Placzek, G., Masur, L., Dörrie, R., Schwerdtner, P., & Kloft, H. (2026). Human–robot collaboration in digital fabrication with concrete: Quantifying productivity and psychophysiological strain of human workers. *Construction Robotics, 10*, Article 4. https://doi.org/10.1007/s41693-025-00173-x

Wang, H., Shi, Y., Sun, X., Lin, X., & Ye, Y. (2026). Design, multi-scale structural analysis, and construction of modular prefabricated 3D-printed concrete residence. *Automation in Construction, 182*, 106705. https://doi.org/10.1016/j.autcon.2025.106705

Wang, Q., Han, S., Yang, J., Li, Z., & An, M. (2025). Optimizing printing and rheological parameters for 3D printing with

cementitious materials. *Automation in Construction, 169*, 105881. https://doi.org/10.1016/j.autcon.2024.105881

Wang, Y., Mao, C., Wang, T., & Tao, X. (2026). Enhancing construction safety through hazard-aware human–robot task allocation. *Journal of Management in Engineering, 42*(3), Article 04026002. https://doi.org/10.1061/JMENEA.MEENG-7134

Zhu, J., Cervera, M., & Ren, X. (2024). Buildability of complex 3D-printed concrete geometries using peridynamics. *Automation in Construction, 165*, 105575. https://doi.org/10.1016/j.autcon.2024.105575

Zuo, Y., Guo, B. H. W., Goh, Y. M., & Lim, J.-Y. (2025). Identifying human-robot interaction (HRI) incident archetypes: A system and network analysis of accidents. *Safety Science, 191*, 106959. https://doi.org/10.1016/j.ssci.2025.106959

BÖLÜM 7

Seismic Performance of Retaining Walls: Numerical, Experimental, and Field Evidence

TEOMAN EFEOGLU[1]

Introduction

Retaining walls that have been shaken by earthquakes, scaled models that have been tested in the laboratory and numerical simulations all provide information on how seismic earth pressures develop, and each of them tests the analytical methods from a different side. In this chapter, the numerical, experimental and field studies that make up this evidence are brought together. It is the second part of a review whose first part, on the analytical solutions, is presented in the companion chapter.

The numerical studies reviewed here are finite-element and finite-difference analyses of walls under earthquake loading. Wall flexibility, soil inhomogeneity, foundation compliance and, in some cases, sliding and separation of the soil from the wall are dealt with in them, and several of them compare the computed pressures with those of the Mononobe–Okabe (M–O) method.

[1] Dr., Van Yuzuncu Yil University, Department of Civil Engineering, ORCID: 0009-0006-5561-4941

The physical tests are of two kinds: shaking table tests, in which the model stands in the normal gravitational field, and dynamic centrifuge tests, in which it is subjected to a much higher one. The stresses in the soil are reproduced differently by the two methods, and this affects how their results compare with the analytical solutions.

Field observations show what actually happens to retaining structures in earthquakes. The reported cases range from heavy damage to no damage at all, and the factors that separate them are the type of wall, the quality of construction, groundwater and the presence of loose, liquefiable soil.

The chapter takes these sources in turn: numerical investigations, shaking table and centrifuge tests, and field performance are discussed first, and the evidence is then set against the analytical methods. The chapter is concluded with the limitation that the analytical methods share, which is the neglect of soil–wall separation, and with the research need that follows from it. This chapter is based on the literature review of the author's doctoral thesis (Efeoglu, 2024).

Numerical Investigations

Effects that closed-form solutions cannot include, such as soil inhomogeneity, a flexible wall or foundation, and sliding or separation at the interface, can be considered in numerical analyses. Each of the studies below examines one or more of these effects.

Wood (1973) analysed the flexure of a wall fixed at its base with a finite-element model. The earthquake was applied as static horizontal body forces of intensity $C_o\gamma$, constant over the whole soil layer, where C_o is the acceleration coefficient and γ is the unit weight of the soil. Wood (2019) came back to this problem, building on his earlier work and on that of Veletsos and Younan, and added

tensionless elements along the soil–wall interface as well as a shear modulus that varies with depth.

Wu and Finn (1999) took the shear-beam model of Wu (1994) as their starting point and produced design charts for the seismic thrust on rigid walls. Finite-element analyses were carried out for uniform and non-uniform backfills, with the soil shear modulus taken as uniform, parabolic or linear with depth.

Green et al. (2003) used FLAC to run nonlinear dynamic analyses of a cantilever retaining wall, in order to test how well the M–O method predicts the earth pressure on the wall stem. The computed pressures agreed well with M–O at low accelerations, but they rose above the M–O values as the acceleration increased. In a follow-up study, again with FLAC, Green et al. (2008) found that the load case governing the structural design of the wall is not the one governing its global stability, although the two are usually assumed to coincide in practice.

Gazetas et al. (2004) used finite elements to study three wall types: L-shaped walls of reinforced concrete, pile walls with prestressed anchors and reinforced-soil walls. For the L-shaped walls under high-frequency excitation, sliding and separation of the soil from the wall brought the dynamic pressures below the M–O values. The authors concluded that the good performance often seen in retaining structures during strong earthquakes becomes easier to explain as the analysis gets more realistic, with sliding and separation included.

Ostadan (2005) analysed the soil–structure interaction of building walls with the program SASSI2000. He proposed a simplified procedure, based on a single-degree-of-freedom oscillator, for the maximum seismic soil pressure on the walls of buildings founded on firm material, and the procedure gave results close to the solution of Wood (1973).

Psarropoulos et al. (2005) studied rigid and flexible walls that are not allowed to slide, again with finite elements. Their model first reproduced the solutions of Veletsos and Younan (1997) and Wood (1975), and the authors pointed out that those solutions, like their own, treat the retained soil and the wall as perfectly bonded. They then examined the flexural rigidity of the wall and the rocking compliance of its base. A second soil layer, representing the foundation, took the place of the rotational spring that Veletsos and Younan had put at the base of the wall, and, as with the spring, this lowered the soil pressure. The general finding was that more flexibility in the system always reduces the pressures.

Taken together, these analyses show that flexibility lowers the pressures (Psarropoulos et al., 2005) and that, under high-frequency excitation, sliding and separation can bring them below the M–O values (Gazetas et al., 2004), whereas Green et al. (2003) found pressures above the M–O values at high accelerations. Of the studies above, only Wood (2019) and Gazetas et al. (2004) allow the soil to separate from the wall, and Psarropoulos et al. (2005) state perfect bonding as a limitation of their own model.

Experimental Investigations

Experiments are the other way of checking analytical and numerical results, and they have also shown how soil and structure interact during shaking. Two methods dominate the work on seismic earth pressures against retaining walls and underground structures. In the shaking table test the model stands in the normal gravitational field of the earth, while in the dynamic centrifuge test it is subjected to a much higher gravitational field.

Shaking Table Tests

Mononobe (1929), Matsuo (1941), Matsuo and Ohara (1960), Niwa (1960), Ichihara and Matsuzawa (1973), Sherif et al. (1982), Sherif and Fang (1984) and Matsuzawa and Sugimoto (1984)

are well-known examples of shaking table studies. The first of these is the most cited, because it is the basis of the M–O theory. Only a selection of the later studies is discussed below.

The strength of the shaking table is that any input motion can be applied. Its weaknesses are that the self-weight stresses of the soil cannot be reproduced correctly, and that inertia forces are modelled correctly only if mass is added to the model (Al-Hussaini, 1976; Crewe, 1998; Prasad et al., 2004).

Ishibashi and Fang (1987) tested rigid walls retaining dry cohesionless sand on a shaking table and moved the wall in different ways: by rotating it about its top or its base, by translating it, or by combining these movements. The active pressure distribution depended on the mode. It was non-linear with depth for both kinds of rotation, and the residual stress was high close to the base when the wall rotated about its base and close to the top when it rotated about its top. At low acceleration levels the geometry of the wall displacement controlled the active pressure, whereas at high levels it hardly mattered, because the dynamic inertia force became dominant.

Wilson and Elgamal (2015) carried out ten shaking table tests on a reinforced concrete cantilever wall, with base accelerations between 0.13g and 1.20g, to see how backfill cohesion and very small wall movements affect the size and distribution of the seismic earth pressure. While the backfill acceleration stayed below the yield value, the response was governed by the interaction between wall motion and soil deformation: the backfill was strong enough to prevent an active failure wedge, and the resultant dynamic pressure was nearly zero. Once the yield value was exceeded, the wall moved enough to bring the backfill to the active state, the seismic pressure increased along the whole wall height, and the measured peak pressures were bounded by limit-equilibrium predictions that used

the peak and residual soil strengths. The M–O method, applied with zero cohesion (c = 0), overpredicted the pressures significantly.

Kloukinas et al. (2015) tested scaled cantilever wall models on a compliant base, with different wall geometries and input motions. The walls were made of 32 mm thick aluminium plate, and both the backfill and the foundation were dry silica sand (Leighton Buzzard 14–25). Three model configurations were tested. Embedding the wall toe in the foundation soil always raised the yield acceleration, because it increases the resistance to sliding. Bearing-capacity failure was more sensitive to the level of input acceleration, while sliding depended mainly on the period of shaking, so that the rotational mechanism became the more critical one under strong ground motion. When the wall moved towards the backfill (passive mode), the bending moment at its base increased; when it moved away from the backfill, the displacement grew and the bending moment decreased.

Centrifuge Tests

In a dynamic centrifuge test a reduced-scale model is subjected to a high gravitational acceleration, so that the self-weight of the soil, and with it the confining stress, is close to the prototype values. This is the main advantage over the shaking table. The disadvantage is the very small scale of the models (Al-Hussaini, 1976; Crewe, 1998; Prasad et al., 2004).

Early centrifuge studies include those of Ortiz et al. (1983), Bolton and Steedman (1982, 1985), Zeng (1990), Steedman and Zeng (1991), Stadler (1996), Dewoolkar et al. (2001) and Al Atik and Sitar (2008). Three studies that bear directly on the M–O method are described here.

Ortiz et al. (1983) tested cantilever walls of different stiffness retaining medium-dense fine sand. They developed a shaker that produces earthquake-like motion in the centrifuge, and the payload

of model structure, soil and container was limited to 200 lb at 50 g. The measured earth pressures agreed with the M–O theory, and a linear distribution was accepted as a reasonable average of the actual one, although the measured distributions along the wall were not linear. The influence of wall stiffness on the dynamic response was not explained.

Nakamura (2006) ran a series of dynamic centrifuge tests on gravity walls to study their seismic behaviour and to check the M–O method. He concluded that earth pressures calculated with the M–O theory are not reliable, because its assumptions do not match the way the wall and backfill actually behave. The part of the backfill that followed the wall displacement deformed plastically, in contrast to the rigid wedge of the theory; the pressure distribution on the wall was not triangular and changed with time; and wall and backfill moved with a phase difference, which the theory does not allow.

Al Atik and Sitar (2010), using the centrifuge tests of Al Atik (2008), investigated a stiff and a flexible cantilever wall, each attached to a rigid floor slab. The first test used two sand layers, with the structures on dry medium-dense sand (Dr = 73%) retaining dry medium-dense backfill (Dr = 61%); the second used a single sand of uniform density (Dr = 72%). The dynamic earth pressure increased with depth and could be approximated by a triangular distribution, with its resultant at H/3 above the wall base, as suggested by Mononobe and Matsuo (1932). According to the authors, the M–O theory overestimates the dynamic pressures significantly, because in the tests the maximum dynamic earth pressure and the maximum inertia force on a cantilever wall did not occur at the same time. They also proposed that, for accelerations below 0.4g, the seismic pressure on cantilever walls is small enough to be ignored.

Giarlelis and Mylonakis (2011) reviewed limit-state analysis and the elastic solutions of Arias et al. (1981), Veletsos and Younan (1994a, 1994b, 1997), Veletsos et al. (1995) and Younan and Veletsos

(2000), and compared them with shaking table and centrifuge results. The shaking table results agreed better with the limit-state solutions, and the centrifuge results with the elastic solutions. The authors suggested that the reason is the more accurate representation of the stress state in the centrifuge, since the confining pressure has a strong influence on it.

The choice of test method therefore bears on the conclusions drawn from the test. Table 1 lists the numerical and experimental studies discussed so far.

Table 1: Summary of the numerical and experimental studies reviewed in this chapter.

Study	**Method**	**Subject**	**Main finding**
Wood (1973, 2019)	Finite element	Fixed-base wall under static body forces; later tensionless interface and inhomogeneous soil	Early elastic reference solution; 2019 study adds soil–wall interface and inhomogeneity
Wu & Finn (1999)	Finite element	Rigid walls; uniform, parabolic and linear shear modulus	Design charts for seismic thrust
Green et al. (2003, 2008)	FLAC	Cantilever retaining wall	Pressures agree with M–O at low acceleration and exceed it at high acceleration; structural yield case differs from global stability
Gazetas et al. (2004)	Finite element	L-shaped, anchored pile and reinforced soil walls	Sliding and separation under high-frequency excitation give lower pressures than M–O
Ostadan (2005)	SASSI2000	Building walls on firm material	Simplified oscillator method close to Wood (1973)

Study	Method	Subject	Main finding
Psarropoulos et al. (2005)	Finite element	Rigid and flexible non-sliding walls	Greater system flexibility reduces soil pressures
Ishibashi & Fang (1987)	Shaking table	Dry cohesionless backfill; four wall movement modes	Non-linear pressure distribution; displacement geometry matters at low acceleration, inertia dominates at high
Wilson & Elgamal (2015)	Shaking table (10 tests)	RC cantilever wall; c–ϕ backfill; 0.13g–1.20g	Near-zero pressure below yield acceleration; M–O overpredicts when cohesion is neglected
Kloukinas et al. (2015)	Shaking table	Scaled cantilever walls with compliant base	Yield acceleration increases with toe penetration; rotation more critical under strong motion
Ortiz et al. (1983)	Centrifuge	Cantilever walls in medium-dense fine sand	Agreement with M–O; distribution along the wall not linear
Nakamura (2006)	Centrifuge	Gravity walls	M–O not reliable: plastic backfill deformation, non-triangular and time-varying pressure, phase difference
Al Atik & Sitar (2010)	Centrifuge	Stiff and flexible cantilever walls	Triangular distribution, resultant at H/3; M–O overestimates; pressure negligible below 0.4g
Giarlelis & Mylonakis (2011)	Test comparison	Shaking table and centrifuge results	Shaking table closer to limit-state solutions; centrifuge closer to elastic solutions

Source: Compiled by the author from the studies cited in the table.

Field Performance of Retaining Walls during Earthquakes

Earthquakes are full-scale tests of retaining structures, and the reports written after them give a different kind of evidence from calculations and laboratory models. The reported cases range from

satisfactory behaviour to heavy damage, so the behaviour of a wall cannot be explained by the strength of shaking alone.

After the 1995 Hyogoken-Nambu (Kobe) earthquake, Koseki et al. (1999) checked the external and internal stability of the types of retaining wall affected, with the aim of improving the current pseudo-static, limit-equilibrium design procedure. Many conventional masonry walls and unreinforced concrete gravity-type walls of railway and road embankments were badly damaged. Reinforced concrete (RC) walls and geosynthetic-reinforced soil walls, on the other hand, performed satisfactorily although the estimated peak ground acceleration was as high as 800 cm/s^2. The cases listed by Koseki et al. (1998) include leaning-type unreinforced concrete walls, 500 m long, that broke at ground level; gravity-type unreinforced concrete walls, 400 m long, that tilted strongly, 200 m of them breaking at mid-height and overturning completely; cantilever-type reinforced walls, 200 m long, that cracked at several places at mid-height; and geosynthetic-reinforced soil walls that deformed and moved only slightly.

Lew et al. (1995) documented four temporary prestressed anchored walls in Los Angeles, 10 to 22 m deep, that were shaken by the 1994 Northridge earthquake with ground accelerations of about 0.4g. The shoring had been designed for static loads only, yet the walls moved very little, about 1 cm, and none failed. Failures were examined by Prakash and Wu (1996), who studied two retaining walls that failed in the Kobe and Hokkaido-Nansei-Oki earthquakes to justify the design chart of Prakash et al. (1995) for the sliding and rocking displacements of walls. The failure types described include complete failure, complete overturning, settlement, rotations of up to 3 degrees and outward movements of up to 6 m.

Lew et al. (2010), in a review of the history of seismic earth pressure, noted that although much damage to retaining walls has

been reported, almost all of it concerns poorly built, non-engineered walls or walls that failed through a soil-related failure. Another case of good performance is the temporary retaining structure of the Kerameikos metro station, which was not designed for earthquakes. Gazetas et al. (2004) reported no damage after the mainshock or the aftershocks, although the peak ground acceleration was at least 0.40g.

Sitar et al. (2012) found no case that proves a systemic problem with traditional walls designed for static conditions, even under intense shaking. They also reported that no significant damage or failure of retaining structures occurred in the 2008 Wenchuan earthquake in China, or in the recent great subduction-zone earthquakes in Chile (2010) and Japan (2011).

Seed and Whitman (1970), Gazetas et al. (2004) and Al Atik and Sitar (2008) all stress that the behaviour of a wall in an earthquake depends on the presence of water and of loose, liquefiable soil in the backfill and the foundation. Walls without these conditions have performed well, even when their design did not consider dynamic effects.

Two points follow from these reports. First, damage is concentrated in masonry walls, unreinforced gravity walls and poorly built walls, and in sites with water or liquefiable soil, while engineered walls, including some designed without seismic loading, generally performed well. Second, this good performance is the starting point of the argument of Gazetas et al. (2004), who explain it by sliding and separation. Table 2 lists the cases discussed.

Table 2: Summary of the field observations reviewed in this chapter.

Study	Event or site	Observed performance
Koseki et al. (1999)	1995 Kobe earthquake	Masonry and unreinforced concrete gravity walls severely damaged; RC and geosynthetic-reinforced walls performed satisfactorily (PGA up to 800 cm/s²)
Lew et al. (1995)	1994 Northridge earthquake	Four temporary anchored walls, 10–22 m deep, about 0.4g: movements about 1 cm, no failure
Prakash & Wu (1996)	Kobe and Hokkaido-Nansei-Oki earthquakes	Failure, overturning, settlement, rotation up to 3 degrees, outward movement up to 6 m
Gazetas et al. (2004)	Kerameikos metro station	Temporary structure not designed for earthquakes; PGA at least 0.40g; no damage
Lew et al. (2010)	Review of reported cases	Damage mostly in poorly constructed non-engineered walls or soil-related failures
Sitar et al. (2012)	Wenchuan 2008, Chile 2010, Japan 2011	No significant damage or failure of retaining structures reported

Source: Compiled by the author from the studies cited in the table.

Comparison of Analytical Predictions with Numerical and Experimental Evidence

The studies above can now be compared with the analytical methods reviewed in the companion chapter. The verdict on the Mononobe–Okabe method is not uniform, and it is therefore useful to separate the evidence that supports it from the evidence that questions it.

Some results are consistent with M–O. Ortiz et al. (1983) measured pressures that agreed with the M–O theory, and Green et al. (2003) found good agreement at low accelerations. Giarlelis and Mylonakis (2011) found that shaking table results lie closer to limit-state solutions, of which M–O is the best known, and in the tests of Wilson and Elgamal (2015) the peak dynamic pressures were

bounded by limit-equilibrium predictions, provided that peak and residual soil strengths were used.

Other results are not. Green et al. (2003) found pressures above the M–O values at high accelerations, and Wilson and Elgamal (2015) found that M–O overpredicts the pressure when the backfill cohesion is neglected. Nakamura (2006) judged M–O unreliable, because the rigid wedge, the triangular distribution and the in-phase motion that it assumes were not observed in his tests, and Al Atik and Sitar (2010) found that it overestimates the dynamic pressure, because the peak pressure and the peak inertia force of a cantilever wall do not coincide in time. In the numerical studies, sliding and separation (Gazetas et al., 2004) and a more flexible wall–foundation system (Psarropoulos et al., 2005) lowered the pressures, and the centrifuge results compared by Giarlelis and Mylonakis (2011) were closer to the elastic solutions than to the limit-state ones.

The studies therefore divide into two groups. In the first, which relies mostly on experimental findings, limit-state methods such as M–O are considered adequate for design, whereas in the second, analyses and observations are used to argue that M–O has major shortcomings and may not be appropriate for retaining structures. The field reports do not decide between the groups, because walls designed for static loads have often performed well (Gazetas et al., 2004; Sitar et al., 2012), while the reported damage was largely in non-engineered or poorly built walls (Koseki et al., 1999; Lew et al., 2010).

Part of the disagreement may come from the test method. It was related by Giarlelis and Mylonakis (2011) to how well the stress state of the soil is reproduced in shaking table and centrifuge tests, and it was shown by Ishibashi and Fang (1987) that the way in which the wall moves also changes the pressure distribution. A comparison between a test and an analytical solution should therefore take the

wall movement, the stress state and the soil strength of both into account.

A more basic point is that in both families of analytical solutions the soil is assumed to stay in contact with the wall. Soil–structure interaction is often neglected in this respect by the limit-state and the elastic solutions, and perfect bonding is assumed in the elastic solutions of Veletsos and Younan, which is listed as a limitation by Psarropoulos et al. (2005). Of the numerical studies, only Wood (2019) and Gazetas et al. (2004) allowed the soil to separate from the wall, and pressures below the M–O values were found by Gazetas et al. when separation occurred.

Critical Assessment and Research Needs

The evidence reviewed here leaves a gap. There is still no reliable approach for assessing how soil–wall separation affects the seismic performance of a retaining wall and the distribution of lateral earth pressure on it, and three observations explain why this gap persists.

First, the choice between limit-state and elastic solutions is not settled by the experiments. Different solutions are favoured by shaking table and centrifuge tests (Giarlelis & Mylonakis, 2011), and since the tests differ in wall type, wall movement and soil, neither family of solutions can be taken as general.

Second, the pressures depend on how the wall moves. Different distributions and mechanisms result from rotation about the top or the base, translation, sliding and bearing failure (Ishibashi & Fang, 1987; Kloukinas et al., 2015), and the pressures are lowered by flexible walls or compliant foundations (Psarropoulos et al., 2005). A solution that assumes one mode of movement is therefore less reliable when the real wall moves in another.

Third, the contact between backfill and wall is changed by separation, and the pressure changes with it. Lower pressures than M–O under high-frequency excitation were found in the few studies that included it (Gazetas et al., 2004), but these covered particular walls and motions, and no general relation has been established between separation, soil properties, wall configuration and seismic loading. For static loading, expressions for the resultant force, the height at which it acts and the depth over which the soil separates, all as functions of the base rotation of the wall, were given by the parametric FLAC study of Efeoglu et al. (2021), which is described in the companion chapter.

A practical way forward is parametric numerical analysis, because the wall configuration, soil properties and loading can be varied systematically and the results can be compared with the analytical solutions. A finite difference code such as FLAC is suitable for this purpose, provided that the interface representation, the boundary conditions and the other assumptions are defined carefully and their limits are stated. This is the approach that was followed in the author's doctoral thesis (Efeoglu, 2024).

The main research need is therefore to establish how soil–wall separation affects seismic earth pressures under different soil, wall and loading conditions, and to build this effect into the analytical solutions.

Conclusion

In this chapter, numerical, experimental and field evidence on the seismic behaviour of retaining walls was reviewed. It was shown by the numerical studies that flexibility, interface conditions and soil inhomogeneity change the earth pressures, and the influence of the mode of wall movement, backfill cohesion, acceleration level and the stress conditions of the test was shown by the shaking table and centrifuge tests. According to the field reports, engineered walls

have generally performed well, while poorly built walls, water and liquefiable soils are associated with damage.

The evidence on the M–O method is divided: some tests agree with it, others find it unreliable or conservative, and the outcome depends on the test method as well as on the wall and soil conditions.

One assumption is common to the limit-state and the elastic solutions, which is that the soil stays in contact with the wall. Lower pressures were found in the few numerical studies that relax this assumption, and a general treatment of soil–wall separation is still missing.

Closing this gap requires parametric numerical studies of separation under different soil, wall and loading conditions, followed by simplified relationships that can be used together with the existing analytical solutions.

Disclosure Statement

The author used AI-based tools (ChatGPT and Claude) to assist with language editing, text restructuring and formatting. The author reviewed the revised text and checked the scientific content, including the selection and interpretation of the cited studies.

References

Al Atik, L. (2008). *Experimental and analytical evaluation of seismic earth pressures on cantilever retaining structures* [Doctoral dissertation, University of California, Berkeley].

Al Atik, L., & Sitar, N. (2008). *Experimental and analytical study of the seismic performance of retaining structures* (PEER Report 2008-104). Pacific Earthquake Engineering Research Center, University of California, Berkeley.

Al Atik, L., & Sitar, N. (2010). Seismic earth pressures on cantilever retaining structures. *Journal of Geotechnical and Geoenvironmental Engineering, 136*(10), 1324–1333. https://doi.org/10.1061/(ASCE)GT.1943-5606.0000351

Al-Hussaini, M. M. (1976). *Centrifuge model testing of soils: A literature review.*

Arias, A., Sanchez-Sesma, F. J., & Ovando-Shelley, E. (1981). A simplified elastic model for seismic analysis of earth-retaining structures with limited displacements. In *Proceedings of the International Conference on Recent Advances in Geotechnical Earthquake Engineering and Soil Dynamics* (Vol. 1, pp. 235–240).

Bolton, M. D., & Steedman, R. S. (1982). *Centrifugal testing of microconcrete retaining walls subjected to base shaking.* University of Cambridge, Engineering Department.

Bolton, M. D., & Steedman, R. S. (1985). *The behaviour of fixed cantilever walls subject to lateral shaking.* A. A. Balkema.

Crewe, A. J. (1998). *The characterisation and optimisation of earthquake shaking table performance* [Doctoral dissertation, University of Bristol].

Dewoolkar, M. M., Ko, H.-Y., & Pak, R. Y. S. (2001). Seismic behavior of cantilever retaining walls with liquefiable backfills. *Journal of Geotechnical and Geoenvironmental Engineering, 127*(5), 424–435. https://doi.org/10.1061/(ASCE)1090-0241(2001)127:5(424)

Efeoglu, T. (2024). *Contributions to the static and dynamic analysis of earth retaining structures* [Doctoral dissertation, University of Bristol]. University of Bristol Research Portal.

Efeoglu, T., Karamitros, D. K., & Mylonakis, G. (2021). Effects of soil-wall separation on static earth pressures. In *Proceedings of the 9th Turkish Conference on Earthquake Engineering*.

Gazetas, G., Psarropoulos, P., Anastasopoulos, I., & Gerolymos, N. (2004). Seismic behaviour of flexible retaining systems subjected to short-duration moderately strong excitation. *Soil Dynamics and Earthquake Engineering, 24*(7), 537–550. https://doi.org/10.1016/j.soildyn.2004.02.005

Giarlelis, C., & Mylonakis, G. (2011). Interpretation of dynamic retaining wall model tests in light of elastic and plastic solutions. *Soil Dynamics and Earthquake Engineering, 31*(1), 16–24. https://doi.org/10.1016/j.soildyn.2010.07.002

Green, R. A., Olgun, C. G., & Cameron, W. I. (2008). Response and modeling of cantilever retaining walls subjected to seismic motions. *Computer-Aided Civil and Infrastructure Engineering, 23*(4), 309–322.

Green, R. A., Olgun, C. G., Ebeling, R. M., & Cameron, W. I. (2003). Seismically induced lateral earth pressures on a cantilever retaining wall. In *Advancing mitigation technologies and disaster response for lifeline systems* (pp. 946–955). American Society of Civil Engineers.

Ichihara, M., & Matsuzawa, H. (1973). Earth pressure during earthquake. *Soils and Foundations, 13*(4), 75–86. https://doi.org/10.3208/sandf1972.13.4_75

Ishibashi, I., & Fang, Y.-S. (1987). Dynamic earth pressures with different wall movement modes. *Soils and Foundations, 27*(4), 11–22. https://doi.org/10.3208/sandf1972.27.4_11

Kloukinas, P., Scotto di Santolo, A., Penna, A., Dietz, M. S., Evangelista, A., Simonelli, A. L., Taylor, C., & Mylonakis, G. (2015). Investigation of seismic response of cantilever retaining walls: Limit analysis vs shaking table testing. *Soil Dynamics and Earthquake Engineering, 77*, 432–445. https://doi.org/10.1016/j.soildyn.2015.05.018

Koseki, J., Tateyama, M., Tatsuoka, F., & Horii, K. (1999). Back analyses of soil retaining walls for railway embankments damaged by the 1995 Hyogoken-Nambu earthquake. In *Joint report on 1995 Kobe earthquake* (pp. 31–55). Institute of Industrial Science, University of Tokyo.

Koseki, J., Tatsuoka, F., Munaf, Y., Tateyama, M., & Kojima, K. (1998). A modified procedure to evaluate active earth pressure at high seismic loads. *Soils and Foundations*, 38(Special), 209–216.

Lew, M., Simantob, E., & Hudson, M. B. (1995). Performance of shored earth retaining systems during the January 17, 1994, Northridge earthquake. In *Proceedings of the Third International Conference on Recent Advances in Geotechnical Earthquake Engineering and Soil Dynamics* (Vol. 3, pp. 1417–1422).

Lew, M., Sitar, N., & Al Atik, L. (2010). Seismic earth pressures: Fact or fiction? In *Earth Retention Conference 3* (pp. 656–673). American Society of Civil Engineers. https://doi.org/10.1061/41128(384)66

Matsuo, H. (1941). Experimental study on the distribution of earth pressure acting on a vertical wall during earthquakes. *Journal of the Japan Society of Civil Engineers, 27*(2).

Matsuo, H., & Ohara, S. (1960). Lateral earth pressure and stability of quay walls during earthquakes. In *Proceedings of the Second World Conference on Earthquake Engineering* (Vol. 1, pp. 165–181). Science Council of Japan.

Matsuzawa, H., & Sugimoto, K. (1984). Seismic active earth pressure against elastically supported rigid wall. *Tsuchi-to-Kiso, 32*(6), 32–39.

Mononobe, N. (1929). On determination of earth pressure during earthquake. In *Proceedings of the World Engineering Congress, Tokyo* (Vol. 9, pp. 177–185).

Mononobe, N., & Matsuo, H. (1932). Experimental investigation of lateral earth pressure during earthquakes. *Earthquake Research Institute and Research Office of Public Works, Department of Home Affairs*, 57, 884–902.

Nakamura, S. (2006). Reexamination of Mononobe-Okabe theory of gravity retaining walls using centrifuge model tests. *Soils and Foundations*, 46(2), 135–146. https://doi.org/10.3208/sandf.46.135

Niwa, S. (1960). An experimental study of oscillating earth pressures acting on a quay wall. In *Proceedings of the 2nd World Conference on Earthquake Engineering* (Vol. 1, p. 281).

Ortiz, L. A., Scott, R. F., & Lee, J. (1983). Dynamic centrifuge testing of a cantilever retaining wall. *Earthquake Engineering & Structural Dynamics, 11*(2), 251–268. https://doi.org/10.1002/eqe.4290110207

Ostadan, F. (2005). Seismic soil pressure for building walls: An updated approach. *Soil Dynamics and Earthquake Engineering, 25*(7–10), 785–793. https://doi.org/10.1016/j.soildyn.2004.11.035

Prakash, S., & Wu, Y. (1996). Displacement of rigid retaining walls during earthquakes. In *Proceedings of the 11th World Conference on Earthquake Engineering* (Paper No. 2147).

Prakash, S., Wu, Y., & Rafnsson, E. A. (1995). *Displacement-based aseismic design charts for rigid walls*. Shamsher Prakash Foundation.

Prasad, S. K., Towhata, I., Chandradhara, G. P., & Nanjundaswamy, P. (2004). Shaking table tests in earthquake geotechnical engineering. *Current Science, 87*(10), 1398–1404.

Psarropoulos, P., Klonaris, G., & Gazetas, G. (2005). Seismic earth pressures on rigid and flexible retaining walls. *Soil Dynamics and Earthquake Engineering, 25*(7–10), 795–809.

Seed, H. B., & Whitman, R. V. (1970). Design of earth retaining structures for dynamic loads. In *Proceedings of the ASCE Specialty Conference on Lateral Stresses in the Ground and Design of Earth Retaining Structures* (pp. 103–147).

Sherif, M. A., & Fang, Y.-S. (1984). Dynamic earth pressures on walls rotating about the top. *Soils and Foundations, 24*(4), 109–117. https://doi.org/10.3208/sandf1972.24.4_109

Sherif, M. A., Ishibashi, I., & Lee, C. D. (1982). Earth pressures against rigid retaining walls. *Journal of the Geotechnical Engineering Division, 108*(5), 679–695. https://doi.org/10.1061/AJGEB6.0001288

Sitar, N., Mikola, R. G., & Candia, G. (2012). Seismically induced lateral earth pressures on retaining structures and basement walls. In *Geotechnical engineering state of the art and practice: Keynote lectures from GeoCongress 2012* (pp. 335–358). American Society of Civil Engineers.

Stadler, A. (1996). *Dynamic centrifuge testing of cantilever retaining walls.* University of Colorado at Boulder.

Steedman, R., & Zeng, X. (1991). Centrifuge modeling of the effects of earthquakes on free cantilever walls. In *Centrifuge '91*.

Veletsos, A. S., Parikh, V. H., & Younan, A. H. (1995). Dynamic response of a pair of walls retaining a viscoelastic solid. *Earthquake Engineering & Structural Dynamics, 24*(12), 1567–1589. https://doi.org/10.1002/eqe.4290241203

Veletsos, A. S., & Younan, A. H. (1994a). Dynamic modeling and response of soil-wall systems. *Journal of Geotechnical Engineering, 120*(12), 2155–2179.

Veletsos, A. S., & Younan, A. H. (1994b). Dynamic soil pressures on rigid vertical walls. *Earthquake Engineering & Structural Dynamics, 23*(3), 275–301.

Veletsos, A. S., & Younan, A. H. (1997). Dynamic response of cantilever retaining walls. *Journal of Geotechnical and Geoenvironmental Engineering, 123*(2), 161–172.

Wilson, P., & Elgamal, A. (2015). Shake table lateral earth pressure testing with dense c-ϕ backfill. *Soil Dynamics and Earthquake Engineering, 71*, 13–26. https://doi.org/10.1016/j.soildyn.2014.12.009

Wood, J. H. (1973). *Earthquake-induced soil pressures on structures* [Doctoral dissertation, California Institute of Technology].

Wood, J. H. (1975). Earthquake-induced pressures on a rigid wall structure. *Bulletin of the New Zealand Society for Earthquake Engineering, 8*(3), 175–186. https://doi.org/10.5459/bnzsee.8.3.175-186

Wood, J. H. (2019). Earthquake design of flexible soil-retaining structures. *Proceedings of the Institution of Civil Engineers—Geotechnical Engineering, 172*(1), 30–41.

Wu, G. (1994). *Dynamic soil-structure interaction: Pile foundations and retaining structures* [Doctoral dissertation, University of British Columbia].

Wu, G., & Finn, W. L. (1999). Seismic lateral pressures for design of rigid walls. *Canadian Geotechnical Journal, 36*(3), 509–522.

Younan, A. H., & Veletsos, A. S. (2000). Dynamic response of flexible retaining walls. *Earthquake Engineering & Structural Dynamics, 29*(12), 1815–1844.

Zeng, X. (1990). *Modelling the behaviour of quay walls in earthquakes* [Doctoral dissertation, University of Cambridge].

BÖLÜM 8

Seismic Earth Pressures on Retaining Walls: Analytical and Theoretical Approaches

TEOMAN EFEOGLU[1]

Introduction

In an earthquake, the pressure acting on a retained soil mass is not simply a magnified version of the static pressure; it is governed by the ground motion, the properties of the backfill, the stiffness of the wall, the foundation conditions and, as will be shown in the later sections, the relative movement between the soil and the wall. Static earth pressure solutions that are extended to dynamic loading can therefore provide only an approximate answer, and the accuracy of this answer depends on how well the assumed mechanism represents the real soil–wall system.

The analytical methods that have been developed for this problem can be grouped according to the soil behaviour and the wall movement assumed in them. In the limit-state (limit-equilibrium) methods, of which the Mononobe–Okabe (M–O) method is the best known, the wall is assumed to move sufficiently to bring the backfill to failure, and the earthquake is introduced as inertia forces acting

[1] Dr., Van Yuzuncu Yil University, Department of Civil Engineering, ORCID: 0009-0006-5561-4941

on a Coulomb wedge. In the elastic methods, on the other hand, the backfill is treated as an elastic or viscoelastic continuum, and the pressures are obtained from wave propagation and from the relative motion of soil and wall. The M–O method is simple and is included in design codes, which explains why it is so widely used; however, its assumptions regarding the soil, the wall movement and the rigid wedge become restrictive when the response is governed by soil–structure interaction.

Many studies have attempted to relax these assumptions. Some of them extend the limit-state theory to cohesive soils, to intermediate wall displacements, and to curved failure surfaces or stress-field solutions, whereas others, which are based on elastic wave theory, include wall flexibility, foundation compliance and soil stiffness varying with depth. Each formulation addresses a different part of the problem, and the assumption it makes about the soil–wall interface is as important as the equations themselves.

In this chapter, the main analytical solutions are reviewed in that order. The M–O method and its extensions are presented first, followed by the simplification of Seed and Whitman (1970), the intermediate-movement solution of Zhang et al. (1998a, 1998b) and the plasticity-based solutions of Lancellotta (2002, 2007) and Mylonakis et al. (2007). The elastic and elastodynamic solutions are discussed next, including the kinematic approach of Brandenberg et al. and the solution of Vrettos et al. (2016) for inhomogeneous soil. The chapter is concluded with a comparison of the methods and with the limitation that most of them share, which is the assumption of continuous contact between soil and wall. The numerical, experimental and field studies are covered in the companion chapter. This chapter is based on the literature review of the author's doctoral thesis (Efeoglu, 2024).

Limit-Equilibrium Methods

The limit-equilibrium approach is the most widely used way of estimating seismic earth pressures on retaining walls. The Mononobe–Okabe (M–O) method extends Coulomb's (1776) wedge theory to earthquake loading (Kramer, 1996). The inertia forces caused by the earthquake are added to the forces acting on the soil wedge behind the wall, namely its weight, the reaction along the failure plane and the reaction of the wall. Solving the equilibrium of these forces gives the active and the passive seismic thrust on the wall.

The method originates from the Kanto earthquake of 1 September 1923. Mononobe and Matsuo carried out a series of shaking table tests after the earthquake (Mononobe, 1929; Mononobe & Matsuo, 1932), and these results, together with the analysis of Okabe (1924, 1926), laid the foundation of the M–O theory. The theory combines quasi-static inertia forces with the static Coulomb wedge. Because the equations are easy to understand and to apply, the method has been adopted by many design standards, such as Eurocode 8 (European Committee for Standardization [CEN], 2004) and NCHRP Report 611 (Anderson, 2008).

The theory rests on three assumptions. First, the soil is cohesionless, isotropic and homogeneous, it behaves elastically and it has a constant friction angle. Second, the wall yields enough to mobilise the full strength along the failure plane, so that a soil wedge forms and separates from the rest of the backfill. Third, the wedge moves as a rigid body, and every point of it has the same constant acceleration, equal to that at the base of the wall. The earthquake enters the analysis only through pseudo-static horizontal and vertical forces, which are the weight of the wedge multiplied by the seismic coefficients k_h and k_v.

Figures 1 and 2 show the forces on the soil wedge for the active and the passive case. In addition to the static forces, the wedge carries pseudo-static forces, which are proportional to its mass and

to the pseudo-static accelerations (a_h and a_v). For the active case, the total seismic thrust at the failure state follows from the equilibrium of the weight of the wedge (W), the earthquake-induced forces (k_hW and k_vW), the force F exerted by the soil below the wedge and the force P exerted by the wall. It is given in Equation (1). The coefficient K_{ae} in Equation (2) depends on the friction angle of the soil, the friction at the soil–wall interface, the inclination of the backfill and of the wall, and the seismic coefficients.

$$P_{ae} = \frac{1}{2} K_{ae} \gamma H^2 (1 - k_v) \tag{1}$$

where,

K_{ae}: seismic active earth pressure coefficient, Equation (2)

k_v: the ratio between vertical seismic acceleration (a_v) and gravity acceleration (g)

k_h: the ratio between horizontal seismic acceleration (a_h) and gravity acceleration (g)

$$K_{ae} = \frac{\cos^2(\phi - \theta - \psi)}{\cos\psi \cos^2\theta \cos(\delta + \theta + \psi)\left[1 + \sqrt{\frac{\sin(\delta + \phi)\sin(\phi - \beta - \psi)}{\cos(\delta + \theta + \psi)\cos(\beta - \theta)}}\right]^2} \tag{2}$$

where

$\phi - \beta \geq \psi$ and $\psi = \tan^{-1}\left(\frac{k_h}{1 - k_v}\right)$.

ϕ: friction angle of the soil

δ: friction angle of the soil-wall interface

β: inclination angle of backfill

θ: inclination angle of the wall

ψ: angle of the resultant body force

The passive case is formulated in the same way. The seismic passive thrust is given by Equation (3) and the corresponding coefficient by Equation (4).

$$P_{pe} = \frac{1}{2} K_{pe} \gamma H^2 (1 - k_v) \tag{3}$$

where K_{pe} is the seismic passive earth pressure coefficient, Equation (4).

$$K_{pe} = \frac{\cos^2(\phi + \theta - \psi)}{\cos\psi \cos^2\theta \cos(\delta - \theta + \psi)\left[1 - \sqrt{\frac{\sin(\delta + \phi)\sin(\phi + \beta - \psi)}{\cos(\delta - \theta + \psi)\cos(\beta - \theta)}}\right]^2} \tag{4}$$

The difficult part of the M–O procedure is the choice of the horizontal seismic coefficient, and the PGA is usually recommended for it. Wagner and Sitar (2018), however, demonstrated that the limit-equilibrium solutions overestimate the pressures that actually develop when the surface PGA is used as the input acceleration.

Figure 1: Forces acting on the soil wedge in the Mononobe–Okabe active case.

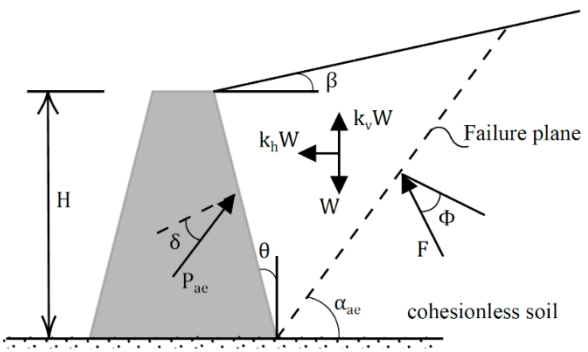
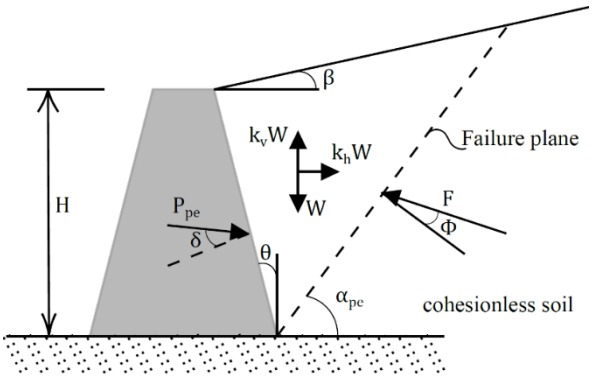


Figure 2: Forces acting on the soil wedge in the Mononobe–Okabe passive case.



A different route is the sliding-block method of Newmark (1965). Instead of taking the PGA as the main design criterion, it starts from the critical (yield) acceleration of the system and bases the design on an allowable displacement. The structure is thus allowed to move by a controlled amount during the earthquake, which makes a performance-based design possible and can give a more economical solution without compromising safety (Kramer, 1996).

Vertical seismic loading has traditionally received little attention. Anderson (2008) explains that the vertical acceleration has a higher frequency and is out of phase with the horizontal one, so its influence on the wall pressure can be positive or negative, and leaving it out of the design has been considered reasonable.

Without an earthquake ($\psi = 0$), K_{ae} reduces to K_a, Coulomb's active earth pressure coefficient, and the dynamic increment is the difference between the seismic and the static thrust (Equation 5). The static thrust and the increment do not act at the same point, which comes out repeatedly in the studies reviewed below. The total thrust alone therefore says little about the pressure distribution and the overturning moment on the wall.

$$\Delta P_{ae} = P_{ae} - P_a = \frac{1}{2}\gamma H^2 (K_{ae} - K_a) \quad (5)$$

The M–O method nevertheless has clear limits. It treats the backfill as a homogeneous cohesionless wedge, so cohesive soils are outside its scope, and its pseudo-static loading says nothing about how the wall and the soil interact during shaking. The extensions and alternatives in the next sections respond to these limits.

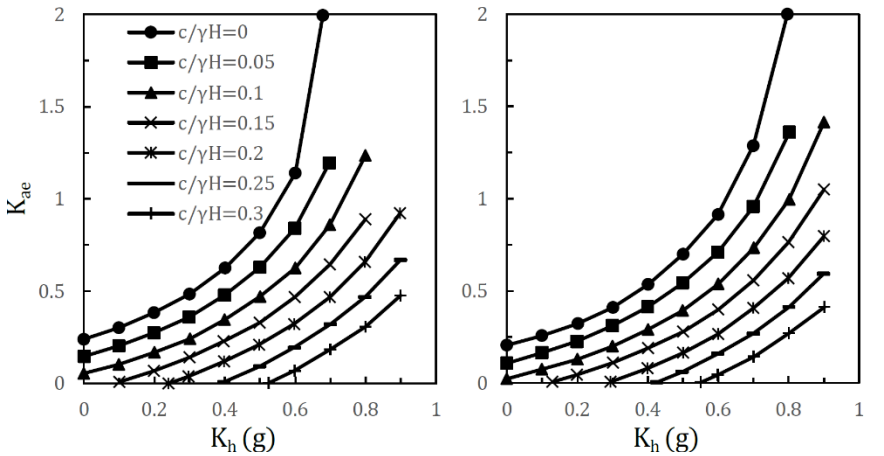
Extensions of the Mononobe–Okabe Method

Treating the backfill as a homogeneous cohesionless material is the most obvious weakness of the M–O equations, and the first extensions were aimed at it.

Prakash and Saran (1966) extended the equations to c–ϕ soils and also dealt with tension cracks and wall adhesion. Comparable solutions were given or discussed by Richards and Shi (1994), Das and Puri (1996) and Chen and Liu (2012).

The effect of cohesion is shown in Figure 3 for horizontal backfill, without tension cracks and wall adhesion, and for two friction angles ($\phi = 35°$ and $\phi = 40°$). Each chart gives K_{ae} as a function of the horizontal seismic coefficient k_h for cohesion values $c/\gamma H$ between 0 and 0.3, where c is the cohesion, γ the unit weight of the soil and H the wall height. The coefficient decreases as $c/\gamma H$ increases, and for the larger cohesion values it is zero over the lower range of k_h. With the help of these charts, Anderson (2008) gave an example in which a small cohesion lowers the dynamic active earth pressure by about 50–75% in typical design cases.

Figure 3: Seismic active earth pressure coefficient K_{ae} for c–ϕ soils with horizontal backfill: ϕ = 35° (left) and ϕ = 40° (right).



The same discussion argues that, for many combinations of small seismic coefficients and short walls, even a low cohesion means that the soil has enough shear strength to carry the inertial loading, so that the wall experiences no additional pressure during the earthquake. This may help to explain the good performance of retaining walls in earthquakes. The charts should not be read as proof that cohesion removes the seismic pressure in every wall, though. They show how sensitive the computed pressure is to the strength assumed for the soil.

The M–O method has a second limitation, which concerns equilibrium. It satisfies the translational equilibrium of the wedge only. Rotational equilibrium would require all the forces to meet at a single point, but the method does not tell where exactly the resultant of the soil reaction (F) acts, nor where the load (P) is applied. It also leaves out the movement of the wall base (rotation or sliding) during the earthquake, which can change the magnitude and the distribution of the pressure considerably.

Seed and Whitman (1970) closed part of this gap by recommending that the additional seismic pressure (ΔP) acts at 0.6 times the wall height. This makes it possible to satisfy both translational and rotational equilibrium. Their approach is described in the next section.

The Seed and Whitman (1970) Approach

Seed and Whitman (1970) prepared a comprehensive document on the design of earth-retaining structures against dynamic loads. They investigated the effects of the friction angle, the backfill inclination, the wall friction, the type of wall (walls above the water table and waterfront structures), the type of load (seismic and blast) and the vertical and horizontal accelerations.

They modified the M–O formula by writing the maximum dynamic active pressure as a static pressure plus a dynamic increment (Equation 6). The increment was simplified to 75% of the horizontal acceleration coefficient, and the vertical acceleration was ignored (Equation 7).

$$P_{ae} = P_a + \Delta P_{ae} \tag{6}$$

$$P_{ae} = \frac{1}{2}\gamma H^2 \left(K_a + \frac{3}{4}k_h\right) \tag{7}$$

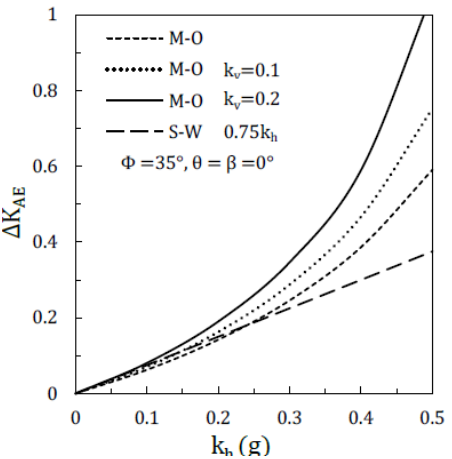
Here P_{ae} is the total active thrust under seismic loading, P_a the static active thrust and ΔP_{ae} the seismic increment; γ is the unit weight of the soil and H the wall height. K_a is the static active earth pressure coefficient and k_h the horizontal seismic coefficient. In this simplified form the seismic increment is represented by the term $3k_h/4$ in Equation (7).

According to Seed and Whitman (1970), the increase in lateral pressure caused by base shaking is concentrated in the upper part of the wall, and the resultant of the additional active thrust acts

between 0.5H and 0.67H above the wall base, where H is the wall height. Since the static thrust of a triangular pressure distribution acts at H/3, the point of application of the total thrust moves upwards as the seismic increment grows.

Figure 4 compares the dynamic increment ΔK_{AE} of the M–O theory, without vertical acceleration and with $k_v = 0.1$ and 0.2, with the simplified expression of Seed and Whitman (1970) for $\phi = 35°$ and $\theta = \beta = 0°$. The two agree closely up to k_h of about 0.2. Beyond this value the M–O increment grows faster and depends increasingly on k_v, so the simplified expression gives clearly lower values at high accelerations. The choice of method therefore changes the design pressure mainly in strong shaking.

Figure 4: Dynamic increment of the earth pressure coefficient from the Mononobe–Okabe method (without vertical acceleration and with $k_v = 0.1$ and 0.2) and from the Seed–Whitman expression ($\phi = 35°$, $\theta = \beta = 0°$).



The attraction of the Seed and Whitman procedure is that the seismic increment can be estimated without evaluating the full M–O equation in every case. Because the increment is a fixed fraction of k_h, however, it does not depend on the friction angle of the soil and

it ignores the vertical acceleration. The difference from the M–O result in Figure 4 shows what this simplicity costs.

Earth Pressures under Intermediate Wall Movement

Zhang et al. (1998a, 1998b) derived analytical expressions for earth pressures on walls that undergo any lateral displacement. In the second paper (Zhang et al., 1998b) the seismic pressure between the active and the passive state, including the neutral state in which the wall does not move, is investigated, and equations are given for its distribution, resultant and point of application. They apply to cases where the wall displacement is too small to mobilise the full shear strength of the soil.

To describe these cases, an intermediate soil wedge is proposed, whose dimensions change with the amount of wall displacement and with the seismic acceleration. The total seismic pressure is divided into four parts: the weight of the effective soil wedge, the seismic inertia force, the surcharge on the backfill surface, and the vibro-densification of the soil near the neutral state. Every part has its own height of application and its own distribution with depth.

Wall displacement therefore matters for the seismic pressure. The limit-state solutions deal only with the fully active or passive state, which are just the two end points of the possible wall movements.

Solutions Based on Plasticity

Wall friction complicates the limit-state solutions. When it is present, the stress field in the backfill is not uniform and the failure surface is not a plane, as the M–O wedge assumes. The effect is largest for the passive resistance.

Lancellotta (2002, 2007) points out that, with wall friction, the M–O approach to seismic earth pressures becomes more

complex because of the non-uniform stress field and the non-planar failure surfaces, particularly for the passive resistance. Reference tables such as those of Caquot and Kérisel (1948) and Absi (2017) rely on limit-equilibrium solutions with a curved failure surface, typically a logarithmic spiral. These solutions are commonly applied, but they are kinematic and give upper-bound estimates rather than exact solutions.

Lancellotta argues that force-based approaches (Steedman & Zeng, 1990; Zeng & Steedman, 1993) are still debated, but their wide adoption justifies further work on solutions built on statically admissible stress fields, which are more conservative or more precise. He therefore developed an analytical solution for the seismic passive resistance coefficient on the basis of the lower-bound theorem of plasticity (Equations 8 to 11). The key step is a transformation of axes, which allows the seismic passive resistance to be calculated with the same equations as in the static case.

The solution gives the normal component of the passive resistance (Equation 8) through the coefficient K_{PE} (Equation 9), the angle θ (Equation 10) and the obliquity ψ of the body force (Equation 11).

$$\sigma'_{xx} = K_{PE}\overline{\gamma}\zeta\cos(i-\psi) \tag{8}$$

where

$$K_{PE} = \left[\frac{\cos\delta}{\cos(i-\psi)-\sqrt{\sin^2\phi' - \sin^2(i-\psi)}}\left(\cos\delta + \sqrt{\sin^2\phi' - \sin^2\delta}\right)\right] e^{2\theta\tan\phi'} \tag{9}$$

and

$$2\theta = \sin^{-1}\left(\frac{\sin\delta}{\sin\phi'}\right) + \sin^{-1}\left(\frac{\sin(i-\psi)}{\sin\phi'}\right) + \delta + (i-\psi) + 2\psi \tag{10}$$

σ'_{xx}: normal component of the passive earth resistance

i: slope of backfill

k_h: coefficient of horizontal acceleration

k_v: coefficient of vertical acceleration

$\overline{\gamma}$: effective unit weight

ζ: depth coordinate

δ: friction angle at soil/wall interface

θ: angle of rotation of the principal stress direction

ϕ': angle of internal friction

ψ: inclination of the body force per unit volume when the earthquake acts

where

$$\psi = \tan^{-1}\left(\frac{k_h}{1 - k_v}\right) \tag{11}$$

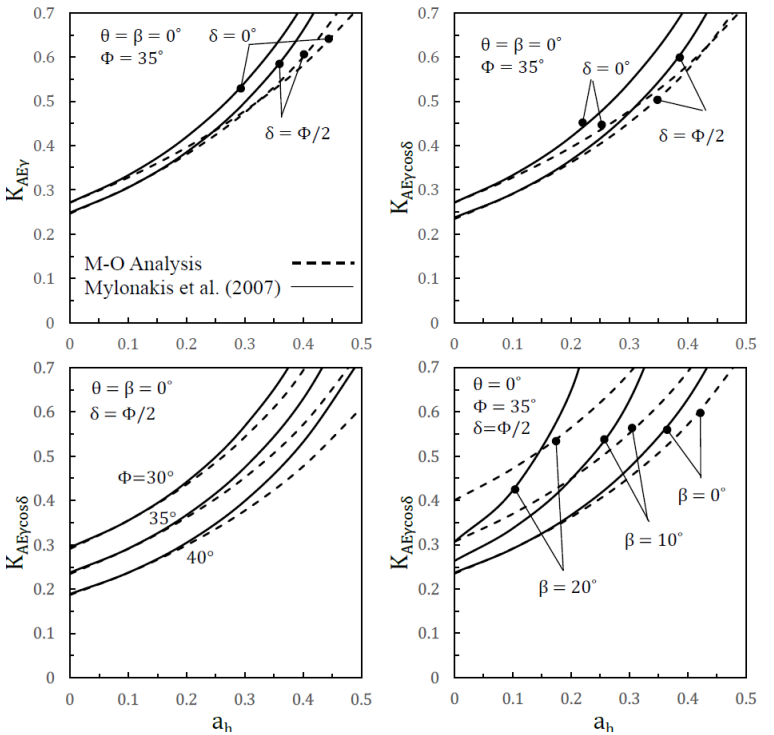
The solution is an alternative to the formulations based only on force equilibrium and an assumed failure wedge. By using a statically admissible stress field, it gives a safe-side estimate of the passive resistance under seismic loading. It also shows that the theoretical framework chosen at the start of the derivation affects the seismic earth pressure coefficients.

Mylonakis et al. (2007) offered an alternative to the M–O method in the form of a stress-plasticity solution for static and earthquake-induced pressures on gravity retaining walls. Their closed-form expression is symmetric: with the proper signs for wall roughness and soil friction angle, a single equation covers both the active and the passive state. The solution is on the safe side, because

the active pressures are overestimated and the passive resistance is underestimated.

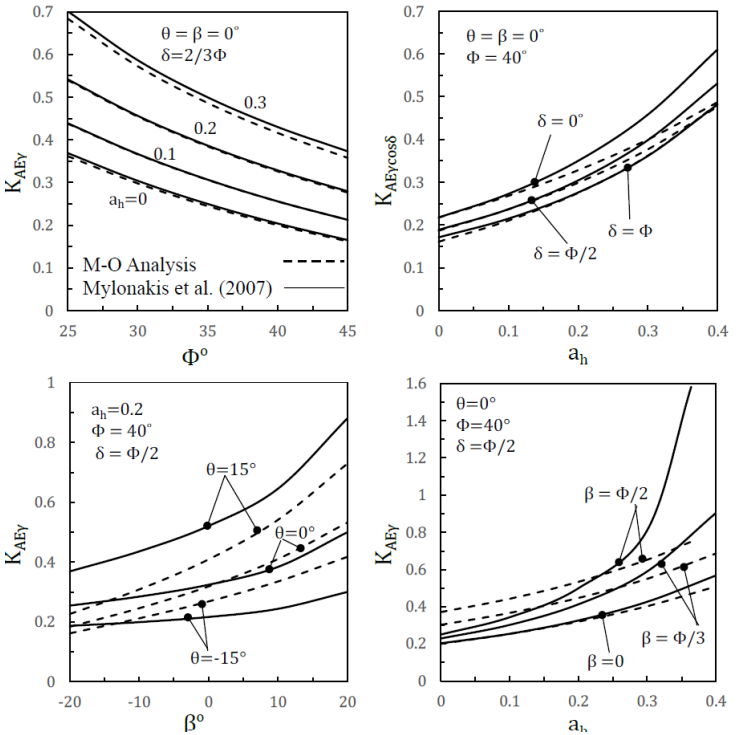
Figures 5 and 6 compare the active pressure coefficients of this solution with those of the M–O method. In both solutions the active pressure increases with the seismic acceleration and the slope of the backfill, and it decreases when the soil friction angle or the wall roughness increases. For horizontal backfill the two solutions are close. The differences appear mainly for inclined backfill and at high accelerations.

Figure 5: Comparison of active seismic earth pressure coefficients obtained using the Mylonakis et al. (2007) and Mononobe–Okabe methods for different soil and wall parameters.



Source: Adapted from Mylonakis et al. (2007).

Figure 6: Influence of soil friction angle, wall friction, backfill inclination, and horizontal seismic acceleration on active seismic earth pressure coefficients.



Source: Adapted from Mylonakis et al. (2007).

Elastic and Elastodynamic Methods

The second group of analytical methods consists of linear elastic closed-form solutions. Their main advantage is that they take elastic wave propagation and the relative motion between soil and structure into account, and their results can be compared with experiments (Wagner & Sitar, 2018).

In these solutions the retained soil is treated as an elastic or viscoelastic continuum, represented by shear beams or springs, while the wall is rigid or flexible depending on the model. Because the

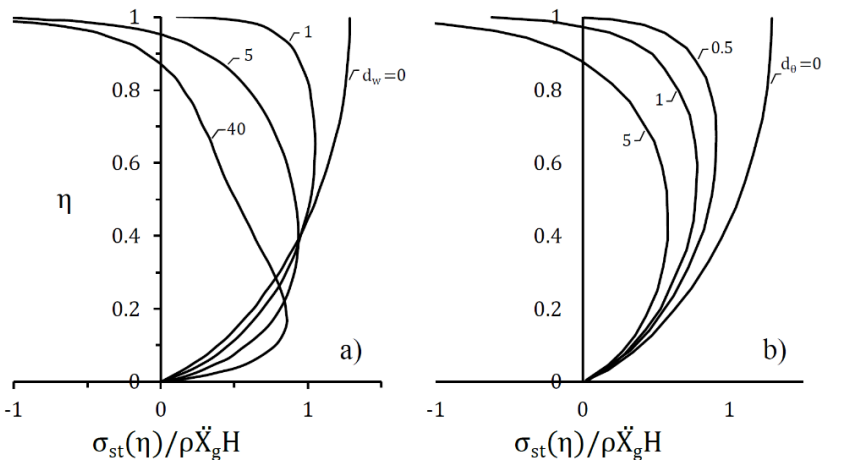
wall, the soil and the foundation interact, the flexibility of the wall and the rotation of its base start to control the pressures, which the limit-state methods cannot represent.

Veletsos and Younan (1994a) obtained an expression for the dynamic pressures and forces that ground shaking induces on a vertical rigid wall retaining a uniform viscoelastic soil. They also evaluated the accuracy of a simplified model proposed by Scott (1973), in which the soil is a shear beam coupled to the wall by springs. The spring stiffness per unit wall length is given by Equation (12).

$$k_s = \frac{0.8(1-\nu)}{1-2\nu}\frac{G}{H} \tag{12}$$

Here k_s is the spring stiffness per unit wall length, G the shear modulus of the soil, H the wall height and ν the Poisson's ratio of the soil.

Figure 7: Distribution of wall pressure for statically excited systems with different wall and base flexibilities.



Source: Adapted from Veletsos and Younan (1997).

Veletsos and Younan (1994a) found that Scott's model leaves out the radiation damping of the medium and makes the wall pressure proportional to the relative displacement between the wall and the far-field soil. As a result, it does not capture the behaviour of the system well and may lead to significant discrepancies in the predictions. The rationale and the accuracy of Equation (12) are also unclear, and since the wall forces are proportional to k_s, any error in this stiffness passes directly to the results. Moreover, k_s, and with it the wall pressures and forces, becomes infinite as ν approaches 0.5, which is not realistic.

In later studies, Veletsos and Younan (1994b, 1997) and Younan and Veletsos (2000) examined the effect of rotating rigid walls and of wall flexibility. The soil was a semi-infinite, uniform viscoelastic layer described by its density ρ, shear modulus G, Poisson's ratio ν and damping factor δ. The wall was described by its thickness t_w, mass per unit surface area μ_w, Young's modulus E_w, Poisson's ratio ν_w and damping factor δ_w.

Two assumptions were made: no vertical stress develops in the soil when it is excited horizontally, and the wall and the soil are completely bonded. The response is governed by two parameters: the flexibility of the wall relative to the retained soil, d_w (Equation 13), and the flexibility of the rotational base constraint relative to the soil, d_θ (Equation 15). Figure 7 shows how the pressure on a statically excited wall changes with each of them. As the flexibility increases, the pressure decreases and its distribution changes, and in the more flexible cases the computed pressure becomes negative, that is tensile, over part of the wall height.

The two flexibility parameters are defined as follows.

$$d_w = GH^3/D_w \tag{13}$$

where D_w is the flexural rigidity per unit length of the wall, and R_θ in Equation (15) is the rotational stiffness of the base constraint:

$$D_w = \frac{E_w t_w^3}{12(1-\nu_w^2)} \tag{14}$$

$$d_\theta = GH^2/R_\theta \tag{15}$$

Veletsos and Younan (1994b, 1997) showed that wall flexibility and the rotational compliance of the foundation control the dynamic earth pressures, so ignoring them may lead to significantly overestimated or underestimated seismic pressures. Finite-element analyses by Wu and Finn (1999) and Psarropoulos et al. (2005) confirmed these results. In addition, Wu and Finn (1999) examined uniform, parabolic and linear profiles of the shear modulus, and Psarropoulos et al. (2005) looked into the flexural rigidity of the wall and the rocking compliance of the base.

These solutions share the assumption that the wall and the soil remain perfectly bonded. They therefore cannot represent a soil that separates from the wall, and this is where they are limited.

Kloukinas et al. (2012) proposed a simple elastodynamic solution in which the horizontal displacement of the backfill follows a shape function over depth. Being in closed form, it is easier to use in practice than the more complex solution of Veletsos and Younan.

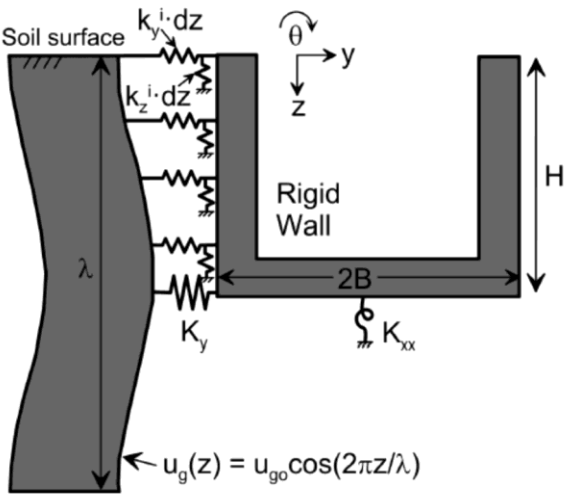
The model consists of a linear viscoelastic soil with a rigid wall and base. A rotationally constrained wall is also included to represent the compliance of the foundation. Wall flexibility, on the other hand, is not considered.

Kinematic Approaches to Seismic Earth Pressures

Brandenberg et al. (2015) proposed a conceptual framework that rests on soil–structure interaction and wave propagation and defines the seismic earth pressures on retaining structures. One of its

aims was to clarify the confusion caused by the conflicting results of the limit-equilibrium and the elastic methods. Seismic pressures are regarded as loads imposed on the system, and kinematic interaction enters through the ratio of the wavelength of the vertically propagating shear waves to the wall height. In contrast to the pseudo-static methods, the pressure does not come from an equivalent inertia force but from the incompatibility between the displacements of the wall and of the soil.

Figure 8: Schematic representation of an embedded rigid strip foundation subjected to vertically propagating shear waves.



Source: Adapted from Brandenberg et al. (2015).

Figure 8 shows the model, which relies on the spring coefficients of Kloukinas et al. (2012): the stiffness intensities k_y^i and k_z^i represent the interaction between soil and wall, and the stiffness terms K_y and K_{xx} represent the interaction between the soil and the base of the wall. Horizontally coherent shear waves propagate vertically through the soil, and the contact between soil and wall is perfect, so no gap opens at the interface. The difference

between the displacement of the rigid wall, $u_w(z)$, and that of the free-field soil column, $u_g(z)$, produces the kinematic pressures. Their resultant force and moment are given by Equations (16) and (17):

$$P_E = \int_0^H k_y^i \left[u_{g0} \cos k\,z - u_w(z)\right] dz \tag{16}$$

$$M_E = \int_0^H k_y^i (H - z) \left[u_{g0} \cos k\,z - u_w(z)\right] dz \tag{17}$$

where,

$$u_w(z) = u_{FIM} + \theta_{FIM}(H - z)$$

$$u_g(z) = u_{g0} \cos\left(\frac{2\pi z}{\lambda}\right)$$

and,

k_y^i: horizontal wall-soil stiffness intensity

k : wave number of shear waves in the soil

λ : wavelength of the shear wave propagating vertically through the soil

u_{FIM} : base slab translation (FIM, foundation input motion)

θ_{FIM} : base slab rotation

If the wall is rigid and rests on a rigid base, the base rotation vanishes $\theta_{FIM} = 0$ and the base translation is equal to the free-field displacement at the base of the wall, so that

$$u_{FIM} = u_{g0}\, cos(kH)$$

Brandenberg et al. (2017) extended the method to vertically inhomogeneous soil and obtained approximate solutions by simplifying the stress and displacement fields in the vertical

direction. This is relevant to natural soil deposits, where the shear modulus is not constant with depth.

Brandenberg et al. (2020) took the approach further. The wall is no longer assumed to be rigid and massless, and the soil is modelled with a shear wave velocity that varies with depth, in a Winkler-type solution for flexible walls. The model was validated by comparison with several closed-form solutions and with the experimental data of Hushmand et al. (2016).

Durante et al. (2022) then proposed a simplified version of this solution. According to the authors, the equations of Brandenberg et al. (2020) require more implementation effort than the M–O methods currently used in practice, and the aim was a simpler model. The proposed model does not account for soil–wall separation, but it still captures the main mechanisms of kinematic seismic earth pressures, considering the frequency of the input motion, the soil stiffness, the wall flexibility and the wall dimensions.

Together, these studies change the question from “how large is the inertia force?” to “how much do the wall and the soil move relative to each other?”. In the model of Brandenberg et al. (2015) and in the simplified solution of Durante et al. (2022), the soil is assumed to stay in contact with the wall.

The NEHRP Recommended Seismic Provisions (Building Seismic Safety Council [BSSC], 2020) follow this line of research. They state that the framework behind the M–O method ties the seismic soil pressure to acceleration instead of to the relative displacement between wall and soil. BSSC (2020) considers this assumption incorrect, because there is no underlying connection between the surface acceleration and the seismic earth pressure. Even if the backfill is shaken by strong accelerations, no appreciable pressure develops when the wall and the backfill move in phase with similar amplitudes.

Pseudo-acceleration (M–O type) methods are therefore regarded as not representing the physics of the problem. BSSC (2020) recommends the soil–structure interaction method of Brandenberg et al. (2015, 2017), which it presents in detail, and states that, compared with observations, this method gives much better results than the M–O method.

The two families of methods can therefore be regarded as complementary. The M–O method is simple and has a long record in practice, whereas the kinematic and elastodynamic solutions provide additional insight in cases where wall flexibility, soil inhomogeneity and the relative movement of wall and backfill are important. The latter also depend on modelling assumptions, one of which is whether soil–wall separation is allowed.

Seismic Pressures on Walls Retaining Inhomogeneous Soil

Vrettos et al. (2016) analysed the seismic pressures on two rigid cantilever walls that support an elastic soil whose stiffness changes continuously with depth. In contrast to the solutions that assume uniform soil properties, the shear modulus varies with depth.

The shear modulus is an exponential function of depth (Equation 18), following the earlier study of Vrettos (2013). The solution combines the procedure of Papazafeiropoulos and Psarropoulos (2010) with earlier work of the authors.

$$G(z) = G_o + (G_\infty - G_o)(1 - e^{-\alpha z}) \qquad (18)$$

G_o: shear modulus at the surface

G_∞: shear modulus at infinite depth

α: non-homogeneity gradient

Taking inhomogeneity into account matters because the stiffness profile controls wave propagation and soil–structure interaction. A uniform shear modulus may not represent walls

founded in deposits whose stiffness changes with depth, and the solution of Vrettos et al. (2016) addresses this point. Its own assumptions are an elastic soil and rigid cantilever walls.

Comparison and Limitations of the Analytical Approaches

The analytical approaches reviewed in this chapter progress from the limit-state methods towards formulations that include wall movement, soil–structure interaction, wall flexibility and soil inhomogeneity, and each of them is tied to its own assumptions. Table 1 summarizes these approaches with their main assumptions and the limitations reported in the literature.

Table 1: Summary of the analytical approaches reviewed in this chapter.

Study	Approach	Main assumptions	Reported limitation or note
Mononobe–Okabe (Mononobe, 1929; Okabe, 1924, 1926)	Pseudo-static limit equilibrium; Coulomb wedge with seismic inertia forces	Cohesionless, homogeneous backfill; wall yields enough for a limit state; rigid wedge	Only translational equilibrium; point of application not given; cohesion not included
Prakash & Saran (1966); Richards & Shi (1994); Das & Puri (1996); Chen & Liu (2012)	M–O extended to c–ϕ soils, tension cracks and wall adhesion	Limit state with a planar failure wedge	Small cohesion can reduce the dynamic active pressure by about 50–75% (Anderson, 2008)
Seed & Whitman (1970)	Simplified M–O: static thrust plus a dynamic increment	Increment taken as 3/4 of the horizontal coefficient; vertical acceleration ignored; resultant at about 0.6H (0.5H–0.67H)	Simplified; depends on the assumed seismic coefficient

Study	Approach	Main assumptions	Reported limitation or note
Zhang et al. (1998a, 1998b)	Earth pressure for any lateral wall displacement, including the neutral state	Intermediate soil wedge; strength only partly mobilised; four pressure components	Distribution depends on the assumed movement mechanism
Lancellotta (2002, 2007)	Lower-bound plasticity for seismic passive resistance	Statically admissible stress field; wall friction; transformation of axes	Alternative to kinematic (upper-bound) log-spiral solutions
Mylonakis et al. (2007)	Closed-form stress-plasticity solution for gravity walls	One equation for active and passive cases; wall roughness included	On the safe side: overestimates active and underestimates passive pressures
Veletsos & Younan (1994a, 1994b, 1997); Younan & Veletsos (2000)	Elastic (viscoelastic) wave solutions for rigid and flexible walls	Uniform semi-infinite viscoelastic soil; wall flexibility and base rotation considered	Perfect bonding between wall and soil assumed
Kloukinas et al. (2012)	Simple elastodynamic solution with a shape function	Linear viscoelastic soil; rigid wall; rotational constraint at the base	Wall flexibility not considered
Brandenberg et al. (2015, 2017, 2020); Durante et al. (2022)	Kinematic soil–structure interaction based on relative soil–wall displacement	Vertically propagating shear waves; inhomogeneous soil; flexible wall (2020); simplified form (2022)	Soil–wall separation not included
Vrettos et al. (2016)	Analytical solution for inhomogeneous elastic soil	Two rigid cantilever walls; shear modulus increasing exponentially with depth	Elastic soil and rigid walls assumed

Source: Compiled by the author from the studies cited in the table.

A limitation that is shared by most of the limit-state and elastic solutions is that the soil is assumed to stay in contact with the wall. When the wall moves away from the soil, the interface cannot carry tension and the soil separates from the wall, which changes both the distribution and the magnitude of the earth pressure.

The effect of separation has been examined numerically by Efeoglu et al. (2021), who carried out a parametric study with the finite-difference code FLAC on smooth rigid walls on a flexible foundation retaining a soil with a shear modulus that varies with depth. The study is described in the companion chapter.

No single analytical method is suitable for every seismic retaining-wall problem. The limit-state methods are intended for walls that move enough for the backfill to reach failure, the elastic and kinematic solutions assume an elastic response of the soil, and the solution of Zhang et al. covers the range in between. The choice of method therefore depends on the expected wall movement, the soil properties, the foundation conditions, the wall flexibility and the possibility of separation, and where these conditions fall outside the assumptions of the method, numerical or experimental evidence is required to support the analytical result.

Conclusion

The analytical methods reviewed here constitute the basis for the assessment and design of retaining walls under earthquake loading. The Mononobe–Okabe method remains the most practical tool, since its formulation is simple and it extends Coulomb's wedge theory to seismic conditions; however, its assumptions regarding the soil, the failure mechanism and the wall movement limit its use where soil–structure interaction is important.

These limits are removed one at a time by the extensions of the limit-state theory, the plasticity-based solutions and the elastic and elastodynamic formulations, which deal with cohesion and wall

adhesion, the point of application of the seismic increment, intermediate wall movement, wall friction, the flexibility of the wall and foundation, and soil stiffness that varies with depth. It was shown by the kinematic solutions that the pressure is controlled by the relative displacement between wall and soil, rather than by the acceleration.

Most of these solutions, however, do not account for the separation of the soil from the wall. Since continuous contact is a basic assumption of the limit-state and the elastic solutions, they cannot be used to estimate how separation changes the distribution and the magnitude of the seismic pressure.

Numerical simulations, model tests and field observations are needed to test these formulations. They are covered in the companion chapter, Seismic Performance of Retaining Walls: Numerical, Experimental, and Field Evidence.

Disclosure Statement

The author used AI-based tools (ChatGPT and Claude) to assist with language editing, text restructuring and formatting. The author reviewed the revised text and checked the scientific content, including the selection and interpretation of the cited studies.

References

Absi, E. (2017). *Active and passive earth pressure tables*. Routledge.

Anderson, D. G. (2008). *NCHRP Report 611: Seismic analysis and design of retaining walls, buried structures, slopes, and embankments*. Transportation Research Board.

Brandenberg, S. J., Durante, M. G., Mylonakis, G., & Stewart, J. P. (2020). Winkler solution for seismic earth pressures exerted on flexible walls by vertically inhomogeneous soil. *Journal of Geotechnical and Geoenvironmental Engineering, 146*(11), 04020127.

Brandenberg, S. J., Mylonakis, G., & Stewart, J. P. (2015). Kinematic framework for evaluating seismic earth pressures on retaining walls. *Journal of Geotechnical and Geoenvironmental Engineering, 141*(7), 04015031.

Brandenberg, S. J., Mylonakis, G., & Stewart, J. P. (2017). Approximate solution for seismic earth pressures on rigid walls retaining inhomogeneous elastic soil. *Soil Dynamics and Earthquake Engineering, 97*, 468–477.

Building Seismic Safety Council. (2020). *NEHRP recommended seismic provisions for new buildings and other structures (FEMA P-2082-2)*. Federal Emergency Management Agency.

Caquot, A. I., & Kérisel, J. L. (1948). *Tables for the calculation of passive pressure, active pressure and bearing capacity of foundations*. Gauthier-Villars.

Chen, W.-F., & Liu, X. (2012). *Limit analysis in soil mechanics*. Elsevier.

Coulomb, C. A. (1776). *Essai sur une application des règles des maximis et minimis à quelques problèmes de statique*.

Das, B. M., & Puri, V. K. (1996). Static and dynamic active earth pressure. *Geotechnical and Geological Engineering, 14*, 353–366.

Durante, M. G., Stewart, J. P., Brandenberg, S. J., & Mylonakis, G. (2022). Simplified solution for seismic earth pressures exerted on flexible walls. *Earthquake Spectra, 38*(3), 1872–1892. https://doi.org/10.1177/87552930221083326

Efeoglu, T. (2024). *Contributions to the static and dynamic analysis of earth retaining structures* [Doctoral dissertation, University of Bristol]. University of Bristol Research Portal.

Efeoglu, T., Karamitros, D. K., & Mylonakis, G. (2021). Effects of soil-wall separation on static earth pressures. In *Proceedings of the 9th Turkish Conference on Earthquake Engineering*.

European Committee for Standardization. (2004). *Eurocode 8: Design of structures for earthquake resistance—Part 5: Foundations, retaining structures and geotechnical aspects (EN 1998-5:2004)*. CEN.

Hushmand, A., Dashti, S., Davis, C., Hushmand, B., McCartney, J., Hu, J., & Lee, Y. (2016). Seismic performance of underground reservoir structures: Insight from centrifuge modeling on the influence of backfill soil type and geometry. *Journal of Geotechnical and Geoenvironmental Engineering, 142*(11), 04016058.

Kloukinas, P., Langousis, M., & Mylonakis, G. (2012). Simple wave solution for seismic earth pressures on nonyielding walls. *Journal of Geotechnical and Geoenvironmental Engineering, 138*(12), 1514–1519. https://doi.org/10.1061/(ASCE)GT.1943-5606.0000721

Kramer, S. L. (1996). *Geotechnical earthquake engineering*. Prentice Hall.

Lancellotta, R. (2002). Analytical solution of passive earth pressure. *Géotechnique, 52*(8), 617–619. https://doi.org/10.1680/geot.2002.52.8.617

Lancellotta, R. (2007). Lower-bound approach for seismic passive earth resistance. *Géotechnique, 57*(3), 319–321. https://doi.org/10.1680/geot.2007.57.3.319

Mononobe, N. (1929). On determination of earth pressure during earthquake. In *Proceedings of the World Engineering Congress, Tokyo* (Vol. 9, pp. 177–185).

Mononobe, N., & Matsuo, H. (1932). Experimental investigation of lateral earth pressure during earthquakes. *Earthquake Research Institute and Research Office of Public Works, Department of Home Affairs, 57*, 884–902.

Mylonakis, G., Kloukinas, P., & Papantonopoulos, C. (2007). An alternative to the Mononobe–Okabe equations for seismic earth pressures. *Soil Dynamics and Earthquake Engineering, 27*(10), 957–969. https://doi.org/10.1016/j.soildyn.2007.01.004

Newmark, N. M. (1965). Effects of earthquakes on dams and embankments. *Géotechnique, 15*(2), 139–160.

Okabe, S. (1924). General theory on earth pressure and seismic stability of retaining wall and dam. *Journal of the Japan Society of Civil Engineering, 10*(5).

Okabe, S. (1926). General theory on earth pressures and seismic stability of retaining wall and dam. *Journal of the Japan Society of Civil Engineering, 10*(6), 1277–132.

Papazafeiropoulos, G., & Psarropoulos, P. N. (2010). Analytical evaluation of the dynamic distress of rigid fixed-base retaining systems. *Soil Dynamics and Earthquake Engineering, 30*(12), 1446–1461.

Prakash, S., & Saran, S. (1966). Static and dynamic earth pressures behind retaining walls. In *Proceedings of the Third Symposium on Earthquake Engineering* (Vol. 1, pp. 277–288). University of Roorkee.

Psarropoulos, P., Klonaris, G., & Gazetas, G. (2005). Seismic earth pressures on rigid and flexible retaining walls. *Soil Dynamics and Earthquake Engineering, 25*(7–10), 795–809.

Richards, R., Jr., & Shi, X. (1994). Seismic lateral pressures in soils with cohesion. *Journal of Geotechnical Engineering, 120*(7), 1230–1251.

Scott, R. (1973). Earthquake-induced pressures on retaining walls. In *Proceedings of the 5th World Conference on Earthquake Engineering* (Vol. 2, pp. 1611–1620).

Seed, H. B., & Whitman, R. V. (1970). Design of earth retaining structures for dynamic loads. In *Lateral stresses in the ground and design of earth retaining structures* (pp. 103–147). American Society of Civil Engineers.

Steedman, R., & Zeng, X. (1990). The influence of phase on the calculation of pseudostatic earth pressure on a retaining wall. *Géotechnique, 40*(1), 103–112.

Veletsos, A. S., & Younan, A. H. (1994a). Dynamic modeling and response of soil-wall systems. *Journal of Geotechnical Engineering, 120*(12), 2155–2179.

Veletsos, A. S., & Younan, A. H. (1994b). Dynamic soil pressures on rigid vertical walls. *Earthquake Engineering & Structural Dynamics, 23*(3), 275–301.

Veletsos, A. S., & Younan, A. H. (1997). Dynamic response of cantilever retaining walls. *Journal of Geotechnical and Geoenvironmental Engineering, 123*(2), 161–172.

Vrettos, C. (2013). Dynamic response of soil deposits to vertical SH waves for different rigidity depth-gradients. *Soil Dynamics and Earthquake Engineering, 47*, 41–50.

Vrettos, C., Beskos, D., & Triantafyllidis, T. (2016). Seismic pressures on rigid cantilever walls retaining elastic continuously non-homogeneous soil: An exact solution. *Soil Dynamics and Earthquake Engineering, 82*, 142–153.

Wagner, N., & Sitar, N. (2018). Comparison of pseudo-static limit equilibrium and elastic wave equation analyses of dynamic earth pressures on retaining structures. In *Geotechnical earthquake engineering and soil dynamics V* (pp. 340–350). American Society of Civil Engineers.

Wu, G., & Finn, W. L. (1999). Seismic lateral pressures for design of rigid walls. *Canadian Geotechnical Journal, 36*(3), 509–522.

Younan, A. H., & Veletsos, A. S. (2000). Dynamic response of flexible retaining walls. *Earthquake Engineering & Structural Dynamics, 29*(12), 1815–1844.

Zeng, X., & Steedman, R. (1993). On the behaviour of quay walls in earthquakes. *Géotechnique*, 43(3), 417–431.

Zhang, J., Shamoto, Y., & Tokimatsu, K. (1998a). Evaluation of earth pressure under any lateral deformation. *Soils and Foundations, 38*(1), 15–33.

Zhang, J., Shamoto, Y., & Tokimatsu, K. (1998b). Seismic earth pressure theory for retaining walls under any lateral displacement. *Soils and Foundations, 38*(2), 143–163.

BÖLÜM 9

SUSTAINABLE SOIL IMPROVEMENT TECHNICS FOR CIRCULAR ECONOMY AND RESILIENCE IN ROAD INFRASTRUCTURES

HALİL OĞUZHAN KARA[1]

Introduction

Today, transport infrastructure—particularly road networks—remains a fundamental determinant of economic development and social well-being. However, the volume of natural resources consumed during the construction and operation of such infrastructure, the amount of waste generated, and the resulting greenhouse gas emissions have brought the sector to a critical juncture regarding sustainability. Traditional road construction largely relies on a linear "take-make-dispose" model, utilizing materials such as natural aggregates, cement, and water. This approach leads to the rapid depletion of raw material reserves, an increased carbon footprint due to energy-intensive production processes, and the accumulation of end-of-life road pavement and soil-improvement waste in landfills. Furthermore, the impacts of climate change—manifesting as more frequent extreme rainfall,

[1] Araştırma Görevlisi, Kastamonu Üniversitesi, Mühendislik ve Mimarlık Fakültesi, İnşaat Mühendisliği Bölümü, Orcid: 0000-0002-7655-8444

floods, temperature fluctuations, and periods of drought—are causing road infrastructure to reach the end of its service life sooner than anticipated. This not only results in economic losses but also disrupts social mobility and weakens emergency logistics. Consequently, there is an increasingly urgent need for new techniques that can both mitigate the environmental impact of road infrastructure and enhance its resilience against climate change.

In recent years, in response to this need, the concept of a circular economy has been increasingly adopted in civil engineering. Unlike the linear model, a circular economy aims to close material loops, treat waste as a resource, and extend the lifespan of products. In the context of road infrastructure, this approach involves using secondary raw materials—such as recycled asphalt, slag, fly ash, tire shreds, and construction and demolition waste—for soil improvement, opting for bio-based binders, and reprocessing excavated materials on-site. However, a circular approach alone is not sufficient. Reducing the carbon footprint of an infrastructure element loses its significance if the element cannot maintain its functionality over the long term. This is where the concept of resilience comes into play. Resilience refers to the capacity of an infrastructure system to maintain its function in the face of unexpected shocks (such as floods, earthquakes, landslides, or extreme temperatures) and prolonged stresses (such as soil settlement, freeze-thaw cycles, or traffic loads). When the circular economy and resilience are considered together, a paradigm emerges in which road infrastructure can adapt to both today's resource constraints and tomorrow's climatic uncertainties. This paradigm necessitates a holistic assessment—one that goes beyond initial costs or short-term performance when selecting soil improvement techniques—by also accounting for the environmental impacts of materials throughout their life cycle, the ease of maintenance, and the possibilities for recovery at the end of their service life.

Soil improvement is a cornerstone of road infrastructure, as the longevity and safety of a road depend directly on the load-bearing capacity, settlement behavior, and sensitivity to environmental factors of the underlying soil. Weak soils—such as high-plasticity clays, organic soils, loose sands, or expansive clays—are typically improved through methods like mechanical stabilization, chemical injection, drainage enhancement, or deep soil mixing. However, many of these conventional techniques consume significant amounts of energy and natural resources; for instance, the production of binders such as cement and lime accounts for a substantial share of global CO2 emissions. In this context, sustainable soil improvement encompasses innovative approaches that use low-carbon, energy-efficient, locally sourced, or waste-derived materials while enhancing the soil's long-term resistance to water, temperature fluctuations, and dynamic loads. Such techniques include biologically based methods (microbially induced calcite precipitation, enzymatic stabilization, and bioengineering with plant roots), stabilization using industrial by-products (such as blast-furnace slag, silica fume, fly ash, or phosphogypsum), and the application of eco-friendly stabilizers based on polymers or nanomaterials. Notably, microbially induced calcite precipitation has emerged in recent years as a promising technique; it leverages a natural process to increase soil strength and reduce permeability, requiring minimal energy and resulting in near-zero carbon emissions. Similarly, it has been demonstrated that soils mixed with waste tire shreds exhibit high energy-dissipation capacity under dynamic loads and can therefore be used to construct resilient road embankments in earthquake-prone regions.

However, several barriers hinder the widespread practical adoption of sustainable ground improvement techniques. Key among these are the limited field data on the long-term performance of such techniques, the failure of existing specifications and standards to

adequately reflect circular economy principles, regional variations in the availability of certain waste-based materials, and the perception that initial implementation costs are sometimes higher than those of traditional methods. Furthermore, the test methods and design parameters used to assess resilience have not yet been fully standardized for sustainable materials. These gaps necessitate establishing a bridge between academic research and field applications.

The objective of this study is to provide a comprehensive examination of sustainable soil improvement techniques for road infrastructure that align with circular economy principles and enhance system resilience to climate change and other unforeseen events. First, the concepts of the circular economy and resilience will be defined and evaluated within the specific context of soil improvement. Subsequently, key sustainable soil improvement techniques will be assessed based on their operational principles, environmental impacts, cost-effectiveness, and contributions to resilience. The study aims to analyze sustainable alternatives—grounded in circular economy principles—that address the high carbon footprint and natural resource consumption associated with traditional soil improvement methods (such as lime or cement) used in road infrastructure. The unique contribution of this work lies in its integration of waste material utilization, biopolymers, life-cycle assessment, and climate resilience into a unified framework, offering a holistic resource to guide both practitioners and researchers.

This study is intended to serve as a guide for engineers, planners, academics, and decision-makers responsible for road infrastructure to facilitate the construction of greener, safer, and longer-lasting roads.

Current Researches in the Field

In recent years, efforts to reduce the construction sector's environmental footprint and enhance resource efficiency have necessitated integrating circular economy principles into geotechnical practice. Soil improvement techniques, particularly within road infrastructure, emerge as a strategic area for the utilization of industrial and agricultural waste. Ghisellini et al. (2018) address the transformation expected from a circular economy—characterized by a balanced interaction between environmental and economic systems—within a theoretical framework, advocating for a focus on the reuse and recovery stages of the waste hierarchy (Ghisellini, Cialani, and Ulgiati, 2016). Similarly, Bamigboye et al. (2021) provide a comprehensive assessment of the use of waste materials in highway applications, documenting the positive impacts of these approaches on sustainability (Bamigboye et al., 2021).

Research on the use of industrial waste for soil improvement demonstrates the effectiveness of materials such as granulated blast-furnace slag, cement kiln dust, calcium carbide residue, and silica fume. Almuaythir et al. (2024) systematically compared various industrial wastes for the stabilization of expansive clays, finding that the addition of 9% slag increased the unconfined compressive strength from 114.64 kPa to 1582.91 kPa, while reducing the liquid limit by 37.66% (Almuaythir, Zaini, Hasan, and Hoque, 2024). Sharma and Sivapullaiah (2016) state that slag supplemented with fly ash serves as an effective binder for the stabilization of expansive soils; this combination enhances sulfate resistance, thereby increasing the durability of infrastructure (A. K. Sharma and Sivapullaiah, 2016). Furthermore, Horpibulsuk et al. (2012) examined strength development in silty clay soils treated with mixtures of calcium carbide and fly ash, demonstrating that these wastes trigger pozzolanic reactions through the formation of calcium

silicate hydrate (C-S-H) and calcium aluminate hydrate (C-A-H) (Horpibulsuk, Phetchuay, and Chinkulkijniwat, 2012).

The use of agricultural waste also plays a significant role in sustainable geotechnical studies. Bio-wastes such as rice husk ash, sugarcane bagasse ash, and marble dust are being investigated as alternatives to traditional binders. In their study on the moisture sensitivity of reclaimed asphalt pavement materials, Arulrajah et al. (2020) emphasize that lightweight stabilization techniques align with the principles of a circular economy and enhance the longevity of infrastructure layers (Arulrajah, Mohammadinia, Haghighi, & Horpibulsuk, 2022). Dang et al. (2021) examined the role of sugarcane bagasse ash in improving the engineering properties of expansive clays, demonstrating the positive impact of waste materials on geotechnical performance (Dang, Khabbaz, & Ni, 2021). Anburuvel et al. (2023) investigated the use of eggshell ash and rice husk ash in the geopolymer-based stabilization of lateritic soils, concluding that these mixtures are suitable for road construction (Anburuvel, Sathiparan, Dhananjaya, & Anuruththan, 2023). The utilization of construction and demolition waste in road infrastructure plays a critical role in the practical application of a circular economy. Arulrajah and Mohammadinia (2014) examined the physical properties and shear strength responses of reclaimed construction and demolition materials used in unbound base/subbase layers, confirming their viability as alternatives to conventional aggregates (Arulrajah, Disfani, Horpibulsuk, Suksiripattanapong, and Prongmanee, 2014). Lu et al. (2021) analyzed the resilient and permanent deformation behavior of construction and demolition waste, demonstrating that these materials exhibit satisfactory performance in terms of load-bearing capacity and resilience (Lu et al., 2021). Meanwhile, Kianimehr et al. (2019) evaluated the potential for using reclaimed concrete aggregates in lightly stabilized clay soils, noting that this approach offers both economic and

environmental benefits (Kianimehr, Shourijeh, Binesh, Mohammadinia, and Arulrajah, 2019).

The resilience and sustainability performance of ground improvement techniques are also supported by life-cycle assessment tools. Reviewing sustainable approaches in transportation infrastructure geotechnics, Gomes Correia et al. (2016) argue that the use of waste materials is effective in reducing carbon footprints and developing resilient infrastructure capable of adapting to climate change (Gomes Correia, Winter, and Puppala, 2016). Analyzing current trends and future research directions regarding the circular economy of construction and demolition waste, Oluleye et al. (2022) highlight the importance of these strategies in achieving waste policy objectives (Oluleye, Chan, Saka, and Olawumi, 2022). Furthermore, by examining the behavior of reclaimed asphalt pavement as a sub-ballast layer for railways, Hashemian et al. (2023) have demonstrated that this material contributes to infrastructure resilience, aligning with circular economy principles (Elyas Hashemian, Moghadas Nejad, and Esmaeili, 2023).

Microstructural analyses are critical to explaining the bonding mechanisms underlying soil stabilization with waste materials. Through scanning electron microscopy, Almuaythir et al. (2024) documented that the interaction of slag and other industrial wastes with clays leads to the formation of C-S-H and C-A-H gels; these compounds create strong bonds between soil particles, thereby enhancing strength (Almuaythir et al., 2024). Investigating the impact of stabilizing soil with mixtures of waste tires and recycled concrete aggregates on mechanical properties, Juveria et al. (2023) demonstrated that this complex approach to waste management offers innovative solutions for infrastructure materials (Juveria, Rajeev, Jegatheesan, and Sanjayan, 2023).

Within the framework of circular economy principles, soil improvement for road infrastructure requires a multidimensional

approach to sustainability. The integrated use of industrial, agricultural, and construction waste not only enhances engineering performance but also mitigates environmental impacts and strengthens the resilience of infrastructure systems against climate change and excessive loading. Future research should focus on long-term performance monitoring and the development of standardized mix-design protocols based on regional waste streams.

Soil Stabilization Using Waste and Alternative Materials

The high carbon emissions and costs associated with traditional binders, such as cement and lime, have accelerated research into alternative stabilization materials. Soil improvement applications in road infrastructure offer an ideal platform for the utilization of waste materials from both industrial and agricultural sources. In this context, the use of waste materials for soil stabilization—aligned with the principles of a circular economy—forms the foundation for sustainable infrastructure development strategies. In a study on the stabilization of expansive clays using mixtures of granulated blast furnace slag, fly ash, cement kiln dust, calcium carbide residue, and silica fume, researchers found that a mixture containing 9% slag increased the unconfined compressive strength from 114.64 kPa to 1582.91 kPa, while reducing the liquid limit by 37.66% (Almuaythir et al., 2024). In another study involving soil samples stabilized with rice husk ash, steel slag, and iron waste dust, researchers observed an increase in mechanical strength of up to 60% following the addition of steel slag and iron waste, and confirmed through microstructural analysis that hydration reactions had been enhanced (Cai et al., 2025).

The effectiveness of industrial wastes for soil stabilization varies with their pozzolanic and binding properties. It has been demonstrated that fly ash modified with blast-furnace slag provides effective stabilization for expansive soils, enhancing sulfate

resistance and improving long-term performance (A. K. Sharma and Sivapullaiah, 2016). Research into the strength development of silty clay soils treated with mixtures of calcium carbide residue and fly ash has documented that the high calcium hydroxide content of calcium carbide triggers the formation of calcium silicate hydrate (C-S-H) and calcium aluminate hydrate (C-A-H), thereby improving the physical properties of the stabilized soil mass (Horpibulsuk et al., 2012). Furthermore, it has been reported that a cementitious binder based on phosphogypsum, fly ash, and steel slag yields a 33.18% higher ultimate compressive strength in stabilized waste soil than Portland cement and also demonstrates superior performance under freeze-thaw and wet-dry cycles (Guo et al., 2025).

The use of agricultural waste in geotechnical applications is significant for both environmental sustainability and economic benefits. It has been demonstrated that for clay soils stabilized with a mixture of wheat straw ash and lime, a composition of 7% lime and 1% wheat straw ash results in a maximum dry unit weight exceeding 1700 kg/m³ and an increase in Unconfined Compressive Strength (UCS) values to 291.71 kN/m² (Adekanle et al., 2026). Research has shown that sugarcane bagasse ash reduces the plasticity index of expansive clays—thereby lowering their swelling potential—and has proven its viability as an alternative binder (Dang et al., 2021). Furthermore, studies on the use of eggshell ash and rice husk ash for the geopolymer-based stabilization of lateritic soils have determined that these waste materials provide suitable engineering properties for road construction (Anburuvel et al., 2023).

The use of construction and demolition waste for soil improvement represents one of the most practical applications of the circular economy. An assessment of the potential of using recycled concrete aggregates in lightly stabilized clay soils revealed that adding such waste concrete aggregates enhances the soil's load-bearing capacity, demonstrating that this approach is beneficial from

both economic and environmental perspectives (Kianimehr et al., 2019). In their study on the moisture sensitivity of demolition materials containing reclaimed asphalt pavement, Arulrajah et al. (2022) emphasize that light stabilization techniques enhance the longevity of infrastructure layers. Research has shown that stabilizing mixtures of waste tires and recycled concrete aggregates provides high energy absorption and durability for flexible road infrastructure (Juveria et al., 2023).

Mineral wastes—such as waste glass, marble dust, and granite dust—are also being evaluated as alternative materials for soil stabilization. It has been noted that stabilizing pumice soils with alkali-activated waste glass increases the California Bearing Ratio (CBR) from 21.67% to 64.70%, suggesting that glass-based alkali activation offers a sustainable application for road sub-bases (Kalatehjari, Najafi, and Asadi, 2025). An investigation into the effectiveness of marble dust in improving expansive clay soils revealed that its addition reduces the plasticity index and enhances the soil's volumetric stability (Abdelkader, Hussein, and Ye, 2021). Furthermore, the use of marble dust as a sustainable stabilization material in sub-base layers has been shown to optimize soil load-bearing capacity and compaction (Jassim, Hassan, Mohammed, and Fattah, 2022).

Understanding stabilization mechanisms is critical to the effective utilization of waste materials. Reviewing the applications of industrial waste-based geopolymers in soil stabilization, K. Sharma and Kumar (2020) identify the optimal parameters as a geopolymer mixture ratio of 5–20%, a molarity (M) of 8–12, a curing temperature of 25–45°C, and a curing duration of 7–28 days. They note that the formation of C-S-H gel, silicates, calcite, and aluminate compounds is the primary driver of improvements in engineering properties. Ajayi et al. (2024) highlight the contribution of stabilization using waste materials to the United Nations Sustainable

Development Goals (SDGs), stating that—when managed correctly—this approach offers a "win-win" scenario for both economic and environmental sustainability; however, they caution that the risks of hazardous substances or dust leakage must be carefully assessed (Ajayi, Epelle, and Akinwumi, 2024).

Soil stabilization using waste and alternative materials represents a promising strategy for implementing circular economy principles in road infrastructure and developing resilient ground conditions. Combining industrial, agricultural, and mineral wastes in appropriate proportions, alongside the application of advanced stabilization techniques such as alkali activation, enables the design of high-performance, eco-friendly infrastructure systems. Future research should focus on optimizing the effects of various waste types and monitoring long-term field performance.

Life Cycle Assessment

Life cycle assessment and life cycle cost analysis—developed to measure the sustainability performance of infrastructure projects objectively—have become indispensable tools for evaluating the environmental and economic impacts of ground improvement applications in road infrastructure from a holistic perspective. Structured within the framework of the ISO 14040:2006 and ISO 14044:2006 standards, these approaches account for all environmental inputs and outputs of a product or service throughout its entire life cycle—from the extraction of raw materials through production and use, to the end-of-service stage (International Organization for Standardization, 2006a, 2006b). Furthermore, they enable the analysis of all costs incurred over the service life of structural assets by discounting them to their present value (International Organization for Standardization, 2017). In geotechnical engineering, integrating these methodologies into the assessment of ground improvement techniques is critical,

particularly for applying circular-economy principles and addressing climate change.

The use of these methodologies to determine the environmental impact profiles of ground improvement techniques has gained significant momentum over the last decade. Research has compared five common ground improvement methods used to mitigate liquefaction risk—compaction grouting, deep dynamic compaction, deep soil mixing (DSM), vibro-compaction, and vibro-replacement (stone columns)—within the framework of life cycle sustainability assessment. The results indicate that deep soil mixing and compaction grouting, both of which rely on Portland cement, are the techniques with the highest environmental impact and cost due to their use of energy-intensive materials. In contrast, vibration-based methods—such as vibro-compaction and deep dynamic compaction—emerge as more sustainable alternatives, despite involving greater variability and uncertainty regarding their impacts and costs (Vitor and Danziger, 2021). These findings indicate that, in the design of ground improvement, environmental impacts should be integrated into the decision-making process alongside performance criteria.

Defining system boundaries is of critical importance when assessing the life-cycle environmental impacts of soil stabilization in road infrastructure. Researchers employed the "Streamlined Energy and Emissions Assessment Model" (SEEAM)—a flowchart-based model—to evaluate three alternative soil-improvement options for river embankment stabilization, including prefabricated vertical drains and pile-supported concrete T-walls. The analysis revealed that one of these designs had the lowest impact on embodied energy and carbon dioxide emissions; however, it was deemed technically infeasible due to the time constraints required for flood protection (Shillaber, Mitchell, and Dove, 2016). This finding underscores the necessity of integrating technical

performance and time constraints—not just environmental indicators—into sustainability assessments. In a subsequent study by the same researchers, a Monte Carlo simulation-based methodology was used to conduct a comparative analysis that accounted for variability in soil conditions and impact coefficients. This approach allows determination of whether alternative methods differ significantly in embodied energy and emissions (Shillaber, Mitchell, Dove, and Ostrum, 2017).

Assessing the use of construction and demolition waste in soil improvement over its entire life cycle highlights the impact of circular economy practices on the carbon footprint. A comparative analysis was conducted on two different soil improvement methods through the lens of circularity. The results demonstrated that the use of reclaimed materials not only reduces costs but also significantly decreases greenhouse gas emissions. In particular, the environmental burden resulting from the production phase of binders used in ground improvement applications accounts for approximately 60–80% of the total life-cycle impact (Miguel et al., 2022). In this context, the use of secondary binders derived from industrial waste—such as ground granulated blast-furnace slag (GGBS) and fly ash—can reduce the carbon footprint by 40–60% compared to Portland cement.

Life-cycle cost analysis is a critical tool for evaluating the economic sustainability of using waste materials in road infrastructure. In a comprehensive study conducted for an urban highway section in Abu Dhabi—covering a 30-year analysis period (2015–2045)—researchers examined the cost implications of incorporating reclaimed asphalt pavement, recycled construction and demolition waste, and blast furnace slag. The optimal scenario—consisting of 25% reclaimed material in the sub-base, 80% in the unbound base, 25% in the hot-mix asphalt base, 15% in the binder and surface layers, and a concrete mix containing 65% ground

granulated blast furnace slag (GGBFS)—yielded a cost saving of $2.6 million (16%) over the 30-year life cycle. The analysis results indicate that the use of sustainable materials leads to a 10.3% reduction in construction costs and a 42.9% reduction in maintenance and repair costs (Hasan, Whyte, Al Jassmi, and Hasan, 2022). These findings demonstrate that the use of reclaimed materials is not merely an environmental consideration, but a strategic decision that offers significant economic benefits.

Evaluating soil improvement techniques across a broad range of environmental impact categories is essential for a holistic approach to sustainability. A hierarchical framework has been developed to assess the sustainability of soil-improvement techniques for infrastructure foundations. This framework integrates economic dimensions (construction and service-life costs) with environmental and social dimensions (such as local employment, user health and safety, and worker health and safety). The study emphasizes that life cycle assessment should not be limited to global warming potential and energy use but should encompass multiple impact categories, such as water consumption, land use, acidification, eutrophication, and human toxicity (Sánchez-Garrido, Navarro, and Yepes, 2022). Similarly, in an environmental and economic assessment of bio-grouting (bacterial-based cementation) and jet grouting techniques, it was documented that the bio-grouting method has a carbon footprint 30–40% lower than that of conventional jet grouting. However, it entails certain limitations regarding application time and sensitivity to soil conditions (Suer, Hallberg, Carlsson, Bendz, and Holm, 2009).

The standardization of life-cycle applications and the development of a methodological framework in geotechnical engineering represent fundamental challenges the discipline faces in its transition toward sustainability. A critical assessment of research on the application of these concepts to geotechnical systems reveals

that the field faces unique challenges, primarily due to the site-specific, heterogeneous nature of soil conditions. The review indicates that many studies limit their system boundaries to the construction phase, excluding the operational and end-of-life phases. This stems from the common assumption that ground improvement structures have an infinite service life and require no maintenance. However, the difficulty of identifying the root causes of failures—such as crack formation in tracks (whether due to overloading, thin asphalt layers, or inadequate ground improvement)—complicates modeling of the operational phase (De Melo, Kendall, and DeJong, 2024).

A methodological framework is proposed for integrating life-cycle considerations into geotechnical engineering projects. This four-stage methodology—encompassing geotechnical design, improvement, and evaluation—enables a systematic comparison of the environmental and economic performance of various ground improvement alternatives. In particular, the identification of three distinct improvement pathways—adjustments to the superstructure, reductions in material quantities, and material substitution—facilitates optimizing the design process with a focus on sustainability (Ida Samuelsson, Spross, and Larsson, 2024). However, researchers emphasize that input data (unit costs, emission factors, conversion coefficients) for geotechnical engineering projects are generally insufficient in standard databases, and that collaboration between industry and academia needs to be strengthened (I Samuelsson, Larsson, and Spross, 2021).

In a case study of an underground excavation near Milan, five different ground improvement technologies—permeation grouting, single- and double-fluid jet grouting, and artificial ground freezing (using brine or liquid nitrogen)—were evaluated using the Envision protocol and the "Do No Significant Harm" (DNSH) criteria. A three-stage assessment methodology—comprising an

Envision/DNSH evaluation, a life cycle assessment, and an integrated assessment—provides a systematic approach for quantifying the environmental impacts of ground improvement works and enhancing their sustainability performance. The study concludes that key areas for improving sustainability in ground improvement processes include climate and resilience (focusing on emissions), resource allocation (focusing on materials and energy), and leadership (fostering collaboration across industry sectors) (Pettinaroli, 2024).

For road infrastructure, the life cycle assessment of ground improvement techniques must encompass not only energy consumption and carbon emissions but also impacts on soil and land resources. It is argued that since the primary material involved in ground improvement is the existing soil, stages such as demolition, disposal, and recovery are not applicable. However, given the significant environmental burden associated with the production of binders—such as cement, lime, or chemical soil additives—a "cradle-to-site" approach (covering the entire process from raw material extraction through to the construction phase) is the most commonly adopted system boundary (Shillaber et al., 2016). They have developed a qualitative approach for assessing impacts on soil quality, noting that criteria such as erosion resistance, mechanical filtration capacity, and biodiversity should be taken into account (Vitor and Danziger, 2021).

Life cycle assessment of soil improvement techniques in road infrastructure requires a multidimensional analysis. Integrating a life cycle perspective enables decision-makers to evaluate not only environmental impacts but also long-term economic sustainability. The use of waste materials reduces both costs and the carbon footprint throughout the life cycle. However, the site-specific nature of geotechnical engineering complicates the development of standardized life cycle methodologies, necessitating strong

collaboration between industry practitioners and researchers. Future research should focus on modeling the usage and end-of-life phases, incorporating uncertainty analyses, and including ecosystem services—such as biodiversity—in the assessment process.

Artificial Intelligence and Data-Driven Modeling

The rapid advancement of artificial intelligence and machine learning technologies is driving a transformative paradigm shift in geotechnical engineering and ground improvement practices. Traditionally, analyses of soil behavior—relying on deterministic approaches such as the finite element method and limit equilibrium methods—have been constrained when dealing with complex, non-linear, and spatially variable conditions. Artificial intelligence-based approaches, with their capacity to process large datasets, model uncertainties, and provide real-time decision support, play a critical role in optimizing sustainable ground improvement techniques that align with the principles of a circular economy. Research has demonstrated that AI applications offer advantages over conventional methods across a broad spectrum of areas, ranging from soil mechanics and foundation engineering to slope stability and soil classification (Gomes Correia, Cortez, Tinoco, and Marques, 2013).

Machine learning algorithms provide time- and cost-efficient alternatives for predicting the mechanical properties of stabilized soils. Models developed for estimating unconfined compressive strength, in particular, facilitate rapid decision-making by minimizing the need for laboratory testing. For instance, researchers have used support vector machines to predict the properties of soils stabilized with cement and fly ash, achieving high accuracy (Kumar, Sinha, Saurav, and Chauhan, 2024). Similarly, studies estimating the compressive strength of fine-grained soils stabilized with various agents—including nano-SiO_2—have shown that machine learning

algorithms, specifically XGBoost and Random Forest models, outperform traditional regression techniques (Ghavami and Naseri, 2025). A hybrid XGB model was developed to estimate the unconfined compressive strength (UCS) of cohesive soils stabilized with waste materials and cement, demonstrating its ability to capture complex relationships (Yao, Tu, Yang, and Zhao, 2024).

Deep learning and hybrid models offer significant advantages for modeling complex geotechnical systems. In particular, artificial neural networks, backpropagation algorithms, and evolutionary polynomial regression are widely used to predict the behavior of stabilized soil. Research has utilized deep learning methods to estimate the strength of single-component geopolymer-stabilized soils, enhancing model performance by combining real-world and synthetic data (Chen, Hu, and Wu, 2024). A four-stage methodology has been proposed for integrating machine learning with life cycle assessment and life cycle cost analysis in the geotechnical design process; this framework identifies optimization pathways, such as structural adjustments, reductions in material quantities, and material substitutions (Ida Samuelsson et al., 2024).

Explainable AI (XAI) enhances the transparency of deep learning models—often characterized as "black boxes"—enabling engineers to understand and trust their decisions. Techniques such as SHAP (SHapley Additive exPlanations) and LIME (Local Interpretable Model-agnostic Explanations) enable quantitative assessment of the influence of input variables on the output, making the results physically interpretable. In a study focused on predicting pile-driving vibrations in the soft clay soils of Bangkok, a deep neural network model was developed; SHAP analysis revealed that distance is the most influential factor affecting peak particle velocity, while hammer weight and pile dimensions exhibit non-linear relationships (Youwai and Pamungmoon, 2025). Similarly, the use of XAI in strength prediction for stabilized soils helps optimize

formulation strategies by revealing the impact of binder dosages—such as NaOH and GGBS—and their synergistic interactions (Luo et al., 2025).

The integration of the Internet of Things (IoT) and artificial intelligence (AI) offers opportunities for real-time optimization in geotechnical field monitoring and compaction operations. Smart sensors enable continuous monitoring of the soil compaction process, allowing comparison of quality control parameters directly with design parameters by integrating roller data with numerical models. Highlighting the transformative impact of AI and IoT on geotechnical field monitoring and construction, it has been noted that early warning systems—which provide real-time feedback—facilitate timely interventions and ensure safety on construction sites (Gomes Correia et al., 2013). Smart compaction technology, which utilizes machine learning algorithms to classify soil and estimate optimal compaction parameters, enables continuous assessment of geomaterial properties.

Digital twin technology is revolutionizing geotechnical engineering across the planning, design, construction, monitoring, and maintenance phases. Functioning as virtual replicas of physical assets, digital twins provide project stakeholders with real-time information—via simulations and predictive analytics—regarding soil movements, the progress of excavation or fill operations, and stability status. It has been demonstrated that the use of digital twins in deep excavation and earthwork projects, particularly under complex soil conditions, can accelerate the design process by up to 50% and support sustainable construction practices by optimizing the cut-and-fill balance (Haryono, Saw, Lee, and Wong, 2022). It has been demonstrated that probabilistic digital twins offer data-driven approaches for reducing uncertainty and determining optimal preloading within geotechnical design and construction processes (Cotoarbă, Straub, and Smith, 2025).

Optimization algorithms are effectively employed to refine soil stabilization mix designs and application parameters. Genetic algorithms, when integrated with artificial neural networks, are used to estimate the resilient modulus of stabilized soils and to develop new empirical formulas. These hybrid approaches facilitate the determination of optimal binder dosages and curing conditions by modeling complex soil-additive interactions (McKenna, Argyroudis, Winter, and Mitoulis, 2021). Automated machine learning frameworks, such as Optuna, enhance the performance of soil stability prediction models by accelerating hyperparameter optimization and model selection processes. By using the Optuna algorithm for optimization, hybrid deep learning models have achieved 99.4% accuracy in predicting the infinite-slope stability of nano-silica-stabilized soils (Li et al., 2025).

The success of artificial intelligence-based models in geotechnical applications relies on the availability of large, high-quality datasets. Long-term performance data, site characterization, and laboratory test results serve as primary data sources for training machine learning models. Research focused on estimating the resilient modulus of subgrade soils has demonstrated that machine learning models—specifically those incorporating genetic algorithms and artificial neural networks—outperform traditional methods (Khawaja et al., 2024). Furthermore, artificial intelligence applications are used to optimize the incorporation of waste materials into soil stabilization, enabling prediction of these materials' engineering properties and automating mix design processes. Artificial intelligence and data-driven modeling offer transformative potential for the development and implementation of sustainable soil improvement techniques in road infrastructure. The integration of machine learning, deep learning, XAI (explainable AI), IoT, digital twins, and optimization algorithms provides a comprehensive framework for more accurate prediction of soil

behavior, real-time optimization of construction processes, and enhanced resilience of infrastructure systems. Future research should focus on multi-objective optimization (balancing cost, environmental impact, and performance), real-world digital twin applications, and the establishment of regional databases.

Results and Evaluations

The integration of circular economy principles into soil improvement practices for road infrastructure reveals a transformative potential for both environmental sustainability and infrastructure resilience. A systematic assessment indicates that industrial and agricultural wastes—such as granulated blast-furnace slag, fly ash, rice husk ash, and reclaimed construction and demolition waste—exhibit engineering performance that is either superior to or at least equivalent to that of traditional binders. Specifically, slag-based stabilization has been shown to increase the unconfined compressive strength of expansive clays from 114.64 kPa to 1582.91 kPa (Almuaythir et al., 2024) and enhance sulfate resistance, thereby ensuring the longevity of infrastructure (A. K. Sharma and Sivapullaiah, 2016). Furthermore, the use of bio-wastes, such as sugarcane bagasse ash, has been found to improve volumetric stability by reducing the plasticity index by 37.66% (Dang et al., 2021).

Findings from life cycle assessment and life cycle cost analysis confirm that soil improvement using waste materials is sustainable not only from a technical standpoint but also from ecological and economic perspectives. Comparative analyses indicate that vibration-based methods, such as vibro-compaction, have a lower carbon footprint compared to cement-based deep mixing (Vitor and Danziger, 2021), while Hasan et al. (2022) demonstrated that the use of reclaimed asphalt pavement and blast furnace slag results in a 16% cost saving over a 30-year service life

(Hasan et al., 2022). The hierarchical assessment framework emphasizes that environmental impact categories should not be limited to global warming potential but should encompass multiple indicators, such as acidification, eutrophication, and human toxicity (Sánchez-Garrido et al., 2022).

The integration of artificial intelligence and data-driven modeling techniques enables optimized decision-making in the design and implementation of ground improvement. Machine learning algorithms (such as SVM, XGBoost, and Random Forest) can predict the unconfined compressive strength of stabilized soils with high accuracy (DOI: Kumar et al., 2024; Yao et al., 2024), thereby reducing the need for laboratory testing and facilitating rapid decision-making. Meanwhile, digital twin and IoT technologies enable real-time field monitoring and the optimization of compaction operations (Cotoarbă et al., 2025). Furthermore, explainable artificial intelligence (XAI) applications enhance the interpretability of "black-box" models, allowing engineers to place greater trust in their decisions.

From a resilience perspective, soils stabilized with waste materials perform comparably to—or even better than—soils treated via traditional methods when subjected to extreme weather events driven by climate change (such as freeze-thaw or wetting-drying cycles). Notably, binders based on phosphogypsum, fly ash, and steel slag have shown superior freeze-thaw resistance compared to Portland cement (Guo et al., 2025), making them an attractive choice for the development of reliable infrastructure systems in regions with variable climatic conditions.

In conclusion, the widespread adoption of circular economy-oriented soil improvement techniques requires the development of standardized mix-design protocols, the creation of databases based on regional waste streams, and the integration of AI-driven decision-support systems. Future research should focus on long-term field

performance monitoring, multi-objective optimization (balancing cost, environmental impact, and performance), and the assessment of ecosystem services, including biodiversity. It is recommended to focus on its inclusion.

References

Abdelkader, H. A. M., Hussein, M. M. A. ve Ye, H. (2021). Influence of Waste Marble Dust on the Improvement of Expansive Clay Soils. Advances in Civil Engineering, 2021(1), 3192122. doi:10.1155/2021/3192122

Adekanle, A. A., Okunade, E. A., Alo, B. A., Awolusi, T. F., Barraj, F. ve Azab, M. (2026). Mechanical and microstructural evaluation of lime-wheat husk ash blend for clay subgrade stabilization. Frontiers in Built Environment, 12, 1768387. doi:10.3389/fbuil.2026.1768387

Ajayi, V., Epelle, P. ve Akinwumi, I. (2024). SUSTAINABLE SOIL STABILIZATION OF ROAD PAVEMENT LAYERS USING WASTE MATERIALS: A MINI-REVIEW. Detritus, (29), 120-134. doi:10.31025/2611-4135/2024.19434

Almuaythir, S., Zaini, M. S. I., Hasan, M. ve Hoque, Md. I. (2024). Sustainable soil stabilization using industrial waste ash: Enhancing expansive clay properties. Heliyon, 10(20), e39124. doi:10.1016/j.heliyon.2024.e39124

Anburuvel, A., Sathiparan, N., Dhananjaya, G. M. A. ve Anuruththan, A. (2023). Characteristic evaluation of geopolymer based lateritic soil stabilization enriched with eggshell ash and rice husk ash for road construction: An experimental investigation. Construction and Building Materials, 387, 131659. doi:10.1016/j.conbuildmat.2023.131659

Arulrajah, A., Disfani, M. M., Horpibulsuk, S., Suksiripattanapong, C. ve Prongmanee, N. (2014). Physical

properties and shear strength responses of recycled construction and demolition materials in unbound pavement base/subbase applications. Construction and Building Materials, 58, 245-257. doi:10.1016/j.conbuildmat.2014.02.025

Arulrajah, A., Mohammadinia, A., Haghighi, H. ve Horpibulsuk, S. (2022). Effect of moisture sensitivity on the light stabilisation of demolition materials in pavement bases. Road Materials and Pavement Design, 23(4), 787-801. doi:10.1080/14680629.2020.1843525

Bamigboye, G. O., Bassey, D. E., Olukanni, D. O., Ngene, B. U., Adegoke, D., Odetoyan, A. O., … Nworgu, A. T. (2021). Waste materials in highway applications: An overview on generation and utilization implications on sustainability. Journal of Cleaner Production, 283, 124581. doi:10.1016/j.jclepro.2020.124581

Cai, D., Ouyang, M., Bao, X., Zhang, Q., Bi, Z., Yan, H., … Shi, Y. (2025). Performance Evaluation of Stabilized Soils with Selected Common Waste Materials of Rice Husk Ash, Steel Slag and Iron Tailing Powder. Materials, 18(2), 346. doi:10.3390/ma18020346

Chen, Q., Hu, G. ve Wu, J. (2024). Prediction of the Unconfined Compressive Strength of a One-Part Geopolymer-Stabilized Soil Using Deep Learning Methods with Combined Real and Synthetic Data. Buildings, 14(9), 2894. doi:10.3390/buildings14092894

Cotoarbă, D., Straub, D. ve Smith, I. F. C. (2025). Probabilistic digital twins for geotechnical design and construction. Data-Centric Engineering, 6, e30. doi:10.1017/dce.2025.10008

Dang, L. C., Khabbaz, H. ve Ni, B.-J. (2021). Improving engineering characteristics of expansive soils using industry waste

as a sustainable application for reuse of bagasse ash. Transportation Geotechnics, 31, 100637. doi:10.1016/j.trgeo.2021.100637

De Melo, D. L., Kendall, A. ve DeJong, J. T. (2024). Evaluation of life cycle assessment (LCA) use in geotechnical engineering. Environmental Research: Infrastructure and Sustainability, 4(1), 012001. doi:10.1088/2634-4505/ad2154

Elyas Hashemian, S., Moghadas Nejad, F. ve Esmaeili, M. (2023). Laboratory and numerical investigation on the behavior of reclaimed asphalt pavement (RAP) as railway track subballast layer. Construction and Building Materials, 384, 131442. doi:10.1016/j.conbuildmat.2023.131442

Ghavami, S. ve Naseri, H. (2025). Prediction of Compressive Strength in Fine-Grained Soils Stabilized with a Combination of Various Stabilization Agents and Nano-SiO2 Using Machine Learning Algorithms. Mathematical and Computational Applications, 30(6), 137. doi:10.3390/mca30060137

Ghisellini, P., Cialani, C. ve Ulgiati, S. (2016). A review on circular economy: The expected transition to a balanced interplay of environmental and economic systems. Journal of Cleaner Production, 114, 11-32. doi:10.1016/j.jclepro.2015.09.007

Gomes Correia, A., Cortez, P., Tinoco, J. ve Marques, R. (2013). Artificial Intelligence Applications in Transportation Geotechnics. Geotechnical and Geological Engineering, 31(3), 861-879. doi:10.1007/s10706-012-9585-3

Gomes Correia, A., Winter, M. G. ve Puppala, A. J. (2016). A review of sustainable approaches in transport infrastructure geotechnics. Transportation Geotechnics, 7, 21-28. doi:10.1016/j.trgeo.2016.03.003

Guo, J., Xu, X., Song, X., Wei, J., Shi, W. ve Xia, Y. (2025). Comparison of the stabilized waste soil properties and stabilization

mechanism of phosphogypsum-fly ash-steel slag based cement versus Portland cement. PLOS One, 20(6), e0318862. doi:10.1371/journal.pone.0318862

Haryono, I. S., Saw, A. L., Lee, S. W. ve Wong, L. C. K. (2022). Digital Twin for Geotechnical Engineering Applications (ss. 73-84). The HKIE Geotechnical Division 41st Annual Seminar, sunulmuş bildiri. doi:10.21467/proceedings.126.7

Hasan, U., Whyte, A., Al Jassmi, H. ve Hasan, A. (2022). Lifecycle Cost Analysis of Recycled Asphalt Pavements: Determining Cost of Recycled Materials for an Urban Highway Section. CivilEng, 3(2), 316-331. doi:10.3390/civileng3020019

Horpibulsuk, S., Phetchuay, C. ve Chinkulkijniwat, A. (2012). Soil Stabilization by Calcium Carbide Residue and Fly Ash. Journal of Materials in Civil Engineering, 24(2), 184-193. doi:10.1061/(ASCE)MT.1943-5533.0000370

International Organization for Standardization. (2006a). ISO 14040:2006, Environmental management—Life cycle assessment—Principles and framework. Multiple. Distributed through American National Standards Institute.

International Organization for Standardization. (2006b). ISO 14044:2006, Environmental management—Life cycle assessment—Requirements and guidelines. Multiple. Distributed through American National Standards Institute.

International Organization for Standardization. (2017). ISO 15686:2017, Buildings and constructed assets—Service life planning—Part 5: Life-cycle costing. Geneva: ISO. Multiple. Distributed through American National Standards Institute.

Jassim, N. W., Hassan, H. A., Mohammed, H. A. ve Fattah, M. Y. (2022). Utilization of waste marble powder as sustainable

stabilization materials for subgrade layer. Results in Engineering, 14, 100436. doi:10.1016/j.rineng.2022.100436

Juveria, F., Rajeev, P., Jegatheesan, P. ve Sanjayan, J. (2023). Impact of stabilisation on mechanical properties of recycled concrete aggregate mixed with waste tyre rubber as a pavement material. Case Studies in Construction Materials, 18, e02001. doi:10.1016/j.cscm.2023.e02001

Kalatehjari, R., Najafi, E. K. ve Asadi, A. (2025). Pumice soil stabilisation using alkali-activated waste glass for sustainable road subgrade applications. Scientific Reports, 15(1), 21287. doi:10.1038/s41598-025-99016-6

Khawaja, L., Asif, U., Onyelowe, K., Al Asmari, A. F., Khan, D., Javed, M. F. ve Alabduljabbar, H. (2024). Development of machine learning models for forecasting the strength of resilient modulus of subgrade soil: Genetic and artificial neural network approaches. Scientific Reports, 14(1), 18244. doi:10.1038/s41598-024-69316-4

Kianimehr, M., Shourijeh, P. T., Binesh, S. M., Mohammadinia, A. ve Arulrajah, A. (2019). Utilization of recycled concrete aggregates for light-stabilization of clay soils. Construction and Building Materials, 227, 116792. doi:10.1016/j.conbuildmat.2019.116792

Kumar, A., Sinha, S., Saurav, S. ve Chauhan, V. B. (2024). Prediction of unconfined compressive strength of cement–fly ash stabilized soil using support vector machines. Asian Journal of Civil Engineering, 25(2), 1149-1161. doi:10.1007/s42107-023-00833-9

Li, S., Hai, M., Zhang, Q., Zhou, B., Wang, M. ve Zhao, Z. (2025). Study on an interpretable prediction model for pile bearing capacity based on SHAP and BP neural networks. Scientific Reports, 15(1), 28134. doi:10.1038/s41598-025-13616-w

Lu, C., Chen, J., Gu, C., Wang, J., Cai, Y., Zhang, T. ve Lin, G. (2021). Resilient and permanent deformation behaviors of construction and demolition wastes in unbound pavement base and subbase applications. Transportation Geotechnics, 28, 100541. doi:10.1016/j.trgeo.2021.100541

Luo, Z., Xue, X., Xiong, C., Huang, R., Du, J., Li, J. ve Liu, K. (2025). Data-driven prediction of unconfined compressive strength in stabilized soils using machine learning. Discover Applied Sciences, 7(10), 1122. doi:10.1007/s42452-025-07766-9

McKenna, G., Argyroudis, S. A., Winter, M. G. ve Mitoulis, S. A. (2021). Multiple hazard fragility analysis for granular highway embankments: Moisture ingress and scour. Transportation Geotechnics, 26, 100431. doi:10.1016/j.trgeo.2020.100431

Miguel, G. D., Saldanha, R. B., Da Silva, A., Festugato, L., Chaves, H. M. ve Mendes, C. C. (2022). Life Cycle Assessment Comparison of Distinct Soil Stabilizations Methods: An Environmental and Cost Approach to the Soil Improvement. Proceedings of the Institution of Civil Engineers—Ground Improvement, 1-41. doi:10.1680/jgrim.21.00006a

Oluleye, B. I., Chan, D. W. M., Saka, A. B. ve Olawumi, T. O. (2022). Circular economy research on building construction and demolition waste: A review of current trends and future research directions. Journal of Cleaner Production, 357, 131927. doi:10.1016/j.jclepro.2022.131927

Pettinaroli, A. (2024). Advances in the sustainability assessment of geotechnical ground improvement processes. https://boa.unimib.it/handle/10281/461828 adresinden erişildi.

Samuelsson, I, Larsson, S. ve Spross, J. (2021). Life cycle assessment and life cycle cost analysis for geotechnical engineering: Review and research gaps. IOP Conference Series: Earth and

Environmental Science, 710(1), 012031. doi:10.1088/1755-1315/710/1/012031

Samuelsson, Ida, Spross, J. ve Larsson, S. (2024). Integrating life-cycle environmental impact and costs into geotechnical design. Proceedings of the Institution of Civil Engineers—Engineering Sustainability, 177(1), 19-30. doi:10.1680/jensu.23.00012

Sánchez-Garrido, A. J., Navarro, I. J. ve Yepes, V. (2022). Evaluating the sustainability of soil improvement techniques in foundation substructures. Journal of Cleaner Production, 351, 131463. doi:10.1016/j.jclepro.2022.131463

Sharma, A. K. ve Sivapullaiah, P. V. (2016). Ground granulated blast furnace slag amended fly ash as an expansive soil stabilizer. Soils and Foundations, 56(2), 205-212. doi:10.1016/j.sandf.2016.02.004

Sharma, K. ve Kumar, A. (2020). Utilization of industrial waste—Based geopolymers as a soil stabilizer—A review. Innovative Infrastructure Solutions, 5(3), 97. doi:10.1007/s41062-020-00350-7

Shillaber, C. M., Mitchell, J. K. ve Dove, J. E. (2016). Energy and Carbon Assessment of Ground Improvement Works. II: Working Model and Example. Journal of Geotechnical and Geoenvironmental Engineering, 142(3), 04015084. doi:10.1061/(ASCE)GT.1943-5606.0001411

Shillaber, C. M., Mitchell, J. K., Dove, J. E. ve Ostrum, Z. A. (2017). Framework to Account for Uncertainty in Energy and Carbon Assessment of Ground Improvement Works. Journal of Geotechnical and Geoenvironmental Engineering, 143(5), 04016122. doi:10.1061/(ASCE)GT.1943-5606.0001649

Suer, P., Hallberg, N., Carlsson, C., Bendz, D. ve Holm, G. (2009). Biogrouting compared to jet grouting: Environmental (LCA)

and economical assessment. Journal of Environmental Science and Health, Part A, 44(4), 346-353. doi:10.1080/10934520802659679

Vitor, K. A. ve Danziger, B. R. (2021). Discussion of "Settlement Estimation of Piled Rafts for Initial Design" by Priyanka Bhartiya, Tanusree Chakraborty, and Dipanjan Basu. Journal of Geotechnical and Geoenvironmental Engineering, 147(5), 07021003. doi:10.1061/(ASCE)GT.1943-5606.0002496

Yao, Q., Tu, Y., Yang, J. ve Zhao, M. (2024). Hybrid XGB model for predicting unconfined compressive strength of solid waste-cement-stabilized cohesive soil. Construction and Building Materials, 449, 138242. doi:10.1016/j.conbuildmat.2024.138242

Youwai, S. ve Pamungmoon, A. (2025). Developing an explainable artificial intelligent (XAI) model for predicting pile driving vibrations in Bangkok's subsoil. Neural Computing and Applications, 37(18), 12881-12902. doi:10.1007/s00521-025-11203-8


BİDGE